NON-HERMITIAN TOPOLOGICAL PHASES IN ELASTIC AND ACOUSTIC LATTICES

HAIYAN FAN

PhD

The Hong Kong Polytechnic University

2023

The Hong Kong Polytechnic University

Department of Mechanical Engineering

Non-Hermitian Topological Phases in Elastic and Acoustic Lattices

Haiyan Fan

A thesis submitted in partial fulfilment of the requirements

for the degree of Doctor of Philosophy

August 2023

CERTIFICATE OF ORIGINALITY

I hereby declare that this thesis is my own work and that, to the best of my knowledge and belief, it reproduces no material previously published or written, nor material that has been accepted for the award of any other degree or diploma, except where due acknowledgment has been made in the text.

_____ (Signed)

___Haiyan FAN___(Name of student)

ABSTRACT

Classical wave systems have been fertile grounds where topological physics are investigated, enabling the discoveries of numerous intriguing phenomena such as backscattering-free chiral edge states associated with the quantum Hall–like effect and localized edge (corner) modes due to the quantized bulk dipole (quadrupole) moments. Much effort in this field has hitherto dedicated to the Hermitian Hamiltonians characterized by real-valued eigenfrequencies and orthogonal eigenvectors, while the intrinsically lossy nature of classical wave systems has inspired explorations towards their non-Hermitian counterparts for more realistic experimental investigations and practical applications. In this thesis, a series of non-Hermitian topological phenomena are explored in elastic and acoustic lattices, aiming at offering new opportunities to explore topological physics and their potential applications in acoustic and elastic wave manipulation.

This thesis starts with one-dimensional (1D) perturbative elastic metamaterials based on the Su–Schrieffer–Heeger (SSH) model to investigate the Hermitian topological edge states and their non-Hermitian counterparts. The designed metamaterials are tight-binding chains consisting of square plates (corresponding to mass points) connected by thin beams (corresponding to rigid bonds). For the hypothetically Hermitian case, alternating coupling strengths contribute to dimerization which gives rise to topologically non-trivial and trivial band gaps as well as the associated topological edge states. For the non-Hermitian case, uneven absorptive damping treatments applied to the double-sized unit cell modulate the system in a similar way

as the uneven damping treatments are capable of creating topological edge states even under identical coupling strength.

In the next chapter, it is shown that the topological edge states can be shifted to coexist with a bulk band, rather than emerging in a band gap as commonly seen, forming the so-called topological bound states in the continuum (BICs). These embedded topological states are observed in a 1D trimerized elastic lattice, which are produced solely by non-Hermiticity realized using constrained damping layers attached to particular sites in the finite-sized chain assembly. The results indicate that appropriately tailored non-Hermitian modulation can induce topological edge states that appear in the bulk spectrum, not necessarily requiring the construction of band gaps.

This thesis further extends the 1D topological phenomena to a two-dimensional (2D) space, which could control not only the first-order topological edge states but also the second-order topological corner states. Different from the conventional wisdom that a topological state is usually altered with varied topological phase, this chapter shows an exception in non-Hermitian acoustic crystals. In an acoustic quadrupole topological insulator (QTI), its topological corner, edge and bulk states can be arbitrarily engineered at any desired positions with its topological phase maintained. These non-Hermiticity-controlled topological states bestow a bulk structure with unique features and versatilities not available in Hermitian scenarios.

The above studies only concern topological phenomena in either fluids or solids alone, with fluid-solid interactions neglected. The following chapter attempts to

answer the question on how intricate fluid-solid interactions in “mixtures” can breed novel topological physics. With a simple three-dimensional (3D) phononic crystal immersed in water, this chapter shows that the unique interplay between fluids and solids can be utilized to realize type-II nodal rings, elusive in phononics. Strongly tilted drumhead surface states, the hallmark phenomena, are also experimentally demonstrated.

In summary, starting from 1D elastic lattices to 2D acoustic lattices, and finally to a 3D phononic crystal with fluid-solid interaction coming into play, multiple new breeds of topological phenomena are demonstrated both in theory and experiment. These results extend the topological physics beyond the conventional Hermiticity assumption and offer reconfigurable and versatile approaches to manipulating topological phenomena. Besides, these phononic approaches open a door to explore topological physics in classical systems, which is easy to implement and can be used for designing high-performance devices.

PUBLICATIONS ARISING FROM THE THESIS

Refereed Journal Papers

1. **Haiyan Fan**, He Gao, Shuowei An, Zhongming Gu, Shanjun Liang, Yi Zheng, and Tuo Liu*, “Hermitian and non-Hermitian topological edge states in one-dimensional perturbative elastic metamaterials” Mechanical Systems and Signal Processing 169,108774 (2022).

2. **Haiyan Fan**, He Gao*, Shuowei An, Zhongming Gu, Yafeng Chen, Sibo Huang, Shanjun Liang, Jie Zhu, Tuo Liu*, and Zhongqing Su*, “Observation of non-Hermiticity-induced topological edge states in the continuum in a trimerized elastic lattice” Physical Review B 106, L180302 (2022).

3. **Haiyan Fan**, He Gao*, Tuo Liu, Shuowei An, Xianghong Kong, Guoqiang Xu, Jie Zhu, Cheng-Wei Qiu*, Zhongqing Su*, "Reconfigurable topological modes in acoustic non-Hermitian crystals" Physical Review B 107, L201108 (2023). (**Editors’ Suggestion**)

4. Xiaoxiao Wu, **Haiyan Fan**, Tuo Liu, Zhongming Gu, Ruo-Yang Zhang, Jie Zhu*, and Xiang Zhang*, “Topological phononics arising from fluid-solid interactions” Nature Communications 13, 6120 (2022). (**Co-first author**)

5. Shuowei An, Tuo Liu, **Haiyan Fan**, He Gao, Zhongming Gu, Shanjun Liang, Sibo Huang, Yi Zheng, Yafeng Chen*, Li Cheng*, Jie Zhu*, “Second-order elastic topological insulator with valley-selective corner states” International Journal of Mechanical Sciences 224, 107337 (2022).

6. Yi Zheng, Shanjun Liang, **Haiyan Fan**, Shuowei An, Zhongming Gu, He Gao, Tuo Liu*, Jie Zhu, “Acoustic Luneburg lens based on a gradient metasurface for spoof surface acoustic waves” JASA Express Letters 2, 024004 (2022).

7. Lei Fan, Yafeng Chen, Shuowei An, Tuo Liu, **Haiyan Fan**, Jie Zhu*, and Zhongqing Su*, “Local-Resonance-Induced Dual-Band Topological Corner States of Flexural Waves in a Perforated Metaplate” Physical Review Applied 19, 034065 (2023).

ACKNOWLEDGEMENTS

First and foremost, I would like to thank my chief supervisor, Prof. Zhongqing Su for his support in my research work and common life. He provides me so many valuable suggestions and enough degrees of freedom to support my research. I still remember the experience that I attended an international academic conference with him in the USA, he gave me many detailed suggestions about my slides and presentation, demonstrated how to give a clear speech and shared with me his experience of giving a presentation. Thanks to him, in every presentation after that, I kept his advice in mind and tried to give a vivid and impressive speech. Meanwhile, my deep appreciation is dedicated to my supervisor, Prof. Jie Zhu, who gave me great support in daily life and generous help for career planning. I also want to express my gratitude to my supervisor, Prof. Tuo Liu. He is a young professor fighting in the front line of scientific research. I always set him as my benchmark. Due to his meticulous guidance and vast knowledge, my independent research ability and writing skills have been significantly improved. I wish to thank Prof. Cheng-Wei Qiu from the National University of Singapore who gave me a precious opportunity in the attachment program as a host supervisor. The experience broadens my views on metamaterials and benefits me a lot beyond academics. I was fortunate to have so many kind, patient and intelligent Ph.D. supervisors.

Next, I would like to convey my gratitude to the technicians of ME department, Mr. Billy Yan, and Dr. Stephen Ng who always help me when I encounter some experimental problems. At the same time, many thanks to Ms. Lily Tam, Mrs.

Michelle Lai, Mrs. Merlin Wong and Mrs. Yan Wong for their work on various general affairs.

In addition, I would like to thank my colleagues and friends in the PolyU. With help from Dr. He Gao, Dr. Zhongming Gu, Dr. Shanjun Liang, Dr. Shuowei An, Dr. Sibo Huang and Mr. Lei Fan, I become familiar with my research topics and experimental equipment soon. I am also grateful to every friend from everyday birthday team, we shared much time together during the lockdown period and gave each other great support and companionship.

Last but not least, my deepest appreciation is given to my family members and my beloved husband. Their selfless support and encouragement give me the power, strength and courage in pursuing my PhD degree.

NOMENCLATURE

Acronyms and Initialisms

QHE	Quantum Hall Effect
2D	Two-dimensional
QSHE	Quantum Spin Hall Effect
3D	Three-dimensional
TSMs	Topological Semimetals
TIs	Topological Insulators
TRS	Time Reversal Symmetry
PT	Parity-Time
1D	One-dimensional
TBMs	Tight-binding Models
SSH	Su–Schrieffer–Heeger
QVHE	Quantum Valley Hall Effect
DPs	Dirac points
TPTs	Topological Phase Transitions
QTI	Quadrupole Topological Insulator
EP	Exceptional Point
DSSs	Drumhead Surface States
HOTIs	Higher-order Topological Insulators
BZ	Brillouin Zone
T	Time-reversal

P	Parity
DOF	Degree of Freedom
LCP	Left-handed Circular Polarization
RCP	Right-handed Circular Polarization
0D	Zero-dimensional
BBH	Benalcazar, Bernevig and Hughes
S	Symmetric
A	Anti-symmetric
FRF	Frequency Response Function
AD	Additional Damping
ID	Intrinsic Damping
BICs	Bound States in the Continuum
HLS	High-loss Subarea
LLS	Low-loss Subarea
WG	Waterborne Guided
FL	Flexure Lamb
EL	Extensional Lamb
SH	Shear Horizontal

Symbols

χ	Geometric topological invariant
K	Gaussian curvature
g	Number of holes
C	Chern number
$\vec{\Omega}$	Berry curvature
$\vec{k}$	Wave vector
$\langle \xi(k) \rvert$	Periodic part of a wavefunction
H	Hamiltonian matrix
t	Intra-cell hopping
s	Inter-cell hopping
ε	Nearest-neighbour hopping
ϑ	Zak phase
a	Lattice constant
γ	Intra-unit coupling
λ	Inter-unit coupling
κ	Coupling strength
E_0	Young's modulus
ρ	Density
v	Poisson's ratio
u_z	Out-of-plane displacement
w	Width of the beam
h	Distance from the beam to the nodal line
l	Length of the beam

f_0	First non-rigid-body resonance frequency
c	Sound speed
δ_w	Resonance perturbation strength
δ_κ	Coupling perturbation strength
$X(\omega)$	Velocity/displacement/acceleration response signal in frequency domain
$F(\omega)$	Excitation force in frequency domain
ω	Angular frequency
$X(t)$	Velocity/displacement/acceleration response signal in time domain
$F(t)$	Excitation force in time domain
$H(\omega)$	Frequency response function
d_0	Intrinsic damping
d_1	Additional damping
p	Biorthogonal polarization
δf	Frequency deviation
γ_1	Intrinsic loss
γ_2	Additional loss
$\Delta\gamma$	Loss contrast
δ_γ	Loss perturbation strength
p_x	Quantized edge polarization along x
p_y	Quantized edge polarization along y
$\Delta\omega$	Frequency variation

ω_{mid}	The middle of frequencies
D	Bending stiffness
M_z	Mirror symmetry along z
$\left\|n_1\right\rangle$	Eigenmode one
$\left\|n_2\right\rangle$	Eigenmode two
V_{w}	Fluid domain of the unit cell
V_{m}	Solid domains of the unit cell
e	Elastic strain tensor
C	Stiffness tensor connecting stress and strain of the solid

TABLE OF CONTENTS

LIST OF FIGURES

CHAPTER 1

Introduction

1.1 Background and Motivation

Topology is initially a branch of geometric mathematics to study the unchanged characteristics of continuously deformed objects. For instance, in Fig. 1.1, a salient difference between a sphere and a torus can be intuitively recognized, that is, the number of holes. The hole number is identified by an equation:

$$\chi = \frac{1}{2\pi}\oint KdS = 2 - 2g \tag{1.1}$$

where χ is an integer number, named as geometric topological invariant, K is the Gaussian curvature defined on the surface, and g is the number of holes. χ is fixed regardless of the any continuous deformation of the object, expect creating or eliminating holes inside the structure.

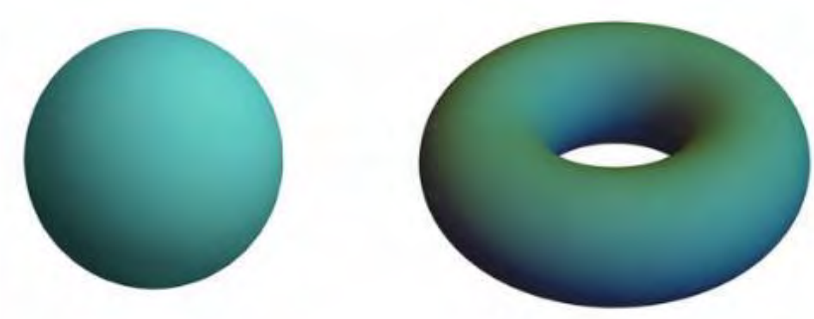

Figure 1.1 Basic examples of different topological objects. Different shapes are indicated by different topological invariants.

In the 1980s, the remarkable discovery of the integer quantum Hall effect (QHE) in a two-dimensional (2D, unit cells periodically arranged along two spatial directions) electron gas under ultra-low temperature and a super strong magnetic field [1] brought the concept of topology into physics, triggering the tremendous exploration towards topological phenomena in condensed matter physics [2-4]. The topological phases of matter are characterized with insulating interior and robust conducting edges. The bulk-edge correspondence relates the existence of back-scattering immune edge states to the bulk topological invariants [5], which takes the form of

$$C=\frac{1}{2\pi}\oint\vec{\Omega}(\vec{k})dS=\frac{1}{2\pi}\oint i\nabla_k\times\langle\xi(k)|\nabla_k|\xi(k)\rangle dS \tag{1.2}$$

where C is an integer number named physical topological invariant (Chern number), and $\vec{\Omega}(\vec{k})$ is the Berry curvature defined on the surface and can be written as $\vec{\Omega}(\vec{k})=i\nabla_k\times\langle\xi(k)|\nabla_k|\xi(k)\rangle$ with $\langle\xi(k)|$ being the periodic part of the wavefunction on a Bloch band. After the discovery of QHE, other related topological phases have also been investigated, including the quantum spin Hall effect (QSHE) [6, 7], three-dimensional (3D, unit cells periodically arranged along all three spatial directions) topological phases in topological semimetals (TSMs) [8-10] and topological insulators (TIs) [11, 12]. These phases of matter with robust edge states against local perturbations could offer greater possibilities for exploring sophisticated applications in electronic devices.

Inspired by the progress of topological phases in condensed matter systems, their counterpart in classical wave systems, including acoustics and elastics (dubbed phononic crystals), have rapidly become artificial platforms to investigate novel

physical mechanisms and extraordinary phenomena associated with topological phases. Furthermore, acoustic and elastic wave systems can even facilitate the investigation of exotic phenomena previously unreachable or extremely difficult in condensed matter systems. They have several advantages in probing topological physics. First and foremost, they are robust to temperature and do not have inter-particle interaction, which helps them to become exceptional macroscopic platforms to probe quantum physics that require complicated atomic-scale operations. Secondly, the design and fabrication of “atoms” and hopping strengths among “atoms” are more flexible and simper in acoustic and elastic topological structures, which facilitate the theoretical and experimental studies of topological phenomena in different dimensions as the “atoms” can be deliberately stacked. Thirdly, the observable frequency in phononic crystals is almost arbitrary, without the limitation in condensed matter systems, where investigation must take place close to the Fermi level. However, some barriers still exist during the implementation of topological phases in phononic crystals due to the lack of a half-integer spin of phonons and their inertia to external magnetic field. For instance, in the realization of QHE, the external magnetic field is exerted to break the time-reversal symmetry (TRS) of the electronic system. Instead, in the implementation of acoustic analogy of QHE, the creation of effective magnetic field that breaks TRS is realized by exerting a circulating airflow [13]. The investigation of topological phases in phononic crystals can enhance the flexibility to manipulate acoustic and elastic waves and lay the foundation for a series of promising applications, such as sound energy harvesting, high-quality sensors, and on-chip phononic circuits.

Most relevant studies in topological physics are based on the premise of Hermiticity, for its simplicity, with which the real eigenvalues and orthogonal eigenstates of their effective Hamiltonians ensure the well-defined topological invariants and bulk-edge correspondence [5, 14]. Acoustic and elastic wave systems, however, are naturally non-Hermitian with loss and/or gain arising from the energy exchange with the surrounding environment. In this regard, taking into consideration the effect of non-Hermiticity when investigating acoustic and elastic topological phases represents a more realistic scenario and is thus essential for practical applications. Particularly, the intrinsic losses such as thermo-viscous and viscoelastic effects, major sources of non-Hermiticity in realistic scenario, are usually considered as negative factors as they naturally lead to energy dissipation and inevitably increase the difficulty in experimental implementation. Contrary to the negative impression of non-Hermiticity, recent studies have indicated that it can bring about novel physical phenomena, such as non-Hermitian parity-time (PT) symmetry [15, 16], topological phase transition [17-20] and breakdown of fundamental bulk–edge correspondence [21-23].

Moreover, the quest for topological phononic systems often concerns sound in either fluids or solids alone (usually termed acoustic wave or elastic wave, respectively). As mechanical waves [24], sound propagates as a perturbation of pressure in fluids and elastic stress in solids, thereby being represented by a scalar field and vector field, respectively. This fundamental point leads to intrinsic differences in the dynamics and symmetries for sound in fluids and solids, a characteristic absent in photonics [25]. However, such intrinsic differences and their possible interactions have yet to

be considered in the development of topological phononics, even for underwater environment where the interactions can become considerable [26, 27].

1.2 Research Objectives

Due to the fact that taking into consideration the effect of losses and fluid-solid interactions represents much more realistic scenarios in topological phononics, and motivated by the lack of investigations of topological phononics arising from non-Hermiticity and fluid-solid interactions as commented above, this PhD study is dedicated at exploring new breeds of topological phases in phononic crystals based on non-Hermitian modulations and fluid-solid interactions, from one-dimensional (1D, unit cells periodically arranged along only one spatial direction) elastic lattices, 2D acoustic lattices, to 3D perforated elastic plates immersed in water. The designed elastic and acoustic lattices are the experimental implementations of the corresponding tight-binding models (TBMs) which significantly enrich the topological physics and application prospects. To address the incompleteness and insufficiency of existing research woks on topological phononics, the following detailed objectives are set:

(i) To calculate the well-defined topological invariant in the non-Hermitian setting;

(ii) To design acoustic and elastic models with good manufacturability and functionality to investigate the non-Hermiticity-induced topological phases;

(iii) To fabricate the experimental samples by 3D printing or laser cutting techniques with high precision;

(iv) To set up the airborne acoustic, waterborne acoustic and elastic wave test

platforms, scrutinize the excitation and detection performances, and to conduct the relevant experiments;

(v) To evaluate the measured results of time domain signals, resonance frequencies, field maps in the real space for each frequency, and band diagrams in the reciprocal space;

1.3 Organization of the Thesis

This PhD study is devoted to investigating new topological phononic systems with topologically protected eigenstates arising from non-Hermiticity and fluid-solid interactions. These topological states are expected to feature merits of extraordinary reconfigurability, good flexibility, and excellent robustness to deliberately introduced defects. This thesis is organized in the order of increasing dimensionality, from 1D in-gap and in-band topological edge states in elastic lattice, through 2D reconfigurable higher-order topological states in acoustic lattice, to fluid-solid interactions induced topological phenomena in a 3D phononic crystal.

A brief literature review that concerns acoustic and elastic TIs in three different dimensions, higher-order topological phenomena and non-Hermitian topological physics is presented in Chapter 2. Major achievements in this field are reviewed, including acoustic and elastic counterparts of 1D Su–Schrieffer–Heeger (SSH) model, 2D TIs with QHE, QSHE, and Quantum Valley Hall Effect (QVHE), 3D TIs based on Dirac points (DPs, linear degenerate points in the band diagram), 3D TSMs with Weyl points and nodal lines (linear degenerate lines in the band diagram) and higher-order TIs based on quantized bulk multipole moments, the nontrivial dipole moments,

and the multidimensional topological phase transitions (TPTs). The concrete examples regarding to the above topological phenomena are also briefly introduced.

Chapter 3 is pertaining to the experimental demonstration of a type of elastic metamaterials, which is composed of aluminium resonant plates and thin linking beams, that can be described by the SSH model to realize topological edge states in elastic wave system under both Hermitian and non-Hermitian modulations. For the Hermitian case, alternating coupling strengths implemented by adjusting the linking positions of the thin beams are the reasons to induce TPTs. For the non-Hermitian case, additional added damping layers on the particular resonant plates of the metamaterial causes the emergence of topologically protected edge states. These results display the first experimental implementation of extending the topological physics in elastic wave systems beyond the conventional Hermiticity assumption.

In Chapter 4, to lift the requirement of complete band gaps in studying topological physics, we experimentally demonstrate a non-Hermitian scheme to induce the in-band topological edge states. The proposed trimerized elastic lattice is also a chain of plates connected through beams with equal coupling strength. We demonstrate that appropriately tailored non-Hermitian modulation can induce topological edge states that appear in the bulk spectrum rather than exist in the band gap. Besides, the existence of such topological edge states is observed to be closely linked to the configurations of the lattice boundaries.

As the non-Hermitian modulations are successfully utilized in creating topological edge states in 1D structures, the 2D structures with higher-order topological states

under non-Hermitian modulations are investigated in Chapter 5. A non-Hermitian recipe to realize reconfigurable topological interface waveguides and corner localizations based on an example of acoustic quadrupole topological insulator (QTI) is proposed. In experiments, the additional on-site losses are implemented by inserting the sound-absorbing sponges to specific cavities of the lattice, while keeping the other cavities intact. If the loss contrast between the two cavities exceeds a particular value [the exceptional point (EP) in eigenfrequency spectra], some newly topological states will emerge at the interfaces formed by different losses, leading to robust guiding and localization of acoustic waves with unchanged topological phase.

In Chapter 6, we go a step further to consider fluid-solid interaction and experimentally observe type-II nodal rings and strongly tilted drumhead surface states (DSSs) in a simple 3D phononic structure immersed in water. The phononic structure is composed of layer-stacked metallic plates with perforated through holes arranged in square lattice. The nodal rings also touch with each other, forming the firstly observed nodal chains in sound waves. Our study demonstrates that the previously often neglected fluid-solid interaction can give rise to interesting topological phenomena unobtainable for solely fluid-borne or solid-borne sound.

Chapter 7 is the concluding remarks of the thesis, and the recommendations for future research are also listed.

CHAPTER 2

State of the Art of Acoustic and Elastic Topological States: A Literature Review

2.1 Introduction

It has been a long time for scholars to find new and efficient methods to manipulate sound and vibration, as they convey vital information to perceive the nature. The idea of metamaterials, artificially designed materials or structures with on-demand exotic properties not available in nature, has suggested a promising direction towards unprecedent capabilities to engineer the basic and intrinsic characteristics of sound and vibration including but not limited to amplitude, phase, frequency and mode shape [24, 28]. More recently, topological phenomena have provided alternative and unparalleled approaches for classical wave manipulation, giving rise to novel acoustic and elastic topological structures. The hallmark of 2D phononic TIs is the ability to form robust and defect-immune waveguides at the artificially designed interfaces or edges. The existence of interface or edge states is governed by the bulk–edge correspondence associating these edge states with bulk topological

invariants [11, 12]. But the realistic applications of phononic TIs encounters some problems, such as the non-conservative characteristic of acoustic and elastic systems and fluid-solid interactions in the underwater environments. Interestingly, these problems in turn could lead to novel topological phenomena not found in conventional Hermitian framework.

In this literature review, we retrospectively introduce the fundamental concepts of topological physics applicable to acoustic and elastic waves, starting from the acoustic and elastic topological families of 1D examples based on the SSH model, 2D examples based on the time-reversal-broken topological phase of QHE and time-reversal-invariant topological phases, including the QSHE and QVHE, 3D cases of TIs and TSMs, and higher-order topological insulators (HOTIs) due to quantized dipole or multipole moments or multidimensional TPTs. We then move on to the latest developments in the field of non-Hermitian topological physics, including non-Hermiticity-induced TPTs and EPs.

2.2 Acoustic Topological Insulators

Acoustics is a branch of science that investigates sound and vibration phenomena ubiquitous in daily life, like speech and audio communication, musical instruments, noise, ultrasonic imaging, etc. Controlling sound flow at will has long been and will always be a central topic. Acoustic topological materials have been proposed as new

ways to manipulate sound wave propagation for decades. Many remarkable functionalities can be obtained by judiciously designing these artificial structures. In the following, we will review the most representative works of acoustic TIs in 1D, 2D and 3D structures.

2.2.1 One-dimensional Acoustic Topological Insulators

The SSH model for polyacetylene [29, 30] is one of the simplest and most typical paradigms with non-trivial topological states. The model is composed of a periodically arranged 1D chain of atoms with alternating hopping terms, intra-cell hopping t and inter-cell hopping s between the nearest neighbours [Fig. 2.1(a)]. The tight binding Hamiltonian matrix takes the form of

$$H=\begin{pmatrix} 0 & \varepsilon \\ \varepsilon^{*} & 0 \end{pmatrix} \tag{2.1}$$

where $\varepsilon=t+se^{-ik}$ and k is the Bloch wavenumber. Changing the value of $|t/s|$ can open or close the complete band gap. For $|t/s|\neq 1$, a complete band gap appears in the band diagram; otherwise, the gap closes and two bands degenerate at the Brillouin zone (BZ) edge [Fig. 2.1(b)]. The right-most panel in Fig. 2.1(b) manifests that the eigenfrequencies of the two bands at the BZ edge are dependent on the value of $|t/s|$.

The acoustic implementation of the tight binding Hamiltonian matrices has been experimentally proposed with coupled resonant cavities [31-35]. Each atomic site is replaced by an acoustic resonant cavity, and the hoppings between the atoms are mimicked by the thin tubes that connect the adjacent resonators. Here, different

hopping strengths are easily obtained by changing the cross-sectional areas of the coupling tubes, and the acoustic SSH chain is depicted in Fig. 2.1(c).

The Bloch wavefunctions of this acoustic SSH model is easy to examine, revealing that when $|t/s| \neq 1$, these two bands possess different symmetries (if one is symmetric then the other one must be antisymmetric) at the BZ edge. Besides, the symmetries are reversed after crossing the degenerate point $|t/s| = 1$. This evolution of the wavefunction symmetries can be evaluated by the Zak phase ϑ, which is a specific kind of the aforementioned topological invariants defined for isolated bulk bands [36]. Here, the Zak phase ϑ is calculated by integrating the Berry curvature over the first BZ, as defined in Eq. (1.2), and it turns out that for $|t/s| < 1$, the Zak phase takes the quantized value of π, for $|t/s| > 1$, $\vartheta = 0$. The Bloch wavefunctions of acoustic unit cells are indicated in Fig. 2.1(d), showing that the value of Zak phase can also be determined by comparing the wavefunctions at the edge ($k = \pi/a$) and center ($k = 0$) of the first BZ. If the wavefunctions switch symmetry at the center and edge of the first BZ, the Zak phase of this band is π; if the symmetry remains the same in this process, the Zak phase is 0 [37]. The topological concept of bulk–edge correspondence [5] can further predict the existence of topological edge states using bulk band characteristics (topological invariants) if the chain is truncated and become a finite-sized structure.

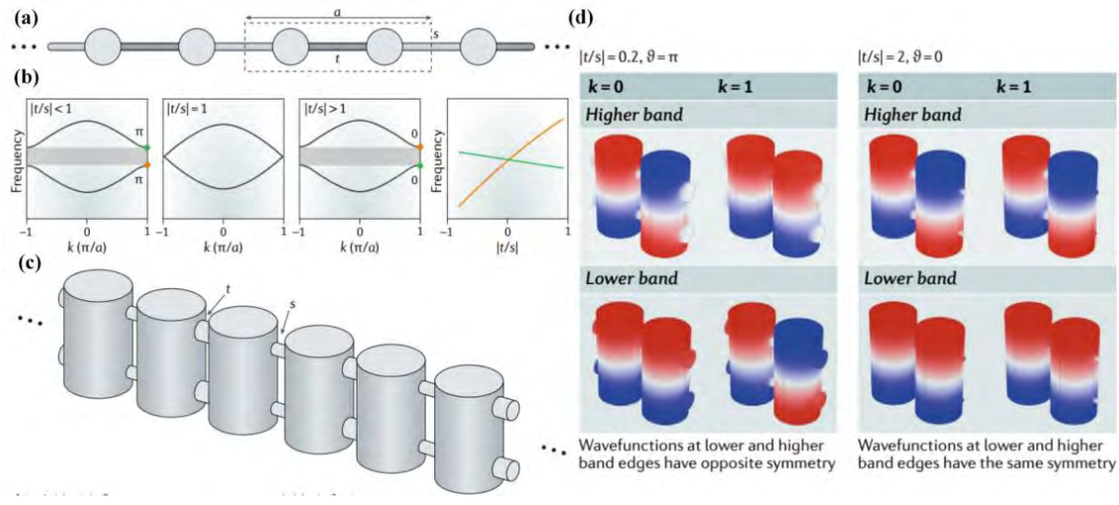

Figure 2.1 Acoustic analogue of the SSH model [38]. (a) Schematic of a dimerized SSH chain with lattice constant *a* and hopping terms *t* and *s*. (b) Band diagrams of infinite SSH chain with different values of $|t/s|$. (c) Implementation of the SSH model with acoustic linked cavities. (d) Simulated Bloch wavefunctions for the two bands correspond to the BZ centre ($k = 0$) and BZ edge ($k = 1$, in units of π/a).

2.2.2 Two-dimensional Acoustic Topological insulators

Having discussed the 1D TIs with an acoustic SSH example, we now briefly introduce the acoustic realizations of the symmetry-protected topological states in 2D TIs, including QHE, QSHE, and QVHE.

The QHE is the first proposed approach to observe the backscattering-immune topological edge propagation in a 2D electron gas in which a strong out-of-plane magnetic field is necessary [1]. Thouless et al. [2] further associated the QHE phenomenon with a topological invariant called the Chern number as defined by Eq. (1.2), which is related to the bulk bands. This effect can be straightforwardly understood by considering the cyclotron motion of the electrons (Fig. 2.2). The electrons can only travel in one direction (clockwise or anti-clockwise) due to the

broken time-reversal (***T***) symmetry induced by the out-of-plane magnetic field in the system. If the 2D system is not infinitely large, the cyclotron orbits must be broken at four edges, and the electrons at the edges have to jump to the neighboring orbit. As a result, a unidirectional current flow is formed as illustrated in Fig. 2.2.

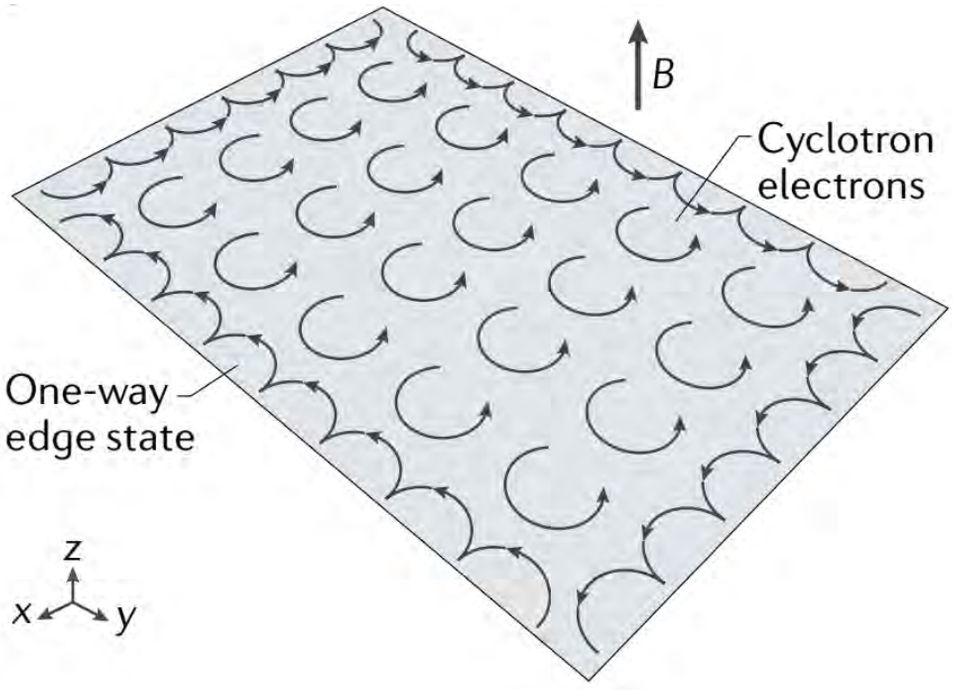

Figure 2.2 The cyclotron motion of the electrons in magnetic field, leading to the QHE [38].

For acoustic analogues of QHE, their implementation is not as intuitive as photonic QHE with the assistance of magneto-optical materials to break the ***T*** symmetry [39, 40]. Sound waves are magnetically inert, and the realization of QHE in acoustics demands new approaches. In fact, effective magnetic fields can be achieved in acoustic wave systems by setting the media in constant motion [13, 41]. In 2015, several theoretical ideas shed light on acoustic QHE by applying circular airflows in triangular [42] or honeycomb lattice [43, 44] to break ***T*** symmetry for sound. Here, we take the triangular lattice composed of rotating rods as an example to illustrate the detailed design in Fig. 2.3. Fluids in the dark blue regions in Fig. 2.3(a) are set in

a circulatory motion because of the rotated rods, while the remaining fluid in the light blue area is in a stationary state. The circulating flows lift the degeneracy at the DP, and form a non-trivial band gap [Fig. 2.3(b)] populated by chiral edge states [Fig. 2.3(c)]. These chiral edge states have the same property as aforementioned QHE, that is, it can propagate only in one direction along the boundary [Fig. 2.3(d)]. Besides, they also have robustness against moderate disorder and defects as illustrated in Fig. 2.3(d).

However, when it comes to the experimental validation of the proposed theory, several challenges including high airflow speed, out of synchronization rotation and flow instabilities must be overcome. In 2019, Ding et al. [45] propose an acoustic lattice consisting of optimized ring resonators with high quality factor [Fig. 2.3(e)], which substantially reduces the required airflow speed. As a result, the expected unidirectional edge transport is successfully observed.

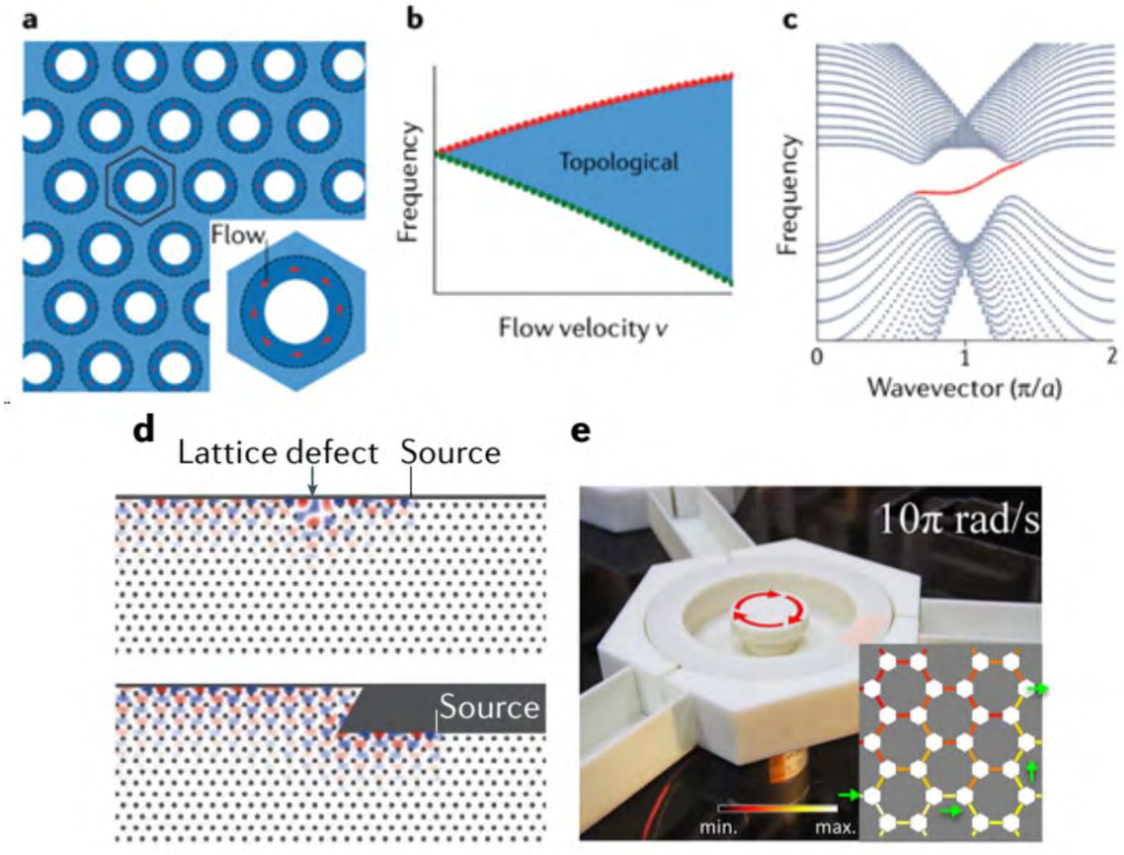

Figure 2.3 Acoustic analogues of the QHE. (a) Schematic of an acoustic QHE. The white circles are solid rods. (b) Frequency evolution with increased flow velocity. The DP is lifted when the velocity is nonzero. (c) Band diagram for a ribbon supercell. The edge band is marked by the red line [46]. (d) Simulated field profiles of the edge state in an acoustic lattice with cavity defect (top) and a bending (bottom) [42]. (e) Experimental sample of an acoustic QHE [45].

Different from the QHE, a system with QSHE preserves the $\boldsymbol{T}$ symmetry and is indeed protected by the $\boldsymbol{T}$ symmetry. Unlike fermionic electrons with intrinsic spin-±1/2, bosonic phonons carry intrinsic spin-0, leading to the $\boldsymbol{T}$ symmetry in acoustic systems satisfies $\boldsymbol{T}^2 = 1$. However, the electric systems with $\boldsymbol{T}$ symmetry satisfy $\boldsymbol{T}^2 = -1$, which enables the two-fold degenerate of electronic states at the $\boldsymbol{T}$-invariant momenta, with Kramers doublets consisting of spin-up and spin-down states [6, 7, 47]. Therefore, realizing the counterpart of the QSHE in acoustic waves depends on

constructing wavefunctions to obtain fermion-like pseudospins and artificial Kramers-like degeneracy.

One typical way is to realize the accidental double DP (a fourfold degeneracy in the band diagram) in graphene-like lattices composed of metallic scatters in a background medium of air or water [48, 49] [Fig. 2.4(a)]. By adjusting the filling ratio of the unit cell, such fourfold degeneracy will split into two gapped twofold degenerated states at the BZ center (two dipole states and two quadrupole states), which is also associated with band inversion and topological phase transition, as indicated in Fig. 2.4(b). In Fig. 2.4(b), the dipole and quadrupole states are denoted by the green and red lines, respectively, and the yellow and blue are topologically trivial and non-trivial phases, respectively. The dipole and quadrupole eigenstates at the BZ center are plotted in the inset. A pair of counterpropagating helical edge states [Fig. 2.4 (c)] can emerge at the interface between the trivial and topological non-trivial acoustic lattice, satisfying the requirement of Kramers-like degeneracy, and the corresponding acoustic QSHE waveguide with robustness against disorder, bends, and cavity can also be achieved [Fig. 2.4 (d)].

Another more general method to construct the analogues of QSHE in photonic, acoustic and mechanical systems resorts to the band folding mechanism [50-53]. The starting point is the primitive unit cell in an acoustic honeycomb lattice featuring a pair of DPs at the BZ corners (K and K’ points). By properly choosing a three times larger unit cell than the primitive one, the DPs are folded to the BZ center, forming a double DP with two dipole states and two quadrupole states. The hybridization of these states generates the required Kramers-like doublets. Then, by compressing or

stretching the scatters in the supercell while maintaining the C_{6v} symmetry, the double DP can be lifted, and topological phase transition can occur as well.

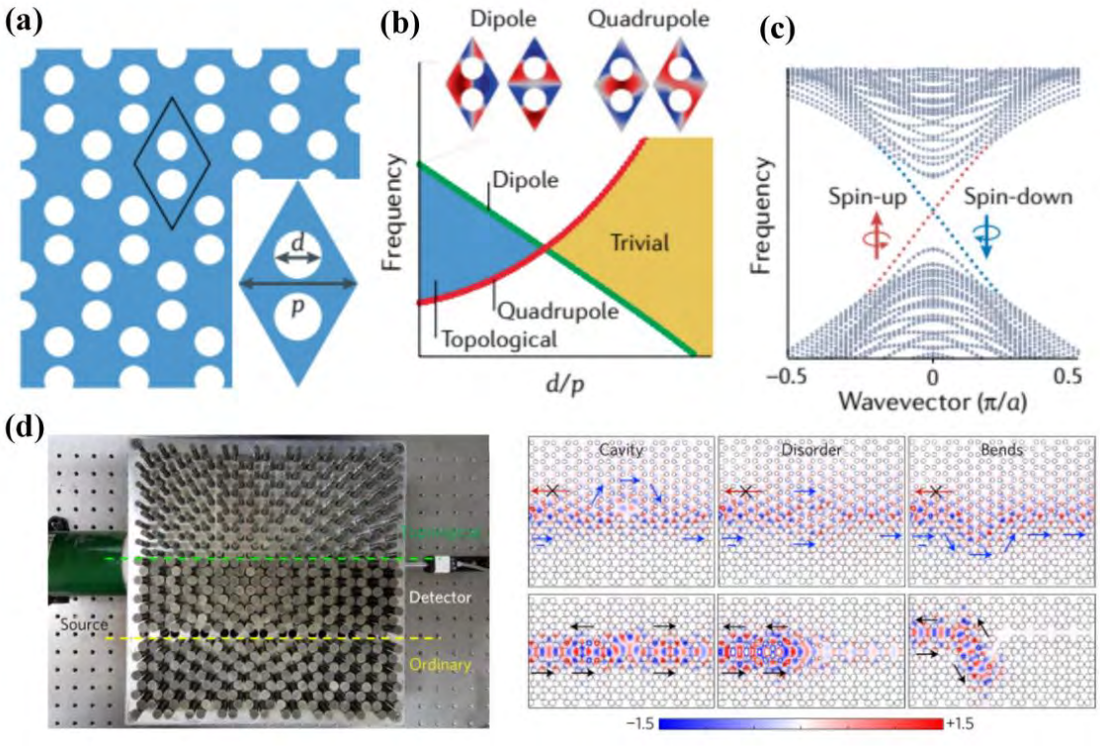

Figure 2.4 Acoustic analogues of the QSHE. (a) Schematic of an acoustic QSHE. The white circles are metallic rods, and the light blue region is fluid. (b) Topological phase transition. (c) Band diagram for a ribbon supercell. The red and blue dots represent the acoustic pseudospin-up and pseudospin-down edge states [46]. (d) An experimental set-up of an acoustic QSHE (left) and the simulated sound field profiles (right) in three different configurations, corresponding to three types of defects [49].

In addition to utilizing the spin degree of freedom (DOF) to implement the QSHE, the valley DOF has also been exploited in acoustics to implement another ***T***-invariant topological phase, called acoustic QVHE [54-56]. Acoustic QVHE is usually achieved by lifting DPs at the BZ corners by breaking the spatial-inversion (parity, ***P***) symmetry of the lattice, such that two local extrema emerge at the corners of the BZ in the band diagram, which are called valleys.

A conventional acoustic QVHE as indicated in Fig. 2.5(a) features equilateral triangular rods arranged in a triangular lattice inside a background medium of air. When the rods are orientated such that the acoustic lattice has C_{3v} symmetry, a pair of DPs appear at the BZ corners. Slightly changing the angle ϑ [Fig. 2.5(a)] can lower the $\boldsymbol{P}$ symmetry to C_3 and split the degeneracy of the DPs [55-57]. The energy flow at different valleys displays opposite vortices with either left-handed circular polarization (LCP) or right-handed circular polarization (RCP) [the insets in Fig. 2.5(b)], further associated with the band inversion and topological phase transition. Moreover, at the domain wall, which is the interface between two acoustic lattices with opposite ϑ, edge states appear [Fig. 2.5(c)]. These edge states are also related to a nonzero topological invariant localized to the valley named the valley Chern number, which is the integration of Berry curvature over a small BZ that includes only one valley. The experimental observation shows that these valley edge states can go through sharp bends with negligible scattering [Fig. 2.5(d)].

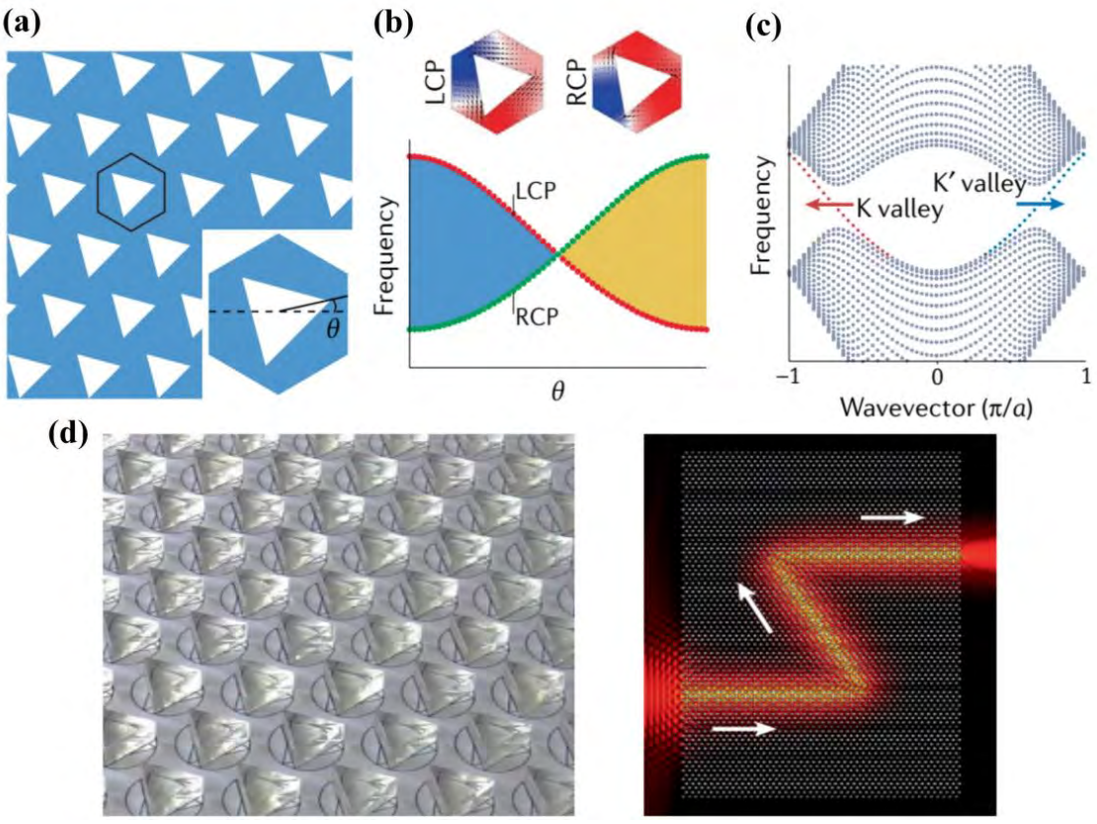

Figure 2.5 Acoustic QVHE. (a) Schematic of an acoustic QVHE. The white triangles are solid rods, and the light blue region is air. (b) Topological phase transition. (c) Band diagram for a ribbon supercell. The red and blue dots represent the valley edge states [46]. (d) An experimental sample of an acoustic QVHE (left) and the simulated sound field profiles (right) in a zigzag path [56].

2.2.3 Three-dimensional Acoustic Topological Insulators and Topological Semimetals

The extension of 2D acoustic topological phenomena to 3D generally can be divided into two groups, 3D acoustic TIs [58] and acoustic TSMs. 3D acoustic TIs are closely associated with 3D DP, which is a fourfold degenerate point with linear dispersions along all three directions (k_x, k_y and k_z) in the band diagram, as shown in the left panel of Fig. 2.6. There are primarily two approaches to achieve 3D DPs, one based on the band inversion mechanism [58, 59] and the other relying on crystalline

symmetries [60, 61]. By breaking the mirror symmetry along the *z* direction (see insets in Fig. 2.6), the space group of acoustic crystal shifts from No. 173 ($P6_3$) to No. 168 (P6), giving rise to a complete topological band gap, which supports robust surface sound propagation.

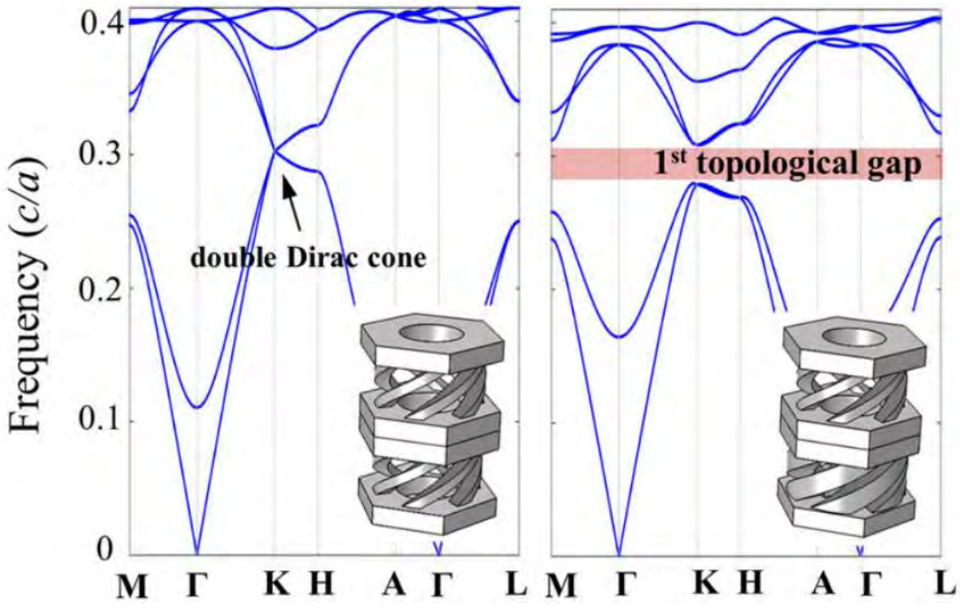

Figure 2.6 Band diagrams for 3D DP (left) and topological band gap (right) by *z*-axis folding and breaking, respectively. Insets indicate the corresponding acoustic unit cells [58].

Different from the TIs with topological band gaps, TSMs are nontrivial gapless phases having band degeneracies [8], including zero-dimensional (0D) nodal point, 1D nodal lines, and 2D nodal surfaces degeneracies. The nodal points mainly contain two kinds of 0D degeneracies, the Weyl points with twofold linear dispersion [Fig. 2.7(a)] and the 3D DPs [Fig. 2.7(b)]. A Weyl point can be regarded as a monopole of the Berry flux, which is demonstrated by integrating the Berry curvature on a surface encircling a Weyl point. The monopole behavior indicates that a Weyl point carry a topological charge defined by Chern number [62]. A Weyl semimetal is characterized by open isofrequency curves of surface states, called Fermi arcs [62], which link the

projections of a pair of oppositely charged Weyl points in momentum space [Fig. 2.7(a)]. Moreover, these two oppositely charged Weyl points can be combined and form a 3D DP with fourfold linear degeneracy [10]. The nodal lines [Fig. 2.7(c)] are generated by the band crossing along 1D lines [9]. According to the geometries of the nodal lines, they can be divided into nodal rings, nodal links, nodal knots and nodal chains [Fig. 2.7(d)]. There are three types of nodal rings, type-I [Fig. 2.7(e)], type-II [Fig. 2.7(f)] and hybrid [Fig. 2.7(g)], depending on the slopes of the crossing bands [63]. A nodal surface is a 2D band crossing.

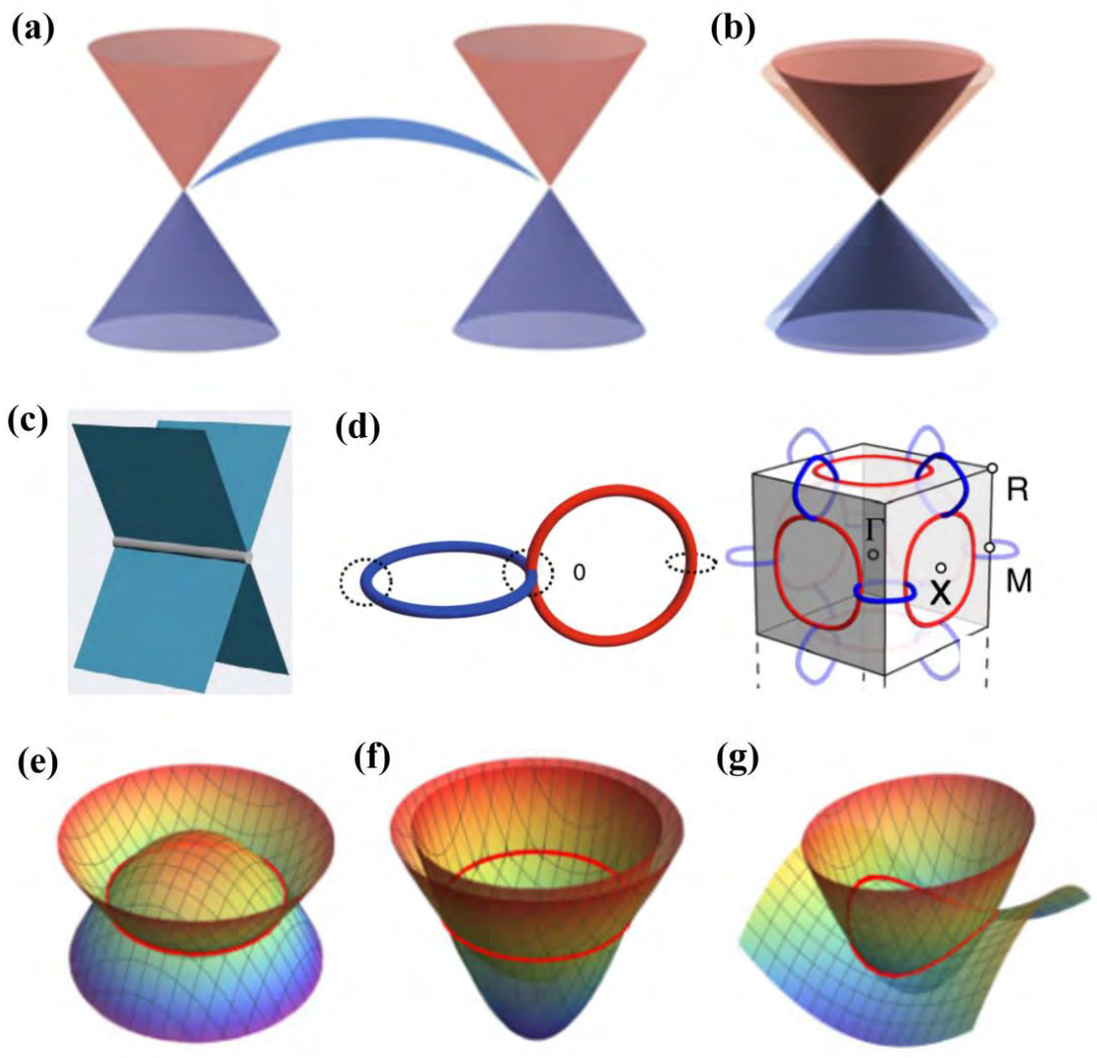

Figure 2.7 Schematic of band degeneracies in TSM. (a) The Weyl points and the surface Fermi arc. (b) A 3D DP [64]. (c) A straight nodal line [46]. (d) The nodal chains [65]. Type-I (e), Type-II (f) and hybrid (g) nodal rings [63].

Similar to the Weyl semimetals in electronic systems, acoustics Weyl semimetals also host Weyl points, which were experimentally observed in 3D artificial acoustic lattices [66-68]. For a system hosts both ***P*** and ***T*** symmetries, the Berry curvature is zero everywhere in momentum space [69]. Therefore, the minimum requirement to obtain Weyl points is to break either ***T*** or ***P*** symmetry. As the ***T***-broken acoustic systems involving circulating fluid flows, which is much more challenging to implement than breaking ***P*** symmetry, most acoustic Weyl points obtained so far only break ***P*** symmetry. Fig. 2.8(a) indicates a unit cell of an acoustic Weyl lattice that is created by stacking 2D honeycomb lattice layers along the *z* direction and each layer is connected by slanted tubes to accomplish chiral interlayer coupling. In the band diagram, two pairs of Weyl points with topological charge ± 1 [red and blue dots in Fig. 2.8(b)] appear at the BZ corners. As a result, a net Berry flux can exist in a 2D plane with a fixed k_z due to the charged Weyl points, leading to a nonzero topological invariant for the 2D band, which predicts the existence of topologically protected unidirectional surface transport in a finite-sized structure. The acoustic Fermi arcs [68] [Fig. 2.8(c)] are also associated with intriguing phenomena, like negative refraction [70] [Fig. 2.8(d)] and sound collimation [66]. The straight [71], ring-like [72] nodal lines [Fig. 2.8(e)] and nodal chains [73] formed by two intersected nodal rings were also experimentally investigated in layer-staked acoustic lattices. As the Zak phase along a closed path that encircles a nodal line is π, exotic drumhead surface states can emerge [72].

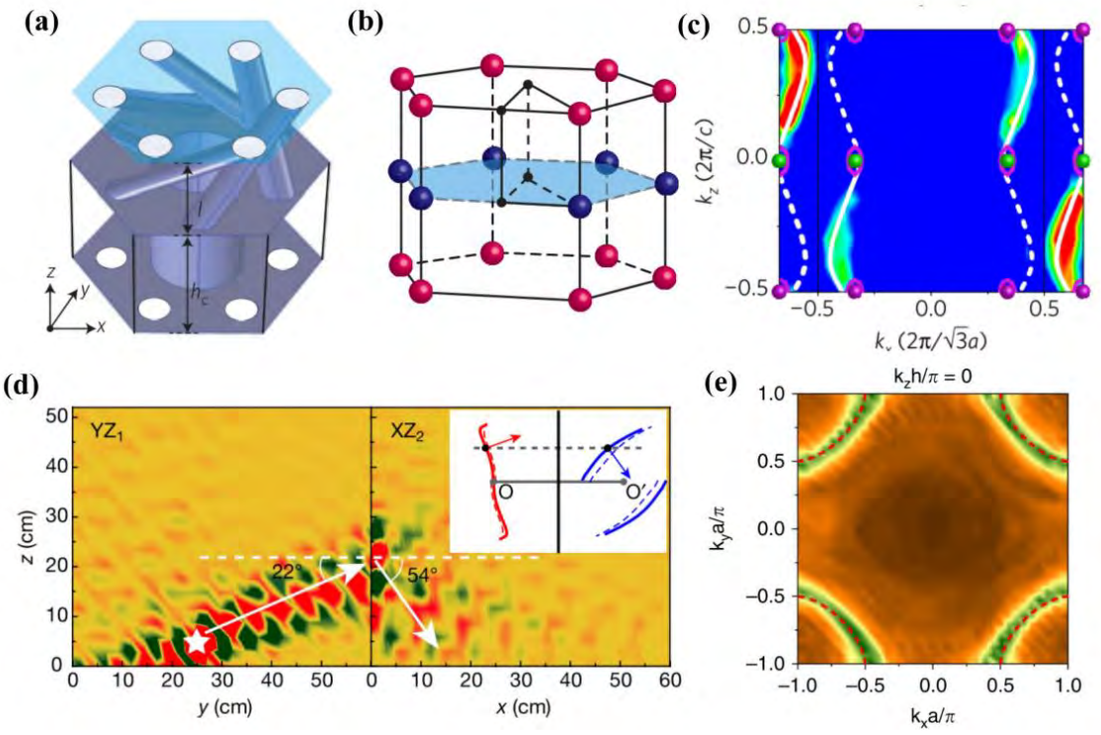

Figure 2.8 Acoustic Weyl points and nodal rings. (a) Unit cell of an acoustic Weyl lattice. (b) Weyl points in momentum space [67]. (c) The measured acoustic Fermi arcs [68]. (d) Measured field profile of topological negative refraction [70]. (e) Measure acoustic nodal rings [72].

2.2.4 Higher-order Acoustic Topological Insulators

Other than the acoustic counterparts of conventional 2D TIs and 3D TSMs, a new type of topological phase, called HOTIs, has attracted tremendous attention. Unlike conventional TIs, HOTIs possess topological states in lower dimensions. For instance, 2D HOTIs host the salient features of gapped 1D edge states and in-gap topological 0D corner modes in a finite-sized sample. 3D HOTIs can exhibit a hierarchy of 2D surface states, 1D hinge states, and 0D corner states (Fig. 2.9). As the topological states can appear in multi-dimensions, HOTIs have not only enriched the topological physics, but also paved the way for applications, such as topologically localized modes with high quality factors, energy harvesting, and

topological sensors. The existing works on acoustic HOTIs are mainly based on three mechanisms, namely, the quantized bulk multipole moments, the nontrivial dipole moments, and the multidimensional TPTs.

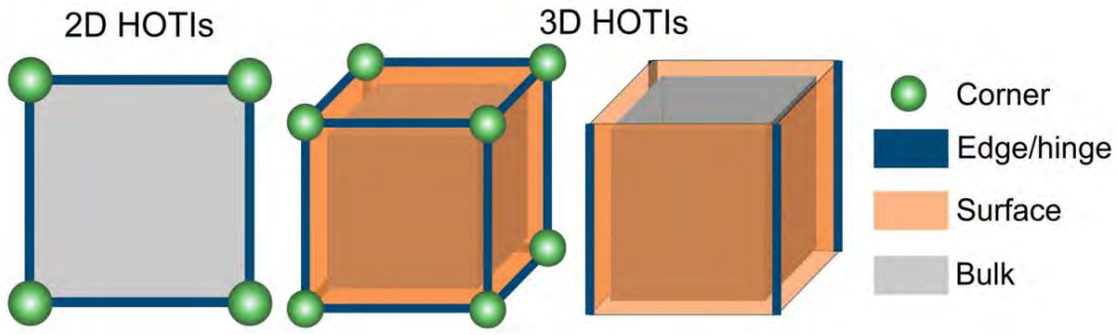

Figure 2.9 Schematic diagrams of HOTIs in two and three dimensions [64].

The earliest investigations were focused on achieving lattices with multipole moments, which were firstly proposed by Benalcazar, Bernevig and Hughes (BBH) [74, 75]. The BBH model contains both positive and negative couplings based on the TBM and constructs a 2D lattice with a quantized bulk quadrupole moment and a 3D lattice with a quantized bulk octupole moment. The nested Wilson-loop [74, 75] or the many-body multipole operators [76, 77] are two main methods to theoretically characterize the nontrivial multipole moments. As the implementation of opposite coupling signs in natural materials is a challenging topic, most experimental observations of HOTIs have been conducted in artificial structures, while only a few real materials with HOTIs were reported [78, 79]. In airborne acoustics, by judiciously engineering the coupling waveguides, the positive and negative couplings are successfully achieved [33, 34], as indicated in Fig. 2.10(a). In addition, the nontrivial quadrupole moments can also be realized, without the help of BBH models, by designing a non-symmorphic acoustic lattice [Fig. 2.10(b)] respecting p4g group symmetry [80]. In parallel, quantized higher moments were also studied in acoustic

lattices, including the octupole moment in 3D structure [33] and hexadecapole moment in a 1D structure by dimensional reduction [81].

For the acoustic HOTIs with non-trivial dipole moments, a great number of artificial structures based on cavity-waveguide configurations or scattering-type lattices show great functionalities in experimental demonstrations, due to their flexible manipulations on coupling strengths. These investigations were conducted in various 2D lattices, including Kagome crystals in Fig. 2.10(c) [35, 82], and triangular crystals [83]. In 3D cases, the 2D surface states, 1D hinge states, and 0D corner states can be observed in succession, showing bulk-surface-hinge-corner correspondence [84-86], as depicted in Fig. 2.10(d).

The acoustic HOTIs due to multidimensional topological phase transitions have been realized in a 2D square lattice with glide symmetry [87] and a 3D honeycomb lattice with bilayer chiral structure [58]. This mechanism indicates that the higher-order corner (hinge) states is only dependent on the edge (surface) topological phases. In the 2D acoustic HOTI, the topological invariants on the two perpendicular boundaries are different, giving rise to a domain wall at the intersecting corners of the two boundaries, which corresponds to the higher-order corner states [Fig. 2.10(e)].

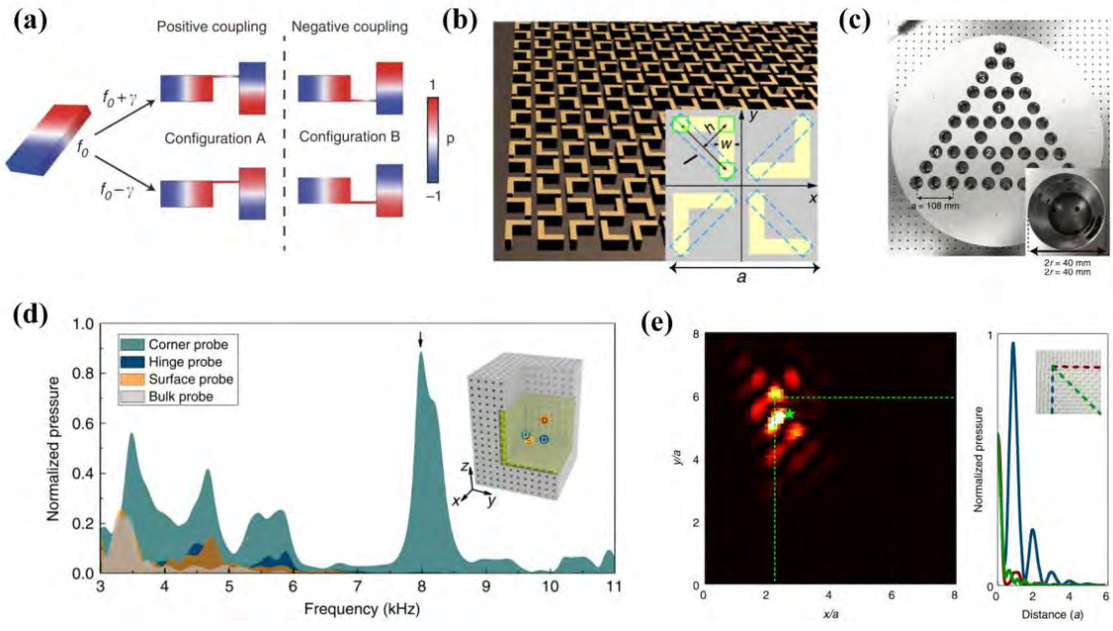

Figure 2.10 Acoustic HOTI. (a) Acoustic design of positive and negative coupling strengths [33]. (b) A non-symmorphic acoustic lattice used to achieve quadrupole moment [80]. (c) An experimental kagome lattice sample [35]. (d) Measured transmission spectra for corner, hinge, surface and bulk modes [84]. (e) Measured field profile for the corner states [87].

2.3 Elastic Topological Insulator

The past decades have also witnessed increasing interest in controlling elastic wave by elastic metamaterials, further promoting the development of topological phononics. Compared with the fluid acoustic systems, elastic waves propagating in solid materials carry richer degrees of freedoms supporting both longitudinal and transverse modes, which can be utilized to create pseudospins to mimic the QSHE in topological physics. Besides, elastic TIs also possess some unique advantages in phononic information transmission, such as extensibility toward integrated devices, robustness against temperature and air flow variations, and relatively lower attenuation than airborne sound. Therefore, elastic TIs have potential to provide

robust designs and unparalleled functionalities for manipulating elastic waves especially for future chip-scale elastic devices.

2.3.1 One-dimensional Elastic Topological Insulators

In accordance with the aforementioned acoustic TIs, our review takes the SSH chains as a starting point to present the recent development of 1D topological phases in elastic wave systems [88-92]. Huang et al. [89] connected two solid elastic plates with different Zak phases to form the topological interface and realized the elastic counterpart of the SSH model with interface states of shear horizontal guided wave. The designed SSH chain and the corresponding transmission spectrum including the non-trivial topological band gaps are depicted in Fig. 2.11(a). Another strategy to achieve an elastic analogue of SSH model is experimentally demonstrated in a highly tunable cylindrical granular particle [90]. The intracell and intercell coupling strengths can be modified by shifting the angles between the adjacent cylinders, thereby leading to a nontrivial topological band gap. Figure 2.11(b) illustrates the topological phase transition corresponds to three different configurations of the infinite chain.

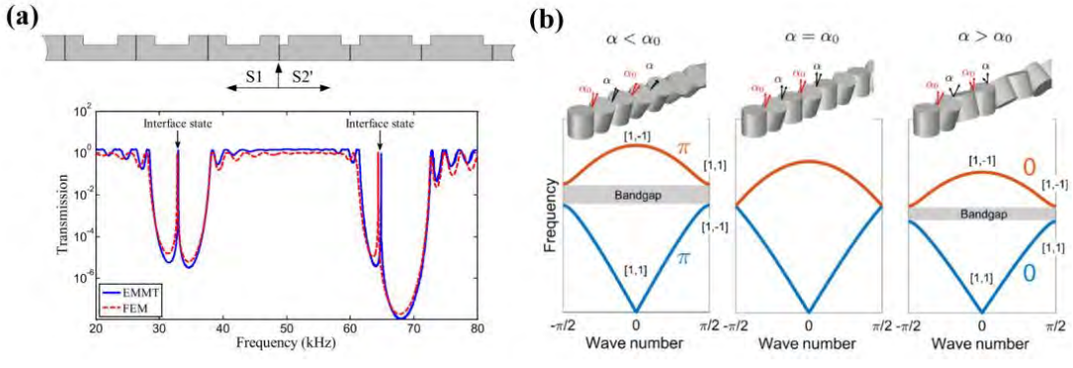

Figure 2.11 Elastic analogues of the 1D SSH model. (a) Topological interface states implemented in shear horizontal guided waves [89]. (b) Topological nontrivial band gap realized in cylindrical granular particles [90].

2.3.2 Two-dimensional Elastic Topological Insulators

As mentioned in the above section on acoustic systems, achieving the QHE needs to introduce circulating air flow to break the $\boldsymbol{T}$ symmetry. This strategy also applies to elastic systems, and the rotating parts are straightforwardly available by using the mechanical components like gyroscopes or direct current motors. One effective way to obtain the elastic analogues of QHE is to utilize the chiral nature of gyroscopes [93]. By arranging the gyroscopes in a 2D honeycomb lattice with their top tips fixed by mass blocks, the $\boldsymbol{T}$ symmetry is broken due to the rotating motion of gyroscopes, giving rise to a topologically nontrivial phase [see Fig. 2.12(a)]. When all the mass blocks are replaced by gyroscopes with small DC motors [see Fig. 2.12(b)], a topological nontrivial gap is formed and populated only by edge states that propagate unidirectionally and unaffected by defects [94].

The first experimental implementation of the elastic counterpart of QSHE was presented in a discrete oscillator system [95], in which each lattice site has two pendulums to obtain a local Kramers pair. Moreover, in contrast to acoustic wave systems, elastic waves have more polarizations, which can be directly used to create pseudospins in QSHE via polarization hybridization. As an example, Mousavi et al. [96] proposed a thin plate with holes arranged in a triangular lattice to realize the topologically protected helical edge states due to the accidental degeneracy between the symmetric (S) and anti-symmetric (A) Lamb waves. These two vibration modes (S-modes are mainly longitudinal vibrations and A-modes are predominantly bending vibrations) can be viewed as two degrees of freedoms, viz., polarizations. Moreover,

as a triangular lattice naturally exhibit DPs, each vibrational mode can possess one set of DPs. By deliberately tuning the two sets of DPs coincide, the double DPs are formed. Then, by breaking the mirror symmetry along the *z* direction, the double DPs are lifted, accompanied by the two pseudospins, as shown in Fig. 2.12(c). This idea was later implemented in an experiment with a simplified design in which holes in the plate are utilized to tune the DPs of two vibration modes [97]. At the same time, Yu et al. [98] experimentally demonstrated another elastic QSHE in perforated thin plates by adjusting the distances among adjacent holes. As illustrated in Fig. 2.12(d), the achieved helical edge states are topologically protected and exhibit a high-quality elastic transport along the designed path.

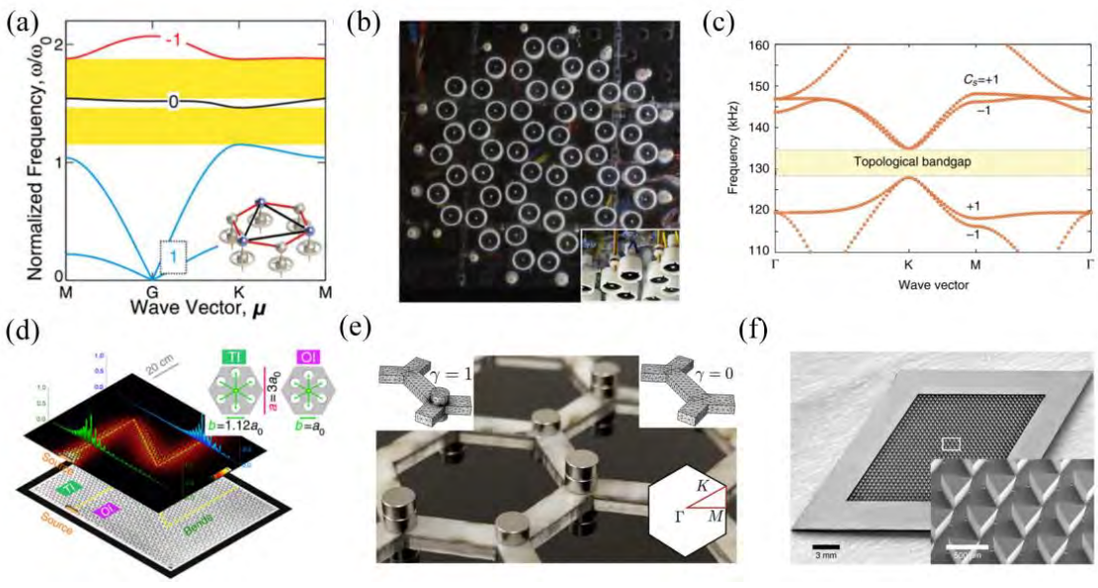

Figure 2.12 Elastic topological insulator in 2D structures. (a) Band diagram of the honeycomb gyroscopic lattice. The inset is the schematic of a unit cell [93]. (b) Experimental sample of the gyroscopic lattice [94]. (c) Band diagram with lifted double DP [96]. (d) A topological waveguide with a Z-shape realized in a perforated thin plate [98]. (e) Experimental sample for elastic QVHE with unbalanced masses [99]. (f) Experimental sample fabricated on the silicon chip with QVHE [100].

The QVHE can also be achieved in elastic wave systems. Most of the existent works about achieving elastic QVHE share the same mechanism, namely, lower the ***P*** symmetry in the lattices. It includes the specific approaches of introducing a strain field [101], adding masses at the particular sites [99] [Fig. 2.13(e)], rotating the triangular pillars [100] [Fig. 2.13(f)] and so on [102, 103].

2.3.3 Three-dimensional Elastic Topological Insulator and Topological Semimetals

Parallel to the growth of 2D elastic TIs, a great deal of effort has been dedicated to the study of topological phases in 3D elastic structures, including TIs, Weyl semimetals, topological nodal lines, etc. All of them can exhibit the robust surface transport against defects without being restricted to a specific plane. The elastic 3D TIs [104, 105] feature the topological band gap that is occupied by gapless surface states. Huo et al. [104] experimentally implemented a 3D elastic TI based on the monolayer-stacked honeycomb lattice fabricated by aluminum material [see Fig. 2.13(a)]. By stacking the original monolayer lattice into bilayer and rotating one layer by an angle of 60°, the out-of-plane mirror symmetry are broken, leading to the 2D topological surface states dependent on layers, as shown in Fig. 2.13(b).

Besides the 3D gapped TIs, another type of topological phase also exists in 3D elastic structures, i.e., the 3D gapless topological phases akin to the 3D Weyl semimetals [106-108]. The model proposed by Shi et al. [106] described an elastic counterpart of Weyl semimetal by stacking honeycomb lattice with chiral interlayer coupling composed of thin beams, as illustrated in Fig. 2.13(c). This model hosts

elastic oppositely charged Weyl points that are connected by elastic Fermi arcs [Fig. 2.13(d)].

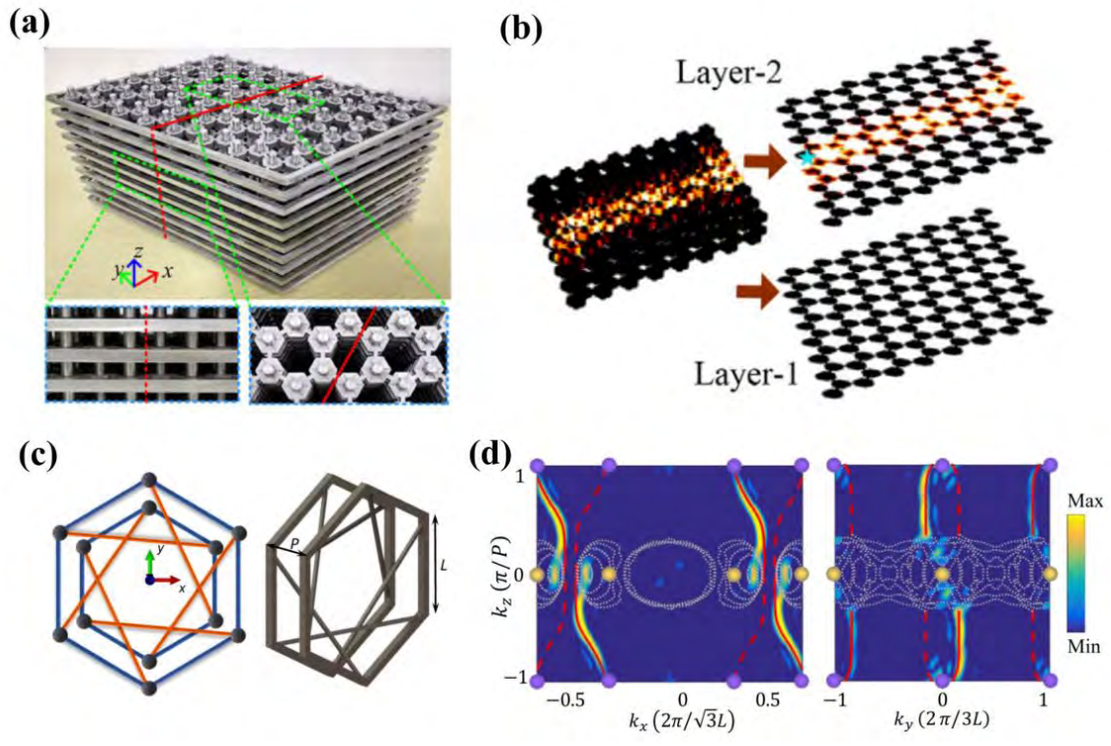

Figure 2.13 Elastic TIs and Weyl semimetals in 3D structures. (a) Experimental sample of 3D elastic TI based on the monolayer-stacked honeycomb lattice. The side and top views of the 3D structure are shown in the bottom panels. (b) The simulated displacement field profiles of the layer-dependent surface states [104]. (c) Schematic for the stacked lattice (blue) and chiral interlayer coupling (orange). The right panel is the slanted view. (d) Spatial Fourier transformed contours of the real-space displacement field profiles of the surface states on the *x*-*z* (left) and *y*-*z* plane (right), respectively, showing the Fermi arcs [106].

2.3.4 Higher-order Elastic Topological Insulator

Higher-order topological phases based on the quantized bulk multipole moments, the nontrivial dipole moments, and the multidimensional TPTs have also been realized in elastic wave systems [109-113]. The pioneering work by Serra-Garcia et al. [112] realized an elastic counterpart of quadrupole TI based on perturbative elastic

metamaterials consisting of resonant silicon plates linked by thin bent beams [Fig. 2.14(a)]. In their design, the shapes and positions of the linking beams mediate the positive and negative coupling strengths λ and γ, which can form a nontrivial band gap between two pairs of doubly degenerated bands.

Motivated by the HOTIs induced by the dipole moments, similar experiments were also conducted on the 2D mechanical Kagome lattice [111] and honeycomb lattice [113] to observe the in-plane and out-of-plane second-order TIs, respectively. The Kagome lattice, composed by thin disks and bivalued width beams, is shown in Fig. 2.14(b). The beams with different widths are used to turn the intra-cell coupling and inter-cell coupling strengths. The honeycomb lattice is depicted in Fig. 2.14(c), and the lengths of the connected beams are utilized to adjust the coupling strengths. Both of them can lead to the in-gap higher-order corner states. The multidimensional topological phase transitions mechanism has also been extended to elastic systems without the need of negative coupling. Huo et al. [110] proposed an elastic HOTI based on this mechanism in a square lattice consisting of perforated plate with pillars [Fig. 2.14(d)].

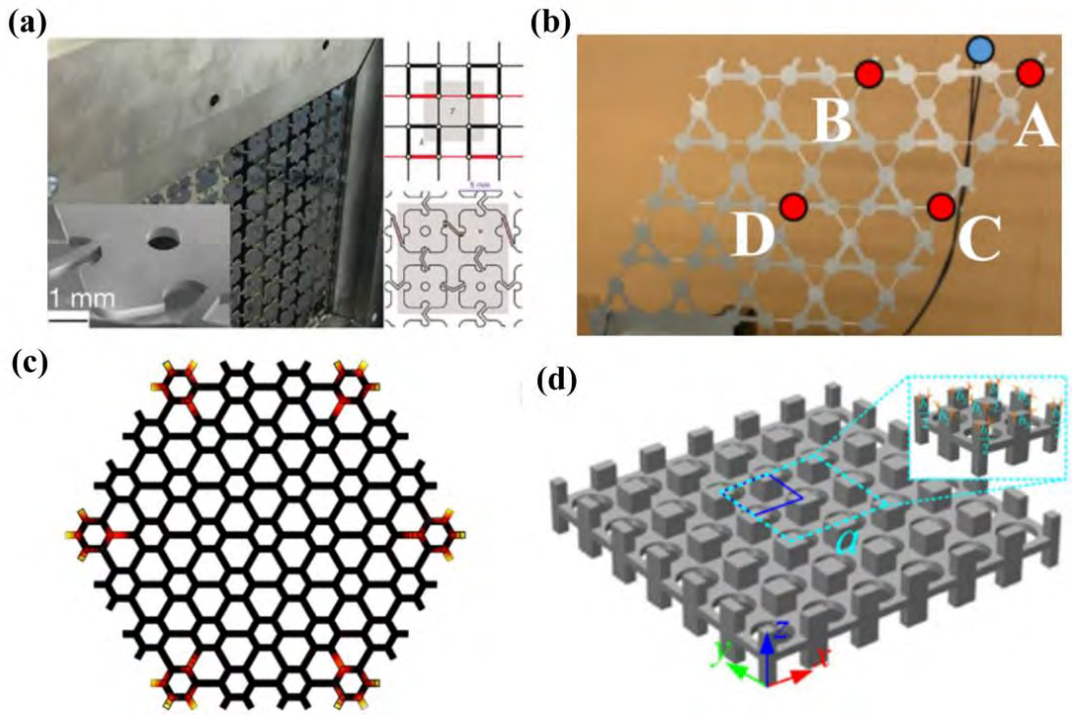

Figure 2.14 Elastic HOTI. (a) Implementation of an elastic QTI based on perturbative elastic metamaterials [112]. (b) Experimental sample of an in-plane HOTI based on a Kagome lattice [111]. (c) A out-of-plane HOTI based on a honeycomb lattice [113]. (d) An elastic HOTI based on a square lattice [110].

2.4 Non-Hermitian Topological Physics

The above topological phenomena in acoustic and elastic lattices are all based on the hypothetically lossless condition, which guarantees real-valued eigenfrequencies, orthogonal eigenstates together with well-defined topological invariants. However, acoustic and elastic systems are indeed nonconservative systems involving energy exchange and interactions with the ambient environments (due to their intrinsic loss ubiquitous in open systems), resulting in the breakdown of Hermiticity. In this regard, taking into consideration the effect of losses represents a more realistic scenario and is thus essential for practical applications. More interestingly, non-Hermiticity, when judiciously designed via loss/gain or asymmetric coupling, can also lead to the TPT

behaviour, bringing new insights into the exploration of topological physics. In this section, two critical subjects in the non-Hermitian topology, namely, the exceptional degeneracies and non-Hermitian line band gaps, are introduced and reviewed by concrete examples.

The non-Hermitian PT symmetry and EPs have been incorporated in a large number of studies in non-Hermitian physics. When the non-Hermitian parameters are tuned (often by controlling the on-site gain/loss), the real eigenvalues can be changed to complex ones, known as the PT phase transition [114], in which the transition point is a so-called EP [Fig. 2.15(a)]. The system's Hamiltonian gives rise to the coalescence of both eigenvalues and eigenvectors at the EP [115], which leads to intriguing phenomena such as loss-induced lasing [116], unidirectional invisibility [117], and unidirectional sound focusing [118].

As aforementioned acoustic and elastic systems with Hermitian assumption, the nontrivial topological band gap (often referred to as insulators) is important for determining topological phases [119]. However, when it comes to their non-Hermitian counterparts, the definitions of band gaps become less straightforward due to the complex nature of non-Hermitian eigenvalues. In general, the complex band gaps show either a line or a point style [120]. Here, we limit our discussion on the line gaps, which refer to the scenarios where the complex eigenvalues are split by 1D lines. The line gaps can be modulated to overlap with the real or imaginary axis in the complex plane, forming the real or imaginary line gap, respectively [Fig. 2.15(b)].

It has been demonstrated that line-gapped non-Hermitian matrix can be deformed

into a Hermitian or an anti-Hermitian Hamiltonian [120]. Therefore, the line-gapped non-Hermitian systems share the similar topological characteristics of its Hermitian counterparts, and the topological invariants can also be obtained according to the Hermitian definition [Eq. (1.2)] after the eigenvectors are orthogonalized in advance.

Here, we take the complex SSH model with on-site gain and loss [121, 122] as an example to specify non-Hermitian topological phenomena. As illustrated in the upper panel of Fig. 2.15(c), the model is composed of the typical dimerized chain with alternating gain and loss (or only be alternating on-site losses to simplify the experimental set-up [20]). By setting appropriate coupling and on-site gain/loss parameters, a real line gap with mid-gap edge states is realized [bottom panel of Fig. 2.15(c)], consistent with its Hermitian counterpart [38]. In 2D TBMs, it has been theoretically [123, 124] and experimentally [19, 125] demonstrated that TPTs and HOTIs can also be realized solely by introducing on-site gain and loss. Gao et al. [19] showed that solely by inserting lossy media in particular acoustic resonant cavities, non-Hermitian counterpart of quadrupole TI with higher-order topological corner states can be obtained [Fig. 2.15(d)]. Zhao et al. [126] demonstrate that by selectively pumping a part of the lattice, the wave can propagate along the gain-loss interfaces in the arbitrary positions of the lattice, leading to the reconfigurable topological edge transportation [Fig. 2.15(e)].

Up to the starting time of my PhD study (September 2020), there was an increasing attention paid to non-Hermitian topological phases in acoustic and elastic wave systems, but very few works were reported. To better organize the thesis, the introduction on specific topics of non-Hermitian topological physics will be

presented as a separated section at the beginning of each chapter.

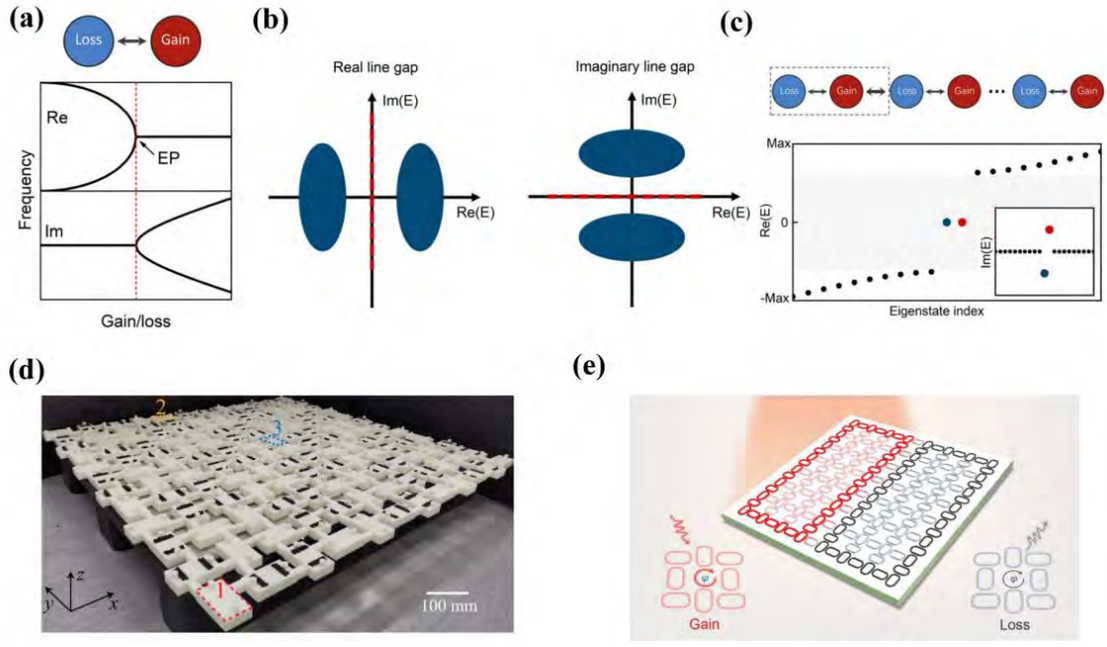

Figure 2.15 Non-Hermitian topological phenomena induced by the on-site gain/loss. (a) The normal EP in a two-level system. (b) The real (left) and imaginary (right) line gaps. (c) The complex SSH model with alternating gain and loss (upper). The calculated eigenvalues if the SSH chain (lower) [64]. (d) The experimental sample of the non-Hermiticity induced HOTI [19]. (e) The reconfigurable topological interfaces enabled by selectively pump the lattice [126].

2.5 Summary

In this chapter, the basic concepts, constituents as well as their concrete implementations of TIs in acoustic and elastic systems are briefly introduced and classified. Clearly, topological phononics has enabled remarkable sound wave manipulation, like topological surface/edge transports and corner localizations with robustness against various defects, which can hardly be realized by traditional methods. More importantly, the study of acoustic and elastic topological phenomena

can be combined with non-Hermitian physics and inspires various non-Hermitian topological phenomena due to the inevitably lossy nature and feasible control of gain/loss in artificial acoustic and elastic lattices, opening new possibilities for both frontier physics research and potential practical applications.

CHAPTER 3

Hermitian and Non-Hermitian Topological Edge States in One-dimensional Perturbative Elastic Metamaterials

3.1 Introduction

As discussed in section 2.3.1, some elastic TIs based on the SSH model have been studied without considering any damping effect unavoidable in solid materials. This ignorance of damping undoubtedly restricts the application of the topological edge states. In fact, the concept of non-Hermiticity in TIs has much more profound significances. Substantial theoretical works about the fundamental bulk–edge correspondence collapse [21-23] and new concepts of topological invariants specific to non-Hermitian settings [127, 128] have been put forward. In parallel, considerable experimental efforts were made in non-Hermitian systems to validate adjustable localization states with robustness [129, 130], skin effect due to the nonreciprocal hopping strengths [123, 131, 132] and topological lasers [133]. In these systems,

active sections are utilized to pump boundary modes thus enhancing the stability of topological boundary states or break time-reversal symmetry to create new kinds of topological insulators. As a matter of fact, recent experiments have shown that topological states in non-Hermitian systems can also be obtained by solely passive variant (loss) in acoustic systems, which significantly simplifies the experimental processes [19, 20].

The non-Hermitian versions of the SSH model have also been extensively investigated and experimentally implemented in electric circuit [134], microwave [135] and acoustic lattice [20]. However, the practical realization of such non-Hermitian SSH model in elastic wave system is yet to be fully investigated, especially when it comes to the implementation and modulation of the required non-Hermitian parameters.

In this chapter, we theoretically and experimentally investigate two different types of topological edge states induced respectively by alternating hopping strengths (under hypothetically Hermitian condition) and non-Hermiticity, with elastic analogues of the SSH model consisting of square plates and thin beams together with additional damping (AD) layers. In the absence of non-Hermitian modulation, a well-defined Zak phase can depict the topological characteristics of the edge state for non-trivial and trivial structures, but the corresponding measured result is inevitably affected by

the intrinsic material damping. For the non-Hermitian case, uneven dampings, purposely introduced through absorptive damping layers attached to particular plates, result in topological edge states characterized by a specific topological invariant called biorthogonal polarization.

3.2 Hermitian Topological Edge States Based on Su-Schrieffer-Heeger Model

3.2.1 Tuning the Coupling Strength Between the Plates

The elastic topological edge states are realized by utilizing the notion of perturbative elastic metamaterials [112, 136] , which can be modulated to an elastic counterpart of the SSH chain. The metamaterials can be regarded as a periodically arranged 1D chain of atoms with alternating hoppings, intra-unit coupling γ and inter-unit coupling λ between the nearest neighbors. Each atomic site is replaced by an elastic resonant plate which shows linear resonant mode weakly coupled with the resonant modes of the nearest adjacent plates by connected thin beams. The lengths and widths of the resonant plates and the thin beams are 80 mm × 80 mm and 45 mm × 45 mm, respectively. As a result, the lattice constant a = 250 mm. This elastic metamaterial is fabricated by laser cutting technique from an aluminum alloy plate (density ρ = 2700kg/m^3, Poisson's ratio v = 0.33) with thickness of 2.94 mm.

Before exploring the topological phases of the periodic chain, we firstly display how

the intra-unit coupling γ and inter-unit coupling λ can be adjusted according to our request, in which the material loss is ignored in theory but unavoidably exists in the fabricated sample. Here, we only focus on the first non-rigid-body resonant mode of the single plate [see the upper inset in Fig. 3.1(a) at 1471 Hz, which shows two perpendicular nodal lines (white dotted lines in Fig. 3.1(a)) intersecting at the center of the plate in the out-of-plane component of displacement (u_z)]. This mode is largely separated from other higher-order modes, which effectively avoids other unwanted modes appearing in the frequency of our interest. For double-plate shown in Fig. 3.1(a), the coupling strength $|\kappa| = |f_2 - f_1|/2$ of the first non-rigid-body resonant mode is closely related to the geometric parameters of the connecting beam, namely, width *w*, distance *h* and length *l*. As indicated by the simulated results plotted in Fig. 3.1(b)-(c), the coupling strength gradually increases with the growth of the beam width *w* or the distance to the horizontal nodal line *h*, determined by the mode shape in Fig. 3.1(a). The growth of the beam length *l* leads to a declined hopping strength, remarkably for small l/l_0 value and smoothly for large l/l_0 value. w_0 = 4 mm, h_0 = 10 mm, and l_0 = 45 mm are the parameters picked in the following simulations and experiments. It is worth noting that the central frequencies of the coupled double-plate may deviate from the single-plate resonant frequency (1471 Hz) due to the introduction of coupling beams.

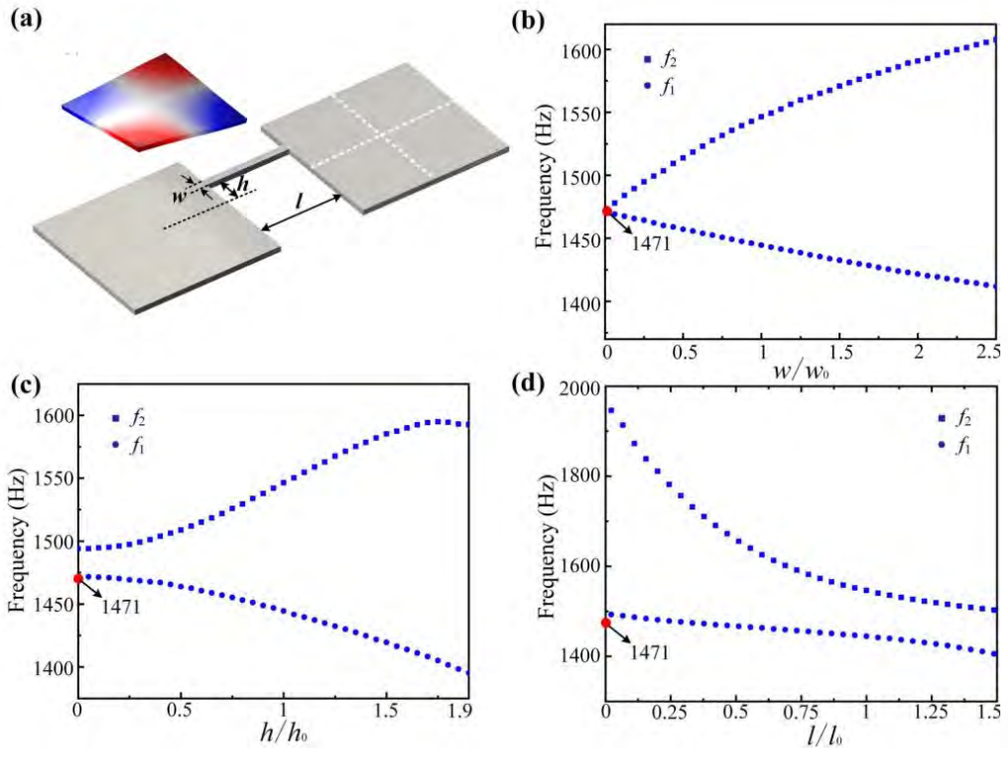

Figure 3.1 Parameter dependencies of the split eigenfrequencies for the double-plate structures. (a) Schematic of the double-plate structures. (b)-(d) The two split eigenfrequencies plotted as a function of, w/w_0 , h/h_0 and l/l_0 respectively. 1471 Hz is the eigenfrequency of the single plate.

3.2.2 Band Diagrams and Zak Phase of the Hermitian Unit Cell

Here we simply tune the beam close to or away from the horizontal nodal line to decrease or increase the coupling strength. The unit cells of the non-trivial and trivial 1D chains are shown in Figs. 3.2(a) and 3.2(b), respectively, which can be well captured by the TBM with the effective Hamiltonian matrix being written as

$$H(k)=\begin{pmatrix} f_0 & \kappa \\ \kappa^* & f_0 \end{pmatrix} \tag{3.1}$$

where $\kappa=\gamma+\lambda e^{-ika}$, k is the Bloch wavenumber, and f_0 is the first non-rigid-body resonance frequency. For the case of $\gamma=\lambda=24$ Hz (the beams are aligned in the x

direction), the band diagram shows a linear degeneracy at the BZ edge, illustrated by the grey dotted lines in Figs. 3.2(c) and 3.2(d). As we change the beam locations such that $\gamma < \lambda$, a complete band gap appears [bule dotted lines in Fig. 3.2(c)], leading to a coupling dimerization. By fitting the eigenvalues obtained by solving Eq. (3.1) to the simulated band diagram in Fig. 3.2(c), we get the tight-binding parameters as: f_0 = 1536 Hz, γ = 10 Hz and λ = 50 Hz [see Fig. A1(a) in Appendix A]. By exchanging the locations of the inter-unit and intra-unit beams (γ = 50 Hz, λ = 10 Hz), the same band diagram can be obtained. However, the topological phases of these two cases are totally different.

The topological property of an isolated bulk band can be characterized by some certain topological invariants, which, for 1D lossless elastic system here, can be denoted by Zak phase. Because of the periodicity of the 1D chain, the Zak phase can be calculated by integrating the Berry curvature over the first BZ, written as

$$\theta_n^{Zak} = \int_{-\pi/a}^{\pi/a} \left[i \int_{unitcell} \frac{1}{2\rho c^2} \xi_{n,k}^*(x) \partial \xi_{n,k}(x) dx \right] dk \tag{3.2}$$

where $\xi_{n,k}(x)$ is the Bloch eigenfunction for the n^{th} band at a specific wavenumber k, factor $1/(2\rho c^2)$ denotes an energy density operator for elastic wave systems. The Zak phase can also be obtained by utilizing the Wilson-loop approach [14], namely, rewriting Eq. (3.2) into a discretized form:

$$\theta_n^{Zak} = -\operatorname{Im} \sum_{i=1}^{N} \ln \left[\int_{unitcell} \frac{1}{2\rho c^2} \xi_{n,k_i}^*(x) \partial \xi_{n,k_{i+1}}(x) dx \right] \tag{3.3}$$

It takes quantized value of π (Fig. 3.2(c)) or 0 (Fig. 3.2(d)), corresponding to the topologically non-trivial case ($\gamma < \lambda$) or trivial case ($\gamma > \lambda$).

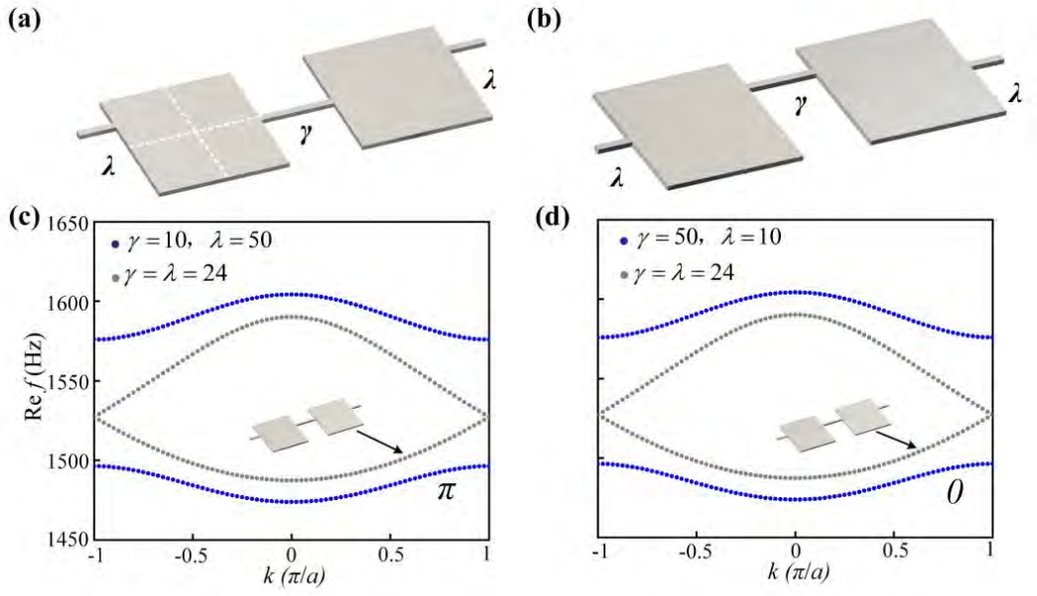

Figure 3.2 Band diagrams of the Hermitian unit cells. Schematics of the (a) non-trivial and (b) trivial unit cells for the elastic SSH chains. (c), (d) Corresponding band diagrams (the bule dotted lines) of the lattices in (a) and (b), respectively. The Zak phase is π for $\gamma < \lambda$ and 0 for $\gamma > \lambda$.

3.2.3 Topological Edge States in Finite-Sized Hermitian Chains

A nonzero Zak phase indicates the existence of localized modes at the edges or the interfaces (between trivial and non-trivial structures) within the band gap frequency range [137]. To confirm this, we consider in simulation two types of finite-sized elastic chains consisting of 5 non-trivial and trivial unit cells (10 connected square plates), respectively. Two topologically protected in-gap edge states [Fig. 3.3(a)] can be observed among the 8 bulk modes in the non-trivial chain due to the Zak phase π mentioned above [Fig. 3.2(c)]. On the contrary, only 10 bulk modes evenly split by a complete gap emerge in the trivial chain [Fig. 3.3(b)], as a result of the zero Zak phase [see Fig. 3.2(d)]. In comparison, for the 1D chain with the same inter-unit and

intra-unit couplings, no obvious gap exists over the concerned frequency range. The simulated edge state profiles presented in Fig. 3.3(c) manifests that the out-of-plane component of displacement is mainly localized on the two boundaries of the topologically non-trivial chain. Here, both ends of the chains are applied with fixed boundary conditions to meet the requirement of the TBM with perturbative elastic metamaterials (see Fig. A2 in Appendix A) [112].

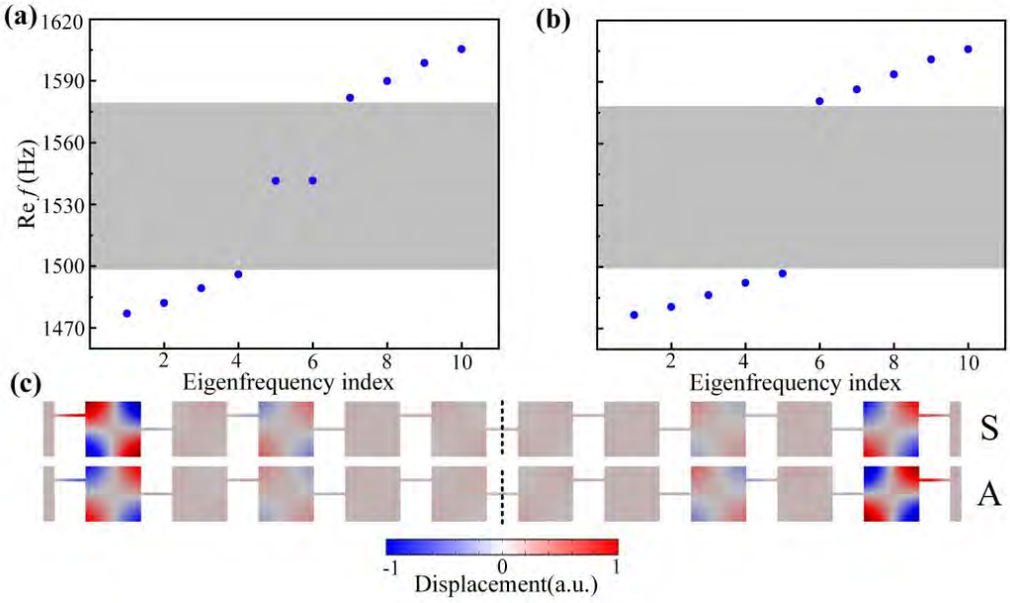

Figure 3.3 Hermitian topological edge states. (a), (b) Numerically evaluated eigenfrequencies for finite-sized non-trivial and trivial 1D chains (5 unit cells), respectively. (c) Simulated out-of-plane displacement component of the edge states at 1544 Hz. Two edge states are respectively mirror symmetric and asymmetric about the middle-dotted line.

3.2.4 Robustness of the Hermitian Topological Edge States

Here we assess the robustness of the Hermitian topological edge states against random defects on the resonance frequencies and the coupling strengths, which are also two main sources of defects in the experiments due to fabrication errors. The

calculations are based on the TBM as it possesses good agreement with the full-wave simulation thus can save much time in simulation. The resonance defects on plate *i* are added by shifting the resonance frequency terms (diagonal terms in Hamiltonian matrices) to $f_0(1+df_i)$, where f_0 is the resonant frequency without the random defects and df_i are random numbers distributed from $-\delta_w$ to δ_w with δ_w being the resonance defect strength. In a similar way, the coupling defects on coupling beam *j* are introduced by replacing the coupling term (off-diagonal terms in Hamiltonian matrices) with $\kappa_0(1+d\kappa_j)$, where κ_0 denotes the coupling strength without the random defects and $d\kappa_j$ are random numbers distributed from $-\delta_\kappa$ to δ_κ with δ_κ being the coupling defect strength.

The resultant real parts of eigenfrequencies are plotted in Fig. 3.4 as a function of δ_w or δ_κ, respectively for the 1D finite-sized Hermitian [Figs. 3.4(a) and 3.4(b)] chains. With the increasing of δ_κ, the edge states in Figs. 3.4(a) keep emerging near $f_0 = 1536$ Hz, verifying their robustness against the coupling defects. On the other hand, with the increasing of δ_w, the eigenfrequencies of the edge states in Figs. 3.4(b) gradually spread, showing that they are not very robust against resonance defects because these topological edge states are protected by chiral symmetries [138].

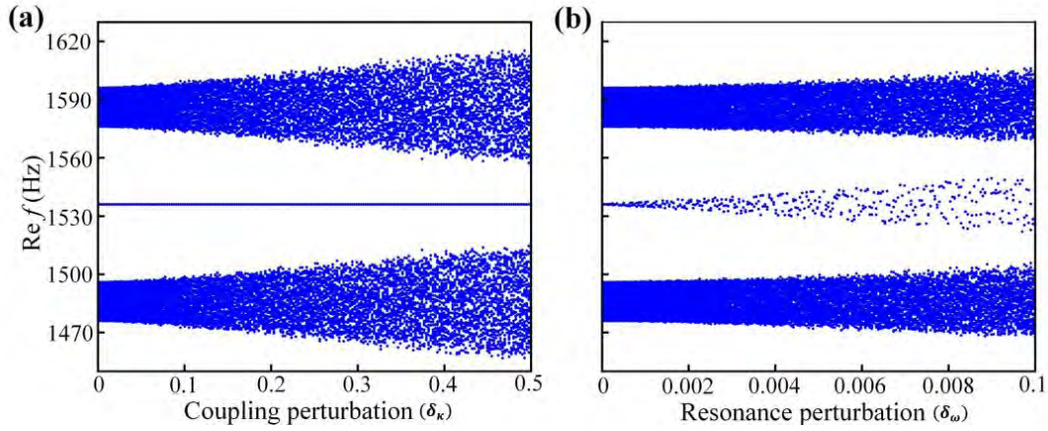

Figure 3.4 Robustness of the edge states. The eigenfrequencies at different strengths of (a) random coupling perturbations and (b) random resonance perturbations for the 1D finite-sized Hermitian chain.

3.2.5 Experimental Validation of the Hermitian Chain

To examine the topologically-protected edge states experimentally, we fabricated two configurations of finite-sized chains (5 unit cells) composed of the trivial and non-trivial unit cells, respectively, by laser cutting technique. In experiments, the samples are clamped at both ends to imitate fixed boundary conditions in simulations and excited by an electromagnetic shaker [Fig. 3.5(b)]. The resultant force at the excitation point, $F(t)$, is recorded by a force transducer (B&K 8200) and then amplified through a charge amplifier (B&K 2635). A Polytec laser vibrometer is used to launch a periodic chirp signal with frequency ranging from 0 Hz to 3.2 kHz. The signal is then amplified by a power amplifier (B&K 2706) and sent to the shaker. The vibration in the out-of-plane direction was captured by the laser vibrometer to obtain the velocity/displacement/acceleration response at the measured point, which gives the forced response signal $X(t)$. After Fourier transformation, the frequency response

function (FRF) can be achieved as

$$H(\omega) = \frac{X(\omega)}{F(\omega)} \tag{3.4}$$

where $X(\omega)$ is the velocity/displacement/acceleration response at the measured point, and $F(\omega)$ is the excitation force. The corresponding signal path in measuring all the FRF spectra in this study is shown in Fig. 3.5(a).

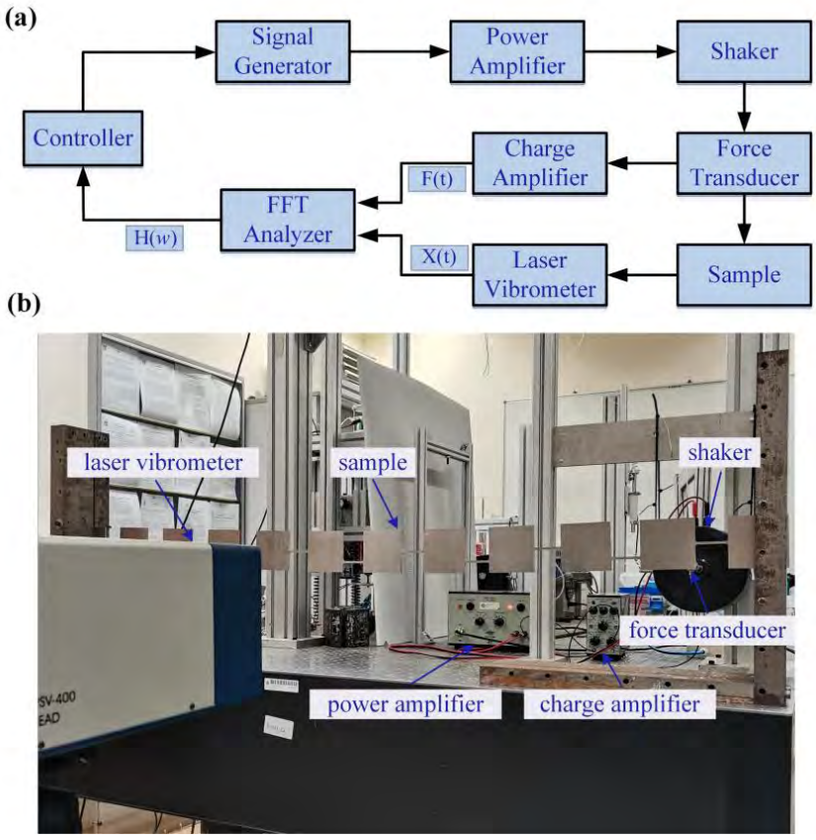

Figure. 3.5 Schematics of experiments. (a) Signal path in measuring all the FRF spectra. (b) Experimental set-up.

Two manufactured samples are displayed in Figs. 3.6(a) (non-trivial chain) and 3.6(b) (trivial chain). We measured the FRF curve at the outmost plates [the first plate in Figs. 3.6(a) and 3.6(b)] to evaluate the edge states and selected one arbitrary bulk

plate to assess the bulk states (both shaker and laser are located at the same plate). For the non-trivial configuration, two main resonance peaks, split by a band gap, can be observed in the bulk spectrum [blue circle curve in Figs. 3.6(c)], which show agreement with the two bulk state regions separated by the band gap from 1496 to 1581 Hz in Fig. 3.3(a). Different from the bulk spectrum, the measured FRF curve on an edge plate only has one dominant peak located around 1545 Hz in the band gap [the red circle curve in Fig. 3.6(c)], which corresponds to the simulated eigenfrequencies of the edge states in Fig. 3.3(a) (the spectrum from the other edge is similar). In contrast, as shown in Fig. 3.6(d), no obvious peak can be observed in the gap range in the FRF curves of the trivial chain, demonstrating the gap property in Fig. 3.3(b). It is worth noting that as we ignore the intrinsic material damping of the whole structures together with the vibro-acoustic coupling, the resonance should theoretically show infinitely small linewidth. Nevertheless, the resonance peaks are broadened because of the unavoidable non-Hermiticities from dissipative and radiative losses non-negligible in experiments.

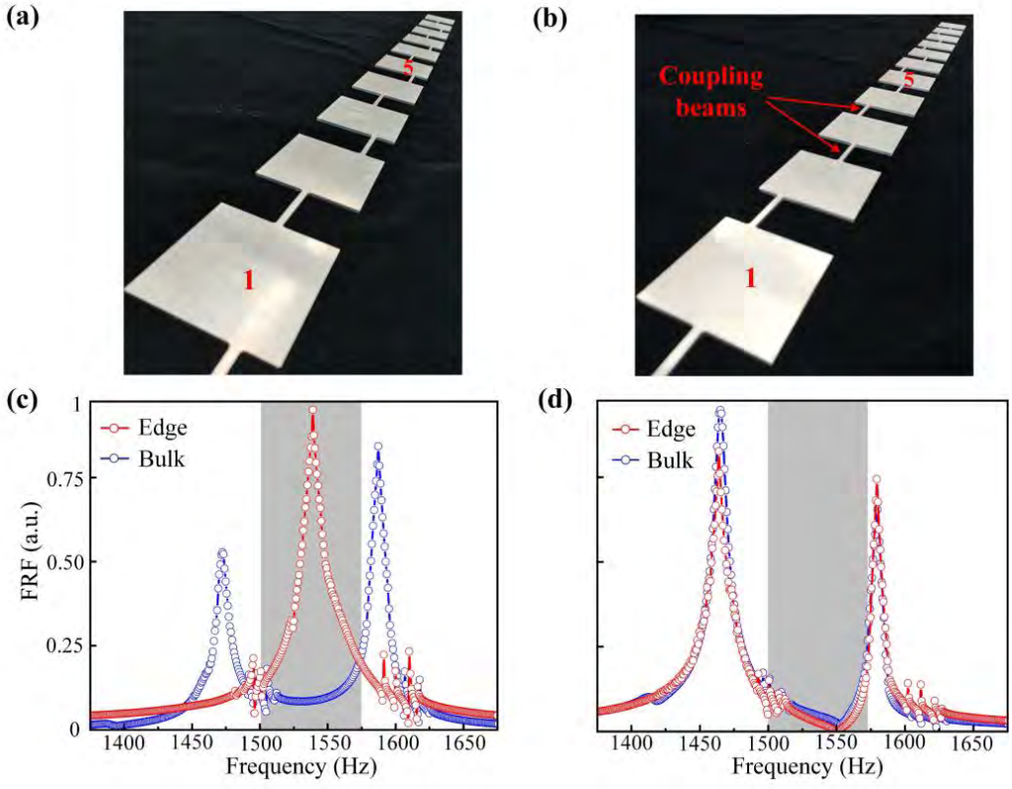

Figure 3.6 Forced responses of the finite-sized Hermitian SSH chains. Photos of the (a) non-trivial and (b) trivial elastic chain samples. (c), (d) Measured FRF spectra of the bulk (blue circle curve) and edge (red circle curve) plates for the non-trivial 1D chain (c) and trivial 1D chain (d), respectively. The gray regions indicate the complete band gap range.

3.3 Non-Hermitian Counterparts in Perturbative Elastic Metamaterials

3.3.1 Band Diagrams and Biorthogonal Polarization

Other than regarding as a negative perturbation to the topological phenomena, non-Hermiticity itself can also be utilized to obtain non-trivial topological phases. Specific to the elastic metamaterial in this study, we now consider a double-sized

unit cell comprised of four square plates connected by beams as depicted in Figs. 3.7(a) and 3.7(b). The degeneracy emerges at the BZ centre [blue solid lines in Figs. 3.7(c) and 3.7(d)] due to the band folding mechanism. After adding AD to two plates coloured in blue in Figs. 3.7(a) and 3.7(b), the degeneracy is opened, and complete band gaps emerge in the band diagrams [dotted lines in Figs. 3.7(c) and 3.7(d)]. Compared to the Hermitian case mentioned above, the double-sized unit cell is vital to lift the degeneracy, otherwise the band gap will be decreased by introducing on-site gains and/or losses [139] .

The two types of non-Hermitian elastic unit cells in Figs. 3.7(a) and 3.7(b) can be captured by the TBM with the same nearest-neighbor coupling terms κ, in which the effective Hamiltonian matrices, $H_1(k)$ and $H_2(k)$ for AD introduced respectively to the central and right two plates, take the forms of

$$H_{1(2)}(k)=\begin{pmatrix} (1+d_0 i)f_0^{'} & \kappa & 0 & \kappa e^{-ika^{'}} \\ \kappa & [1+(d_0+d_{1(2)})i]f_0^{'} & \kappa & 0 \\ 0 & \kappa & [1+(d_0+d_1)i]f_0^{'} & \kappa \\ \kappa e^{ika^{'}} & 0 & \kappa & [1+(d_0+d_{2(1)})i]f_0^{'} \end{pmatrix} \tag{3.5}$$

In the matrices, $a^{'} = 2a$ is the doubled lattice constant, $f_0^{'}$ is the first non-rigid-body mode resonance frequency, and d_0 and d_1 correspond to the intrinsic damping (ID) and AD, respectively, which are reflected by the imaginary part of the diagonal terms of the Hamiltonians ($d_2 = 0$). By fitting the eigenvalues calculated by Eq. (3.5) to the simulated band diagram in Fig. 3.7(c), we can obtain the tight-binding parameters as: $f_0^{'}=1133$ Hz , $\kappa=18.85$ Hz , d_0 = 0.0061, and d_1 = 0.041 [see Fig. A1(b) in Appendix A]. In these two types, uneven dampings of the four sites leads to the band

gap, different from the aforementioned Hermitian case that depends on dimerized couplings.

Here, a biorthogonal polarization [121, 123] is used to represent a more generalized topological invariant in complex field induced by non-Hermiticity. The left-right and right-left polarization vectors can be obtained by integrating the biorthogonal non-Abelian Berry curvature over the first BZ:

$$P_n^{LR(RL)} = \frac{1}{4\pi}\int_{-\pi/a}^{\pi/a} \left\langle \xi_{n,k}^{L(R)} \middle| i\partial_k \middle| \xi_{n,k}^{R(L)} \right\rangle dk \tag{3.6}$$

where the superscripts L and R of ξ denote the left and right eigenvectors of the Hamiltonian matrix after the normalization of $\left\langle \xi_{n,k}^{L} \middle| \xi_{n,k}^{R} \right\rangle = \delta_n$. As these two eigenvectors are orthogonal to each other, they can form a biorthogonal basis. To obtain a real-valued topological invariant, we define $p = P^{LR} + P^{RL}$ as the biorthogonal polarization. By utilizing the biorthogonal Wilson-loop approach, p is calculated to be 1/2 for the lower two bands of $H_1(k)$, which corresponds to a topologically non-trivial case. Meanwhile, p is 0 for $H_2(k)$ that corresponds to a trivial case. The colour scale in Fig. 3.7 (c) and (d) denotes the imaginary parts of the eigenfrequencies. For example, an eigenfrequency in red (or blue) means that the elastic wave undergoes a relatively higher (or lower) attenuation, related to the mode shape in which the displacement is mainly localized at the plates with (or without) AD treatment.

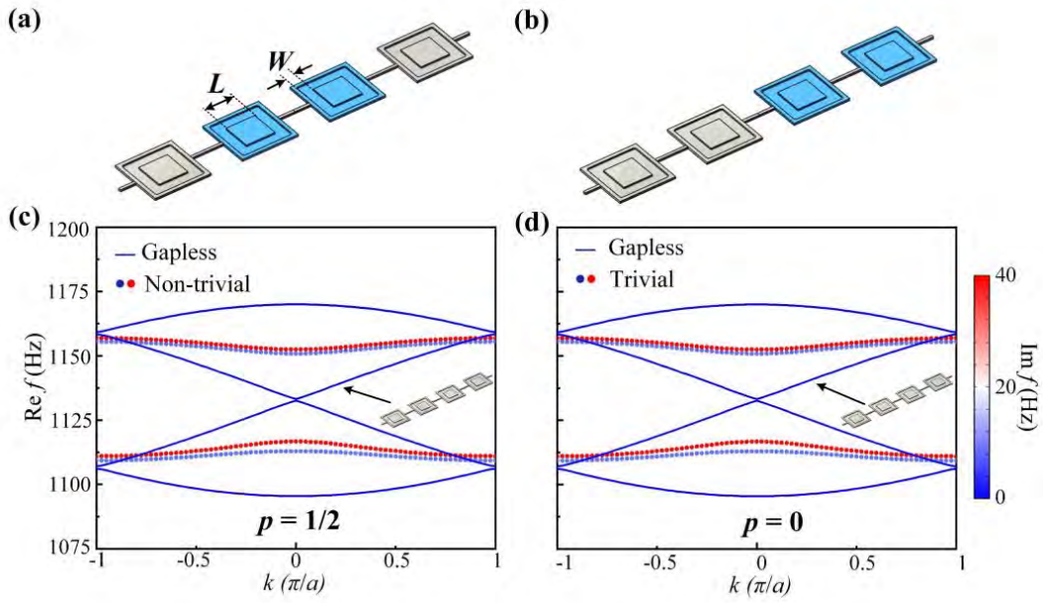

Figure 3.7 Band diagrams of non-Hermitian unit cells. (a), (b) Schematics of unit cells for non-Hermitian elastic SSH chains. L = 41 mm, W = 14.5 mm. (c), (d) Corresponding band diagrams (dotted lines) of the lattices in (a) and (b), respectively. The solid blue lines are the band diagram of unit cell without AD treatment indicated by the insets.

3.3.2 Topological Edge States in Finite-Sized Non-Hermitian Chains

Similar to the Hermitian case, we create two finite-sized elastic chains with 3 non-trivial and trivial unit cells (12 connected square plates), respectively, to evaluate the non-Hermitian topological edge states. Again, due to the nonzero topological invariant of the infinite chain with AD in the middle two plates, two topological in-gap edge states [Fig. 3.8(a)] are clearly observable among the 10 bulk states in the finite-sized non-trivial chain. And only 12 bulk modes separated by a complete gap emerge in the finite-sized chain with the trivial unit cells [Fig. 3.8(b)]. The simulated mode shapes of two edge states presented in Fig. 3.8(c) further confirms their localization feature.

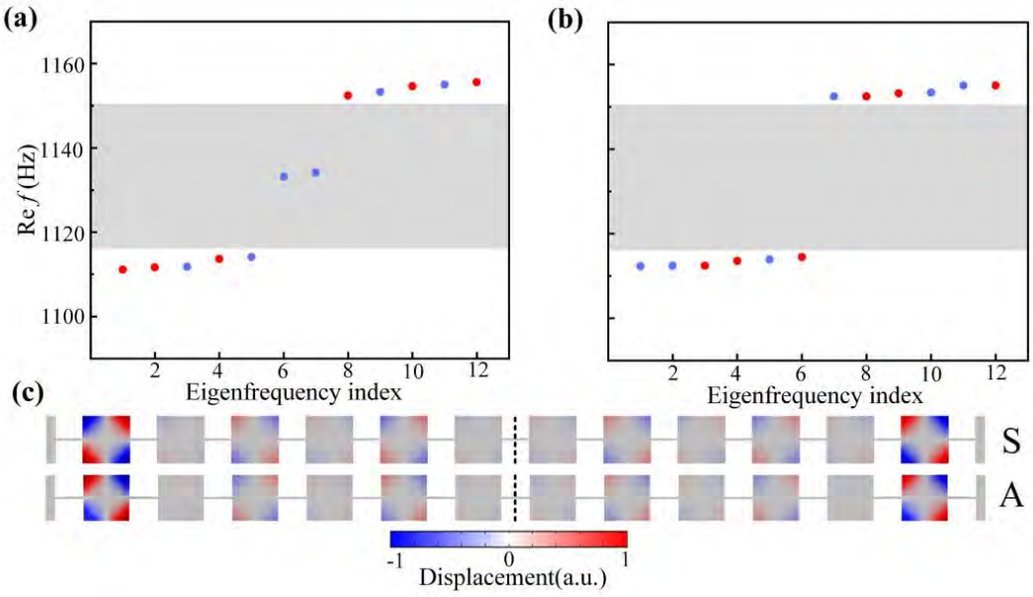

Figure 3.8 Topological edge states induced solely by non-Hermiticity. (a), (b) Simulated eigenfrequencies for finite-sized non-trivial and trivial 1D chains (3 unit cells), respectively. (c) Simulated out-of-plane displacement fields of the edge states at 1135 Hz. Two edge states are respectively mirror symmetric and asymmetric about the middle dotted line.

3.3.3 Robustness of the Non-Hermitian Topological Edge States

Like section 3.2.4, we also explore the robustness of the non-Hermitian edge states against random defects on the resonance frequencies and the coupling strengths. The resultant eigenfrequencies with the increasing of δ_κ and δ_w are illustrated in Fig. 3.9, demonstrating the robustness of the non-Hermitian edge states is similar to the previous Hermitian edge states.

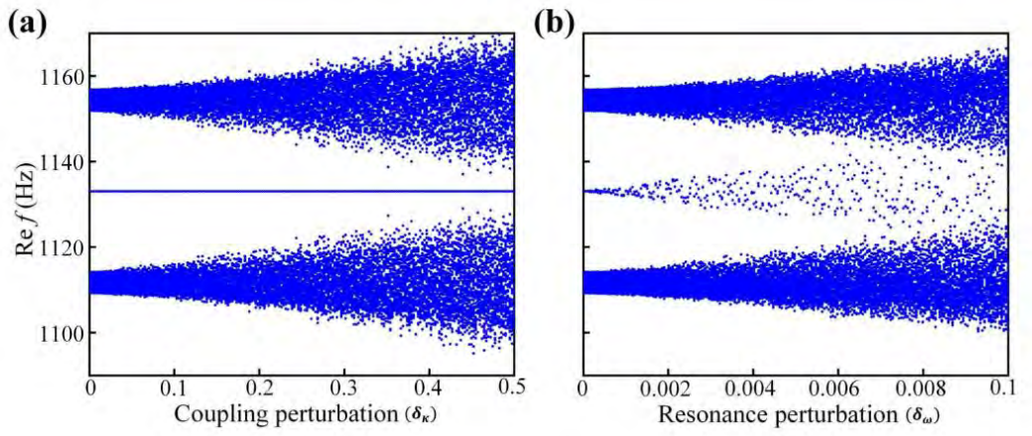

Figure 3.9 Robustness of the edge states. The eigenfrequencies at different strengths of (a) random coupling perturbations and (b) random resonance perturbations for the 1D finite-sized non-Hermitian chain.

3.3.4 Experimental Results of Single Plate with Intrinsic and Additional Damping

The resonant plates and connecting beams possess the same dimensions as the aforementioned Hermitian cases except that frame-shaped grooves with a depth of 2 mm [Figs. 3.10(a) and 3.10(b)] are added in the plates to attach AD layers (butyl rubber) in experiments. Since the out-of-plane displacement of the first non-rigid-body resonant mode is localized at the four corners of the plate, damping layers attached near the corners give rise to higher damping efficiency. Therefore, the grooves are located away from the plate's center. To determine the intrinsic material damping of a single plate, we measured the FRF curve of the plate with groove (L_1 = 41 mm, W_1 = 14.5 mm) but without AD layer [Fig. 3.10(a)] at first. The plate was suspended by thin strings to mimic free boundary conditions. As shown in Fig. 3.10(c), one resonance peak with a quality factor of 108 is located at 1082 Hz in the FRF curve. Then a piece of butyl rubber with matched size [black area in Fig. 3.10(b)] is inserted into the groove (L_2 = 46 mm, W_2 = 12 mm) of another resonant plate to

produce energy absorption. The resultant resonance frequency and quality factor are 1084 Hz and 13, respectively, shown in Fig. 3.10(d). Note that the widths of the grooves are uniform in simulations (W = 14.5 mm) but different (W_1 = 14.5 mm, W_2 = 12 mm) in the fabricated samples to minimize the frequency deviation introduced by the damping layers in experiments. The ID is represented by the imaginary part of the Young's modulus whose loss factor $\eta_1 = 0.009$ is achieved by fitting the simulated FRF curves to the experimental ones. The loss factor with AD is extracted and expressed in a similar way as $\eta_2 = 0.085$.

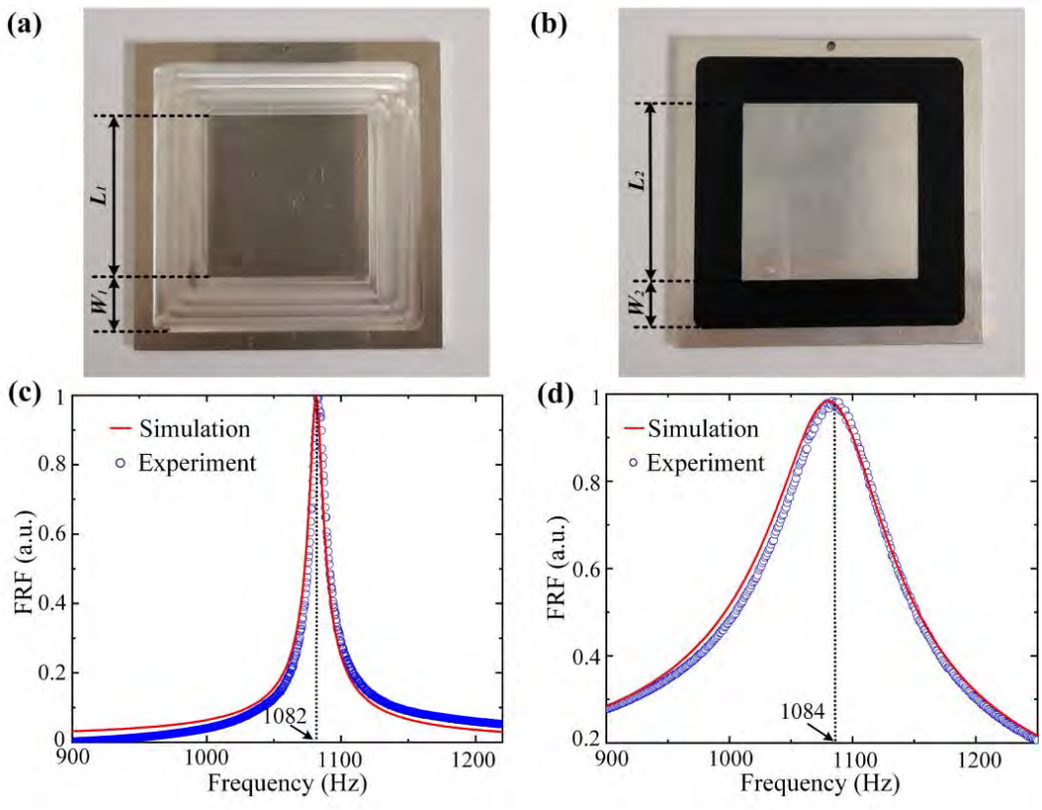

Figure 3.10 Forced responses of single plates with ID and AD. (a) Top view of experimental sample with only ID. L_1 = 41 mm, W_1 = 14.5 mm. (b) Top view of experimental sample with AD layer. L_2 = 46 mm, W_2 = 12 mm. (c), (d) FRF curves for the single plate correspond to (a) and (b), respectively. The blue circle curves represent the measured results, and the red solid curves are simulated results.

3.3.5 Experimental Results of the Non-Hermitian Chain

As single plates with distinct damping effects have been experimentally realized, we can further create different finite-sized non-Hermitian chains and explore their topological phenomena in experiments. Firstly, we fabricated two different elastic chains with 12 connected resonant plates. One chain possesses narrower grooves (W_2 = 12 mm) milled at the middle two plates within each unit cell while the other chain has the same grooves milled at the right two plates within each unit cell. Then, butyl rubbers are added in all the narrower grooves, giving rise to non-Hermitian topological non-trivial chain [Fig. 3.11(a)] and trivial chain [Fig. 3.11(b)]. To measure the bulk FRF curves, the shaker and laser are placed at the corners of fifth and ninth plate, respectively, as depicted in Fig. 3.11(a). When both shaker and laser are located at the outmost plate, edge FRF curves can be obtained. According to simulated results, band gaps should exist in both chains and edge states only appear in the non-trivial chain.

As displayed by the measured bulk FRF curves in Figs. 3.11(c) and 3.11(d), obvious drops are clearly visible, demonstrating the existence of the band gap in both cases. Compared to the bulk curves, the measured FRF spectra on edge plates exhibiting huge difference. Only one resonant peak [Fig. 3.11(e)] is observed in the band gap frequency range for the non-trivial case due to the in-gap topological edge states, while no obvious state emerges in the gap range in Fig. 3.11(f), since this band gap is trivial. These experimental results agree well with simulated ones, because the loss factors are well extracted in simulations to approach to realistic situations.

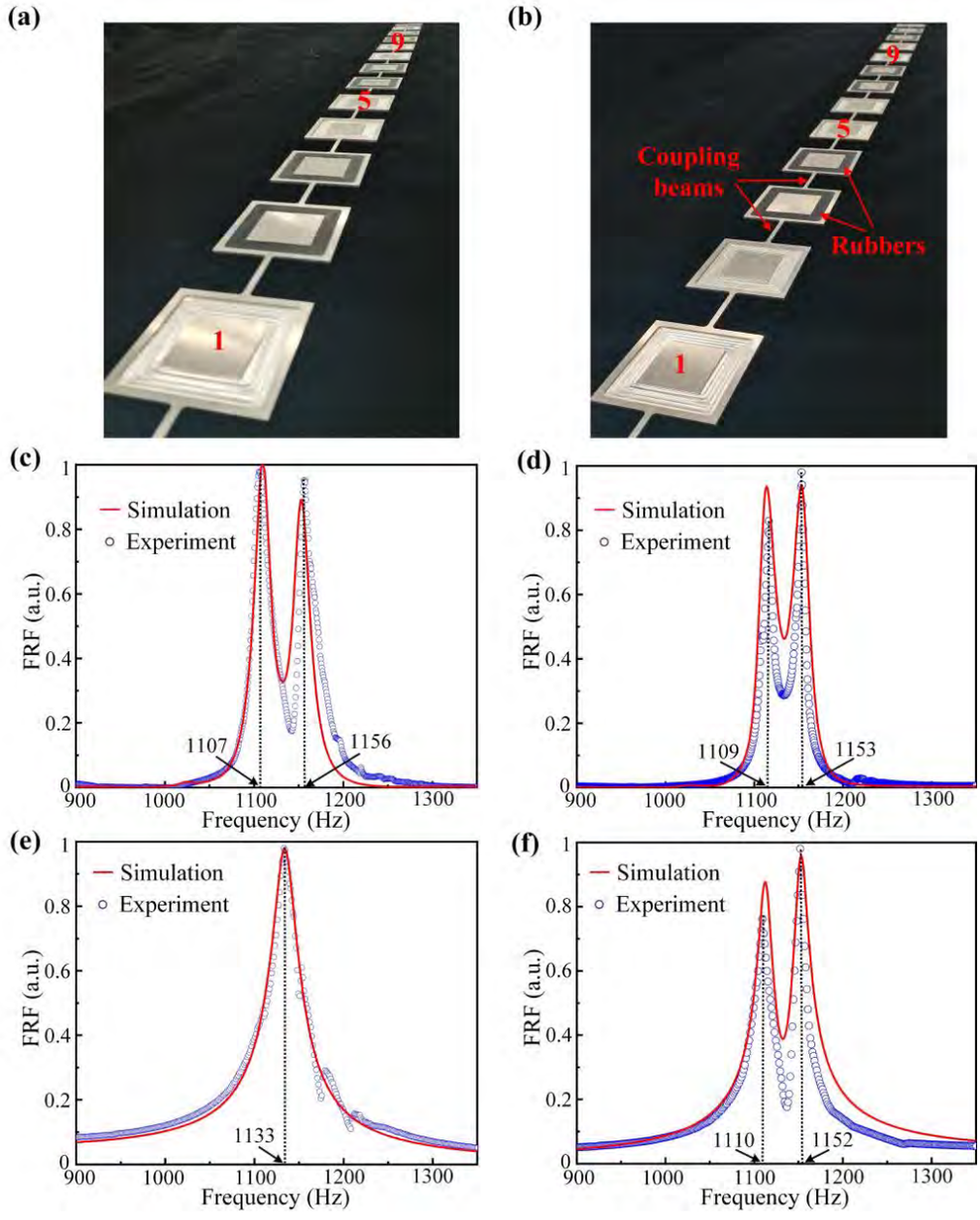

Figure 3.11 Forced responses of the finite non-Hermitian SSH chains. Photos of (a) non-trivial and (b) trivial elastic chain samples. (c), (d) Measured (blue circle) and simulated (red line) FRF bulk curves of the non-trivial 1D chain (c) and trivial 1D chain (d). (e), (f) Measured (blue circle) and simulated (red line) FRF edge curves of the non-trivial 1D chain (e) and trivial 1D chain (f).

3.4 Summary

In conclusion, two different topological edge states induced by different physics have been experimentally explored by using elastic counterparts of SSH chains: arrays of square plates connected by thin beams. We start with an ideal Hermitian case, whose non-trivial topology originate from different coupling strengths in a unit cell. The relative strengths of intra- and inter-cell couplings govern if the band diagram is topologically non-trivial or trivial. Then for the non-Hermitian case, coupling strengths are identical in the double-sized unit cell while AD is deliberately applied to certain square plates. The damping configuration is the decisive factor in creating topological non-trivial or trivial structure. As demonstrated by the experimental FRF measurements, edge states only exist in the non-trivial band gaps in both cases. The proposed perturbative metamaterials offer a good experimental platform for studying non-Hermitian topology in macroscopic scale as compared to electronic and photonic systems that are often in atomic scale and are difficult to be realized experimentally.

CHAPTER 4

Non-Hermiticity-Induced Topological Edge States in the Continuum in a One-dimensional Trimerized Elastic Lattice

4.1 Introduction

In Chapter 3, the topological properties are considered to exist in the band gaps which separate the spatially localized modes from the bulk continuous spectra of propagating waves. Yet, it is entirely possible that the localized topological states reside in bulk bands, behaving as the so-called bound states in the continuum (BICs) [140-143].

BICs refer to a class of spatially confined eigenstates residing inside the continuous spectra of propagating modes. Their appearance and unconventional properties in topological systems have recently gained much attention and inspired a variety of theoretical and experimental investigations, e.g., topologically protected bound states

against hybridization in electronic system [144], subspace-induced embedded topological interface states in coupled 1D acoustic chains [145], and in-band topological corner states known as higher-order topological BICs [146, 147]. Topological BICs generally emerge as a result of the eigenfrequency shift of either bulk bands [145] or localized topological states [148] due to specific spatial variations in the coupling terms. However, the relevant exploration remains in the context of Hermitian scenario. A recent theory [149] based on the TBM implies a possible direction to realize in-band topological states from PT symmetry with balanced gain and loss, but the experimental observation of these non-Hermiticity-induced, in-band topological states has not been reported to date.

In this chapter, rather than resorting to balanced gain and loss configurations that require complicated experimental setups, we develop a series of lossy and passive structures to experimentally observe the non-Hermiticity-induced, in-band topological edge states. The structures are 1D non-Hermitian trimerized chains which consist of resonant square plates and connecting beams. Dissimilar to the in-gap topological states that depend on alternating coupling strengths and Hermitian hypotheses, the in-band topological states in the chains only rely on the additionally added damping on particular plates. Since the AD is purposely applied to the middle site of the trimerized unit cell, two DPs respectively located at the BZ center and corner are gradually opened, leading to two band gaps. Rather than emerging in the

band gaps, the topological edge states keep fixed in the continuous spectrum, behaving as BICs. The robustness of these in-band edge states is still indicated by the nonzero general Zak phases based on the orthogonalized eigenstates. By implementing the necessary non-Hermitian parameters with constrained damping layer treatments, we experimentally observe such in-band topological edge states.

4.2 Band Diagrams and Topological Invariant of the Infinite-sized Chain

Here we focus on the non-Hermitian version of the trimerized lattices (lattice constant a = 187.5 mm) consisting of resonant square plates (with a hole in each center) weakly coupled by linking beams as depicted in Figs. 4.1(a) and 4.1(b). The lattices are cut from an aluminum alloy plate with a thickness of 1.46 mm, and the sizes of the plates and beams are 40 mm × 40 mm and 22.5 mm × 1.5 mm, respectively. Besides, the linking positions are identical (located at the middle of the plates), leading to the identical nearest-neighbor coupling strengths between two adjacent plates. Consequently, the band diagram for the trimerized unit cell in Fig. 4.1(a) is gapless, as presented in Fig. 4.1(c), and the degeneracies emerge at the center and edge of the first BZ. When AD treatment is introduced to the middle plate colored in blue in Fig. 4.1(b), both the degeneracies gradually split, giving rise to two complete band gaps, as shown in Fig. 4.1(d).

The band diagrams of the unit cells illustrated in Figs. 4.1(a) and 4.1(b) can also be obtained by solving the eigenvalue problems of the tight binding Hamiltonian matrices, which can be written as

$$H(k) = \begin{pmatrix} (1-d_0 i)f_0 & \kappa & \kappa e^{-ika} \\ \kappa & [1-(d_0+d_1)i]f_0 & \kappa \\ \kappa e^{ika} & \kappa & (1-d_0 i)f_0 \end{pmatrix} + \delta f \begin{pmatrix} 1 & 0 & 0 \\ 0 & 1 & 0 \\ 0 & 0 & 1 \end{pmatrix} \quad (4.1)$$

where a = 187.5 mm is the lattice constant, f_0 = 2640 Hz is the resonance frequency of the single plate, and $\kappa = 16$ Hz is the nearest-neighbor coupling strength, d_0 = 0.0041 and d_1 = 0.02 describe the unavoidably intrinsic material damping and additionally introduced damping, respectively, $\delta f = 36$ Hz is the frequency deviation from f_0 to the zero-energy frequency of the band diagrams due to the introduction of coupling beams. The value of δf can be adjusted to zero when the thickness of linking beams is smaller than the resonance plates (see Fig. A3 in Appendix B). The numerically calculated band diagrams based on Eq. (4.1) [red dotted lines in Figs. 4.1(c) and 4.1(d)] match well with those obtained from numerical simulations with COMSOL Multiphysics software [blue solid lines in Figs. 4.1(c) and 4.1(d)], indicating that the tight binding Hamiltonian matrices possess satisfactory agreement with the numerical simulations.

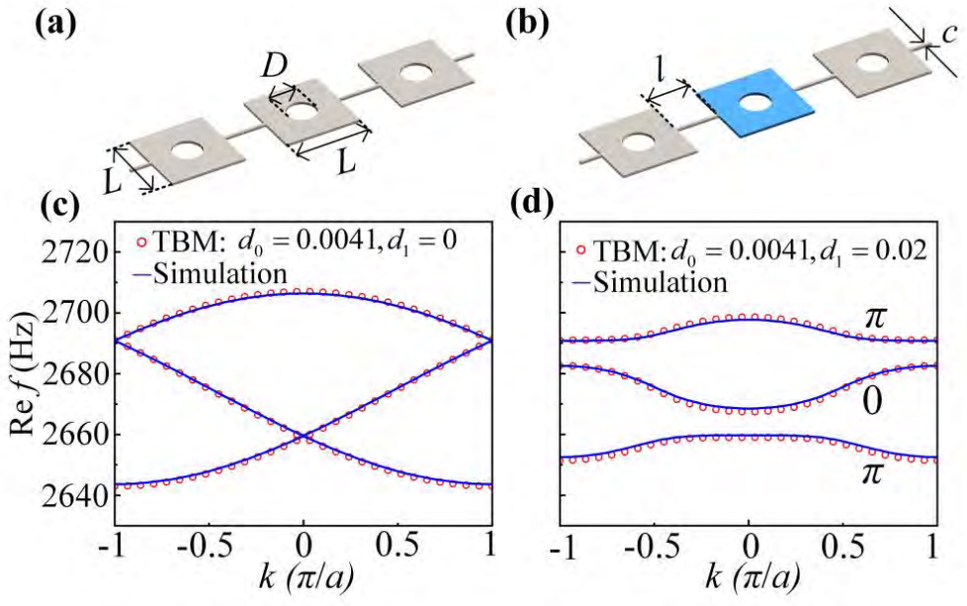

Figure 4.1 Band diagrams of the trimerized elastic lattices in the absence and in the presence of the non-Hermitian modulation. (a), (b) Schematic diagrams of the unit cells for the trimerized lattices with only intrinsic material damping and with AD treatment (applied to the middle plate colored in blue), respectively. L = 40 mm, D = 15 mm, l = 22.5 mm, c = 1.5 mm. (c), (d) Calculated band diagrams corresponding to the unit cells in (a) and (b), respectively. The general Zak phases for the three bands in (d) are calculated to be π, 0, π, respectively.

The topological properties of the non-Hermitian trimerized lattice can be identified by the general Zak phases of the energy bands [36, 150, 151], which take the form of

$$\theta_{mn}^{zak} = i\int_{-\pi/a}^{\pi/a} \langle \xi_{m,k}^{R} | \, \partial_k \, | \xi_{n,k}^{L} \rangle dk \tag{4.2}$$

where $\xi_{m,k}^{R}$ and $\xi_{n,k}^{L}$ are the biorthogonalized right and left eigenvectors of $H(k)$ that satisfy $\langle \xi_{n,k}^{L} | \xi_{m,k}^{R} \rangle = \delta_{mn}$. m, n = 1, 2, 3 represent the three energy bands and k is the corresponding wavenumber. The general Zak phases accumulated from $-\pi/a$ to π/a in the BZ are π, 0, π for the first, second and third band in Fig. 4.1(d), respectively, indicating the topologically non-trivial properties of the configuration in Fig. 4.1(b).

4.3 Topological Edge States in the Continuum of the Finite-sized Chain

4.3.1 Topological Edge States for a Lattice without Defects

To further probe the non-Hermiticity controlled topological properties, a finite-sized lattice with 5 non-trivial unit cells [Fig. 4.2(a)] is considered foremost. The simulated real parts of the complex eigenfrequencies for the chain are plotted in Fig. 4.2(b) (the calculated eigenfrequencies based on TBM see Fig. A4 in Appendix C). Two band gaps (gray shaded areas) are formed, which are consistent with the band diagram in Fig. 4.1(d). Furthermore, two topological edge states [red boxes in Figs. 4.2(b)] are clearly embedded into the middle 5 bulk modes other than the band gap ranges, which significantly differs from its Hermitian counterparts in this trimerized lattice (more details see Fig. 4.5). Although the edge states lie inside the continuous spectrum, their energy remains perfectly confined at two edges [Fig. 4.2(d)] with robustness against random coupling strength disorders.

Note that the middle 5 bulk modes between the two complete band gaps possess relatively higher imaginary parts around 40 Hz [Fig. 4.2(c)], implying a relatively higher elastic wave dissipation. In the according mode profiles, the elastic energy is mostly distributed on the 5 sites with AD that are highlighted in blue in Fig. 4.2(a).

As the elastic energy of the edge states is mainly trapped in the two plates with lower damping parameter [Fig. 4.2(d)], they possess relatively lower imaginary parts around 16 Hz shown in Fig. 4.2(c).

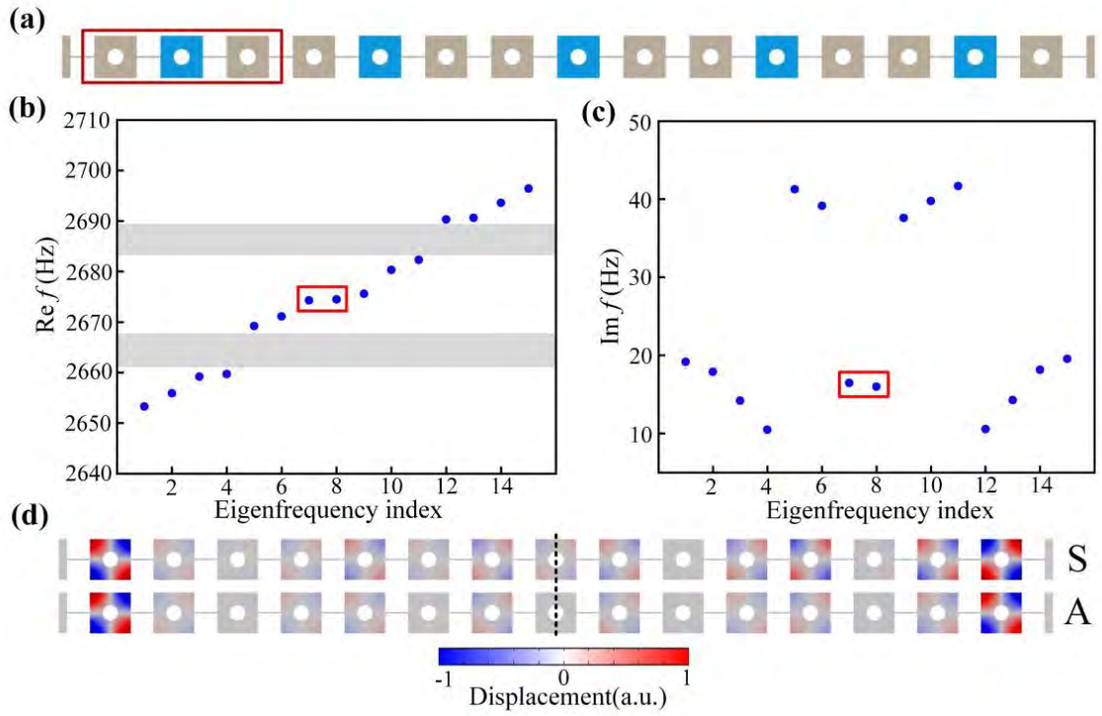

Figure 4.2 Topological edge states in the continuum for the chain system with 15 resonators. (a) The schematic of the chain composed of 5 unit cells. The red box indicates the trimerized non-trivial unit cell. Simulated real parts (b) and imaginary parts (c) of the complex eigenfrequencies for the non-trivial chain. (d) The out-of-plane displacement of the edge states at 2676 Hz. S (A) indicates the edge state profile is symmetric (anti-symmetric) about the dotted central line.

4.3.2 Eigenfrequencies of a Trimerized Lattice with Defects

Moreover, the existence of the edge states can be flexibly tuned by altering the boundary configurations. By way of illustration, for a chain composed of four nontrivial unit cells and one additional defect at each end [Fig. 4.3(a)], the edge

states disappear in the eigenfrequencies spectra, as observed in Figs. 4.3(b) and 4.3(c) [see Fig. A4 in Appendix C for the TBM results], which are fairly distinct from the spectra of the nontrivial lattice without any defect, Figs. 4.2(b) and 4.2(c). In this case, there are four middle bulk modes with relatively higher imaginary parts, as the chain has four additional damped sites highlighted in blue.

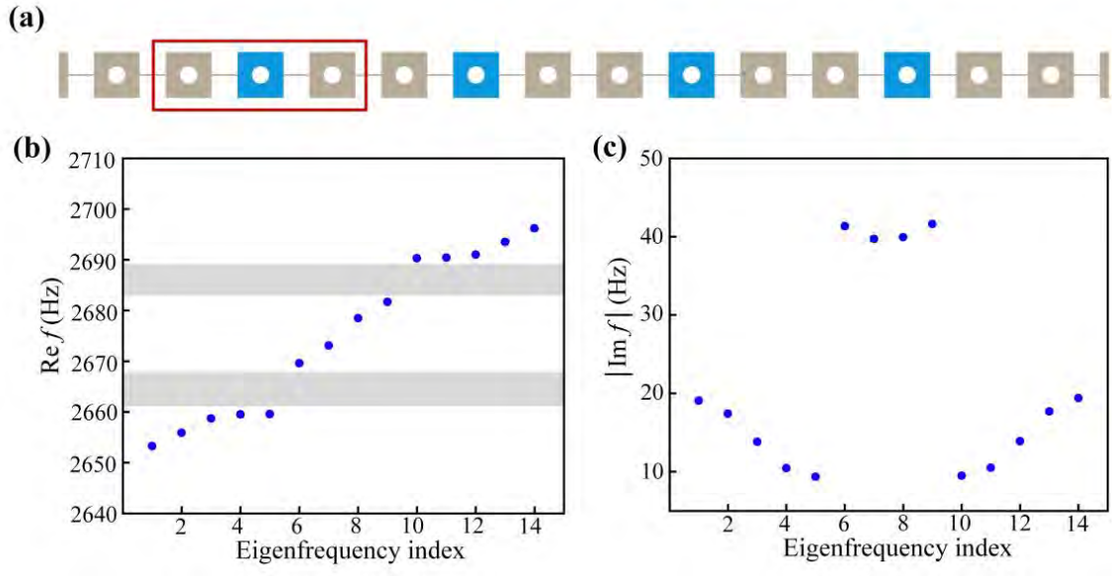

Figure 4.3 Eigenfrequencies of a trimerize lattice with one defect at each boundary. (a) The schematic of the chain with defects. Simulated real parts (b) and imaginary parts (c) of the complex eigenfrequencies for the chain.

4.3.3 Robustness of the Edge States in the Continuum

To evaluate the topological robustness of the edge states in the continuum, two kinds of random disorders are respectively introduced to the coupling (off-diagonal) terms and the resonance (diagonal) terms in the Hamiltonian matrices as they are two main nominal errors in manufacturing process. More specifically, we introduce a random perturbation on every off-diagonal and diagonal term with the strengths of

randomness denoted by δ_κ and δ_w, respectively. The resultant real part of eigenfrequencies for the long chain with 40 unit cells are plotted in Fig. 4.4(a) [Fig. 4.4(c)] with the increase of δ_κ (δ_w). In Fig. 4.4(a), the edge states marked by the red box are still trapped in the continuum and restricted at the central frequency of 2676 Hz despite the increase of δ_κ. Their eigenvectors [red curves in Fig. 4.4(b)] further demonstrate that the displacement fields are well confined in the first and the last sites of the chain. By contrast, all the eigenfrequencies in Fig. 4.4(c) gradually spread, and no obvious confinement of displacement fields can be observed in Fig. 4.4(d), implying the breakdown of robustness against randomness on the diagonal terms. Overall, the topological robustness of the non-Hermitian edge states in the continuum is similar to the robustness of the previous edge states in band gaps [34, 138].

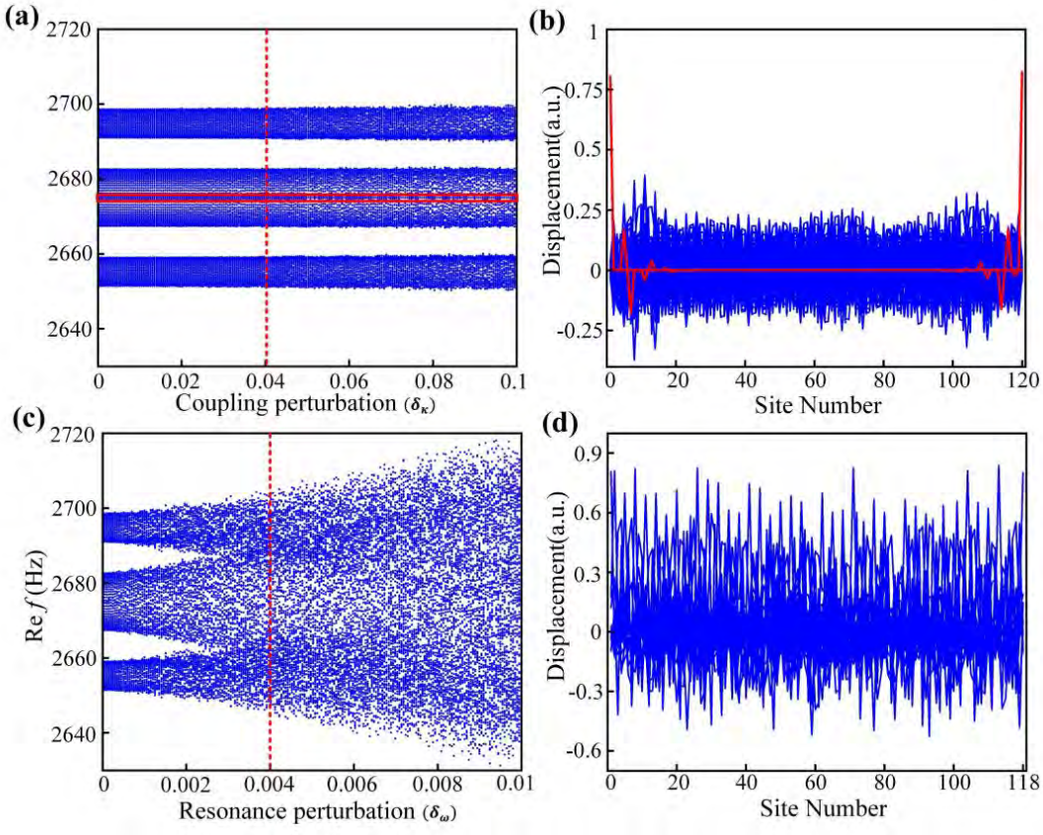

Figure 4.4 Topological robustness of the edge states in the continuum in a long chain with 40 unit cells. (a) The real part of eigenfrequencies with the increase of randomness on coupling disorders. Red box marks the edge states. (b) Displacement field profiles of the eigenstates at $\delta_\kappa = 0.04$ as marked by the vertical red dotted lines in (a). The red lines indicate two edge states. (c) The real parts of eigenfrequencies with the increase of randomness on resonance disorders. (d) Displacement field profiles of the eigenstates at $\delta_\omega = 0.04$ as marked by the red dotted lines in (c).

4.3.4 Hermitian Counterpart of the Trimerized Lattice

In Hermitian (lossless) systems (or the non-Hermiticity is irrelevant, e.g., a global loss uniformly distributed in the entire system), topological edge states can be realized by alternating coupling strengths. There is no exception for the trimerized lattice. For the two types of unit cells in Figs. 4.5(a) and 4.5(b), the nearest neighbor

coupling inside the unit cells is denoted by the intra-cell hopping γ, while the coupling between two nearest neighbor unit cells is inter-cell hopping λ. The coupling strength depends on the geometric parameters of the connecting beam, and here we just change the distance from the beam center to the horizontal nodal line to regulate the coupling strength. If all the beams are aligned ($\gamma = \lambda$), two Dirac cones will appear, similar to the band diagram in Fig. 4.1(c). As we change the linking positions to the extent that $\gamma < \lambda$ in Fig. 4.5(a), two band gaps appear [Fig. 4.5(c)] and the accumulated Zak phases are respectively π, 0, π from the top band down, which suggests this configuration is a non-trivial structure. On the other hand, for the $\gamma > \lambda$ configuration in Fig. 4.5(b), the accumulated Zak phases are all zero for the three bands in Fig. 4.5(d), corresponding to a trivial structure.

To observe the topological edge states, we further calculate the eigenfrequencies of a finite-sized chain composed of 5 trimerized non-trivial unit cells. It turns out that four topological edge states [marked by the red boxes in Fig. 4.5(e)] exist in the two band gap regions, rather than among the bulk modes, which further confirms that the in-band topological edge states presented in the main text are indeed caused solely by the non-Hermiticity. For the trivial chain, only bulk modes separated by two band gaps are observed [Fig. 4.5(f)]. The mode profiles of the edge states are given by Fig. 4.5(g), in which the upper (lower) two correspond to the two degenerate edge states in the upper (lower) band gap, and their out-of-plane displacement components are

mainly confined to the two edge sites asymmetrically (symmetrically) about the black dotted line.

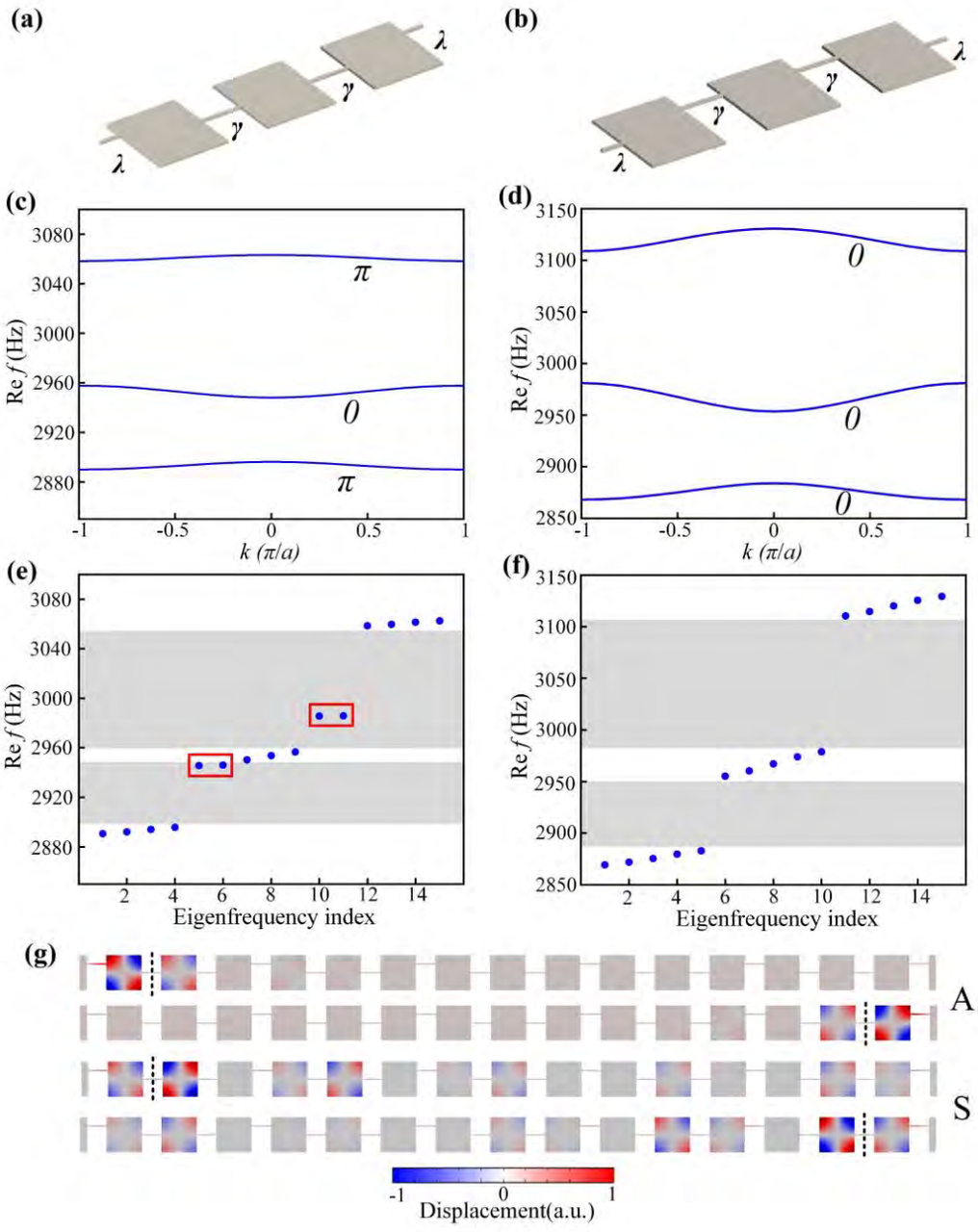

Figure 4.5 Topological edge states in finite-sized Hermitian chains. (a) The non-trivial trimerized unit cell. (b) The trivial trimerized unit cell. (c), (d) Simulated band diagrams corresponding to the unit cells in (a) and (b), respectively. (e), (f) Simulated eigenfrequencies for finite-sized chain composed of unit cells in (a) and (b), respectively. (g) The out-of-plane displacement of the edge states at 2986 Hz (the upper two state profiles) and 2945 Hz (the lower two state profiles).

4.4 Experimental Validation

4.4.1 Experimental Results for the Bare Plate and Composite Plate

In the experiments, the plates with AD treatments can be easily achieved by attaching constrained damping layer on the square plate to introduce energy dissipation, as depicted in Fig. 4.6(a). This composite plate is composed of three layers. From the top down, they are the constraint layer of reflective tin foil (silver layer), damping layer of butyl rubber (blue layer), and aluminum alloy plate (host plate with low intrinsic material damping), with the thicknesses of t_0 = 0.05 mm, t_1 = 1.00 mm, and t_2 = 1.46 mm, respectively. The ultrathin reflective tin foil can not only provide a highly reflective surface for receiving vibration signals by laser vibrometer but also increase the effective damping of the composite plate as the vibration energy is mainly attenuated by shear deformation [152].

To measure the FRF spectrum of the composite plate illustrated in Fig. 4.6(a), it was suspended by a string to mimic free boundary conditions. As depicted by the blue circle curve in Fig. 4.6(c), one resonance peak with certain bandwidth (the quality factor is 27) can be clearly observed at 2639 Hz. Without the constrained damping layer, the resonance peak of the bare plate will be shifted to a higher frequency of

2922 Hz with a sharper shape (see Fig. A5 in Appendix D). To experimentally make the plate without and with AD resonate at the same frequency, the bare plate was perforated with a circular through hole (the diameter is 15 mm) at the center [Fig. 4.6(b)]. As a result, the measured FRF spectrum, as given in Fig. 4.6(d), shows a narrower resonance peak (the quality factor is 112) around 2641 Hz. To obtain the effective damping parameter (denoted by imaginary part of Young's modulus) used in above numerical simulations from Fig. 4.1 to Fig. 4.3, the numerically calculated FRF spectra are fitted to the experimental data. It turns out that the Young's moduli are modeled with $E_1 = 68.9\ (1 + 0.04i)$ GPa and $E_2 = 68.9\ (1 + 0.007i)$ GPa for the plate with and without the constrained damping, respectively.

In addition, we also measured the mode shapes of these two plates at 2640 Hz and plotted them in the insets of Figs. 4.6(c) and 4.6(d), respectively (the data points measured for the interpolation are indicated by the black dots in the insets). It is proved that in spite of the constrained damping layer, the measured mode profiles still match well with the numerical results in Fig. 4.2(d).

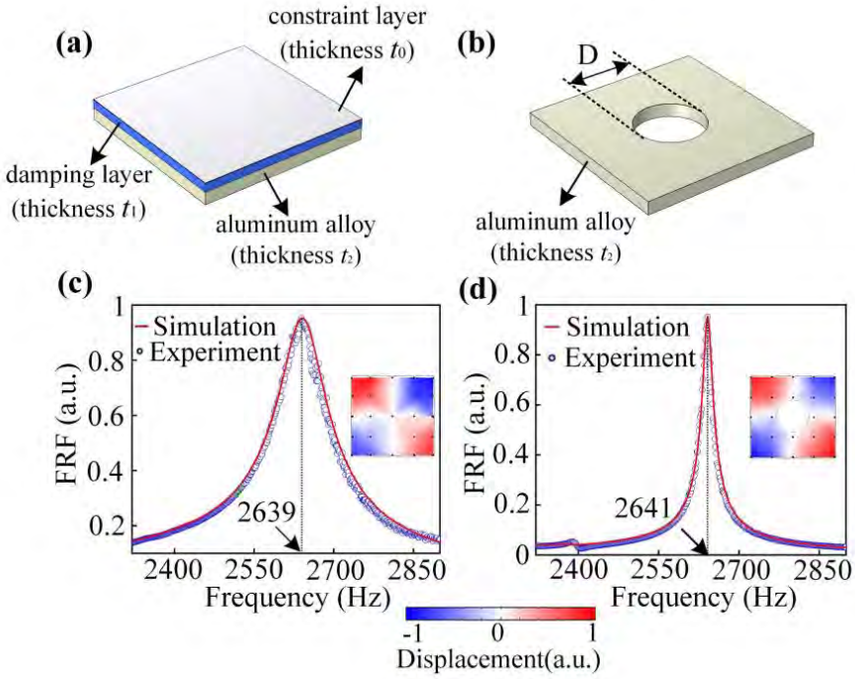

Figure 4.6 Forced responses of the plates with and without constrained damping layer. (a) Schematic of the composite plate with constrained damping layer. (b) Schematic of the aluminum alloy plate with a circular through hole. D = 15 mm. (c), (d) FRF spectra for the single plate illustrated in (a) and (b). The blue circles are the measured results, and the red solid lines present the simulated results.

4.4.2 Experimental Results for the Finite-sized Chains

As the single plates with different damping parameters have been satisfied, now we can move to explore the topological properties of 1D truncated lattice chains. One experimental sample is composed of 15 coupled plates without any defects [Fig. 4.7(a)], corresponding to the chain in Fig. 4.2(a). And the other sample possesses one additional defect at each boundary [14 coupled plates in Fig. 4.7(d)], corresponding to the chain in Fig. 4.3(a). In these two samples, the constrained damping layers are attached on the middle plates of all the trimerized non-trivial unit cells to supply the needed non-Hermiticities. Note that to keep the resonance frequency of the single plates pinned to 2640 Hz both in simulations and experiments, all the plates possess

the circular through holes in Figs. 4.2(a) and 4.3(a) but only the plates without constrained damping layers have the holes in Figs. 4.7(a) and 4.7(b).

During all the measurements, the shaker with a force transducer is placed at the corner of a bulk plate only with ID [marked as “4” in Figs. 4.7(a) and 4.7(d)] to input the excitation signal. For the sample in Fig. 4.7(a), the according response FRF curve of a bulk plate [marked as “7” in Fig. 4.7(a)] is measured, as denoted by the bule line in Fig. 4.7(b). Obviously, two dominant resonance peaks can be observed, corresponding to the upper and lower bulk states with lower imaginary parts [the first to forth and twelfth to fifteenth eigenfrequencies in Figs. 4.2(b) and 4.2(c)]. When it comes to the eighth plate with constrained damping layer, the measured FRF spectrum has three resonance peaks, in which the highest peak located in the middle bulk bands with higher imaginary parts [the fifth, sixth, nineth and eleventh eigenfrequencies Figs. 4.2(b) and 4.2(c)], as shown by the green curve in Fig. 4.7(c).

Strikingly different from two bulk spectra, the edge spectrum measured on the first plate in Fig. 4.7(a) only possesses one peak at the central frequency of 2676 Hz [the red line in Fig. 4.7(b)], exactly consistent with the simulated eigenfrequencies of edge states [the seventh and eighth eigenfrequencies Figs. 4.2(b) and 4.2(c)]. As we can see, the peaks of the edge spectrum and the bulk spectrum in green are overlapped at 2676 Hz in Fig. 4.7(b), indicating the topological edge states are embedded into the middle bulk states. For the other sample with two defects, no evident difference can be discovered between the response FRF spectra of an edge plate [the first plate in Fig. 4.7(d)] and a bulk plate only with ID [the seventh plate in Fig. 4.7(d)], as presented by the red line and blue line in Fig. 4.7(e), respectively. For

the green line in Fig. 4.7(f), which is the measured response of the nineth plate with AD in Fig. 4.7(d), the three separated peaks are consistent with that in Fig. 4.7(c). All the measured FRF spectra in Figs. 4.7(e) and 4.7(f) demonstrate that the topological edge states disappear with the introduced defects on the lattice boundaries.

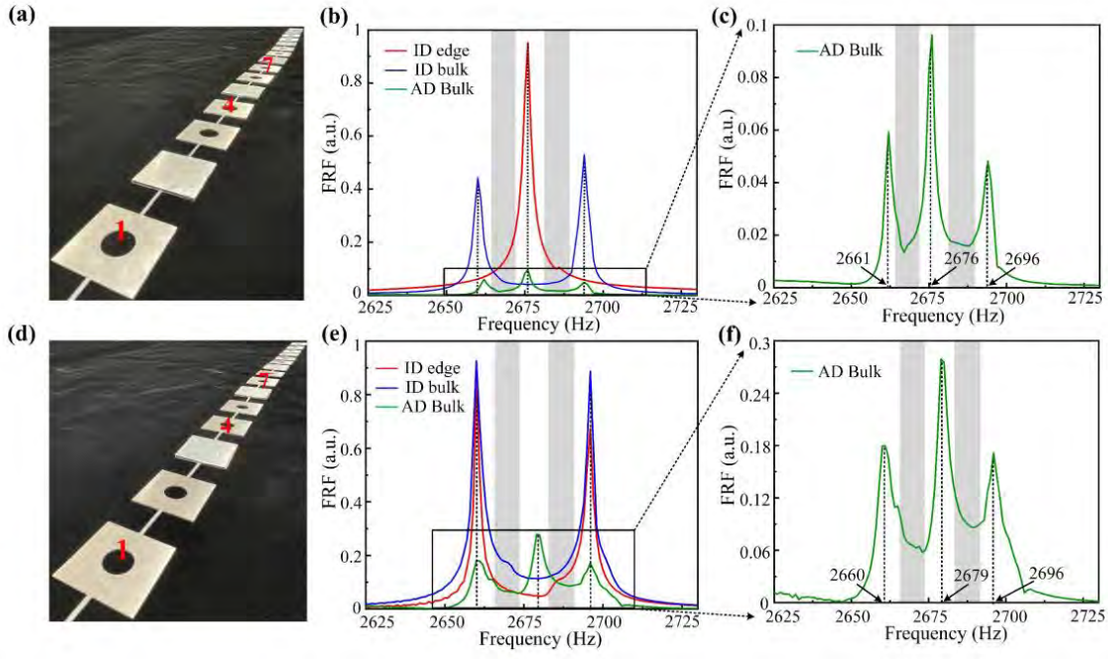

Figure 4.7 Forced responses of the 1D truncated lattice chains. (a) Photo of the sample without defects at boundaries. (b) Measured FRF spectra of the chain in (a). (c) Enlarged view of the green curve in (b). (d) Photo of the sample with defects at boundaries. (e) Measured FRF spectra of the chain in (d). (f) Enlarged view of the green curve in (e).

4.5 Summary

In conclusion, we have systematically elucidated the topological edge states in the continuum caused exclusively by non-Hermiticity in a trimerized elastic lattice. The characteristics of the edge states are numerically investigated and experimentally demonstrated in the finite-sized elastic lattices. Furthermore, two types of trimerized

chain systems with different topological features are respectively explored, which depend on the boundary conditions. The additional boundary defects can make the topological edge states in the non-Hermitian non-trivial chain disappear, providing a flexible approach to tune the existence of edge states. Our work offers an excellent platform towards the explorations on diverse non-Hermitian topological phenomena, such as higher-order non-Hermitian topological states in the continuum to enable high-density and disorder-immunity for wave routing. This idea can also be extended to various platforms in different dimensions, such as electric circuit, photonic and acoustic systems.

CHAPTER 5

Reconfigurable Higher-order Topological States in a Two-dimensional Acoustic Non-Hermitian Lattice

5.1 Introduction

In Chapters 3 and 4, the non-Hermiticity-induced in-gap and in-band topological edge states are all focused on the 1D chain structures, which hinders the explorations toward the non-Hermitian 1D topological waveguides and 0D topological higher-order corner states based on the 2D periodic lattices. More interestingly, it was demonstrated that when the non-Hermitian parameter goes across the EP, the topological interface states can propagate along arbitrary gain and loss domain walls in a 2D photonic lattice [126] . Moreover, non-Hermiticity shows the capabilities to flexibly control the higher-order topological states at domain walls with arbitrary shapes [153]. But, how to experimentally realize the reconfigurable higher-order topological states is not reported so far.

In this chapter, we experimentally investigate the flexible control of topological interface pathways and corner localizations based on an acoustic QTI with the help

of non-Hermiticity. The non-Hermitian modulation is realized by applying additional loss to a particular portion of the lattice [colored in blue in Figs. 5.1(a) and (b), termed as high-loss subarea (HLS)], while keeping the other sites intact [colored in red in Figs. 5.1(a) and (b), termed as low-loss subarea (LLS)]. Multiple new topological states emerge at the interfaces of the HLS and LLS as long as the loss contrast crosses the EPs, which gives rise to steering or localizing energy without changing the topological phase of the lattice. Hence, the non-Hermiticity can be regarded as a vital factor to manipulate the topological states on demand by constructing different patterns of the HLSs (Fig. 5.1), making the bulk sites, which always occupy a large section of the whole lattice, useful.

5.2 Theoretical Prediction Based on the Tight-Binding Model

5.2.1 Non-Hermiticity-Induced Newly Emerged Corner and Edge States

We start with the TBM for a QTI that has a topological nontrivial band gap, where the intracell coupling is smaller compared with the intercell coupling. The orange and black connecting lines in Figs. 5.1(a) and 5.1(b) represent the positive and negative couplings, respectively. In this typical QTI, the interior bulk sites are insulating, whereas the edge-transport pathways and corner-localizations are topologically protected. If we evenly introduce loss to the whole sites of this QTI, still no in-gap states occupy the bulk sites as the overall identical loss will not change

the topological properties of QTI [126]. However, if two different losses are applied to the red and blue sites in Figs. 5.1(a) and 5.1(b), respectively, new topologically protected corner [Figs. 5.1(c) and 5.1(d)] and edge states [Figs. 5.1(e) and 5.1(f)] will emerge at the interfaces between different loss areas. Both topological edge and corner states can be flexibly redistributed in various interfaces simply by changing the HLS shape.

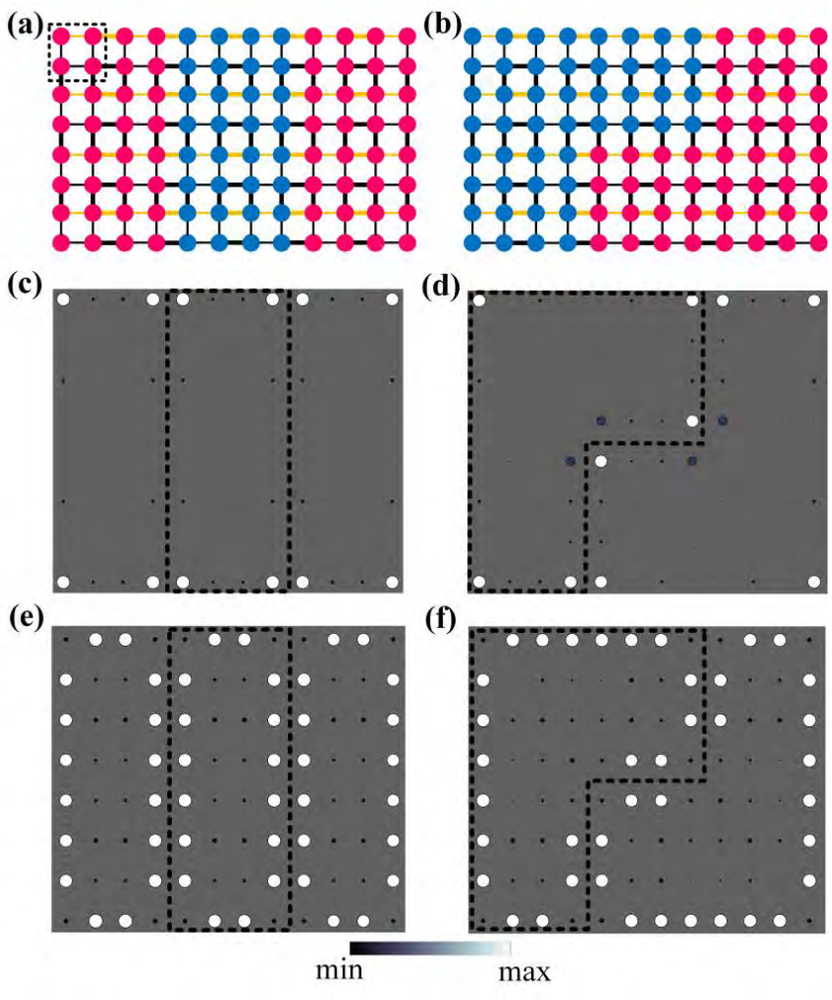

Figure 5.1 Non-Hermitian modulation of the topological states in a QTI. (a), (b) Schematics of the QTI with the imbalanced loss distributions. The dotted black box delineated one unit cell. (c), (d) The topological corner mode shape for the TBMs in (a) and (b), respectively. (e), (f) The topological edge state shape for the TBMs in (a) and (b), respectively. In (c)-(f), the areas inside the dotted black boxes possess additional losses. Both the size and the color of the dots in (c)-(f) represent the intensity.

5.2.2 Eigenvalue Evolution

The uneven energy dissipation along the interfaces breaks the insulating property of interior, creating new interior topological states. The loss contrast defined by $\Delta\gamma = \gamma_2 - \gamma_1$ (γ_1 and γ_2 are the loss coefficients in the LLS and HLS, respectively) is the decisive parameter, which is confirmed by the results given by TBM, as illustrated in Fig. 5.2. When $\Delta\gamma = 0$, the finite-sized lattice is a standard QTI with corner states located at the zero-energy, and gapped edge and bulk states distributed symmetrically about the zero-energy. With the increase of the loss contrast, more corner (red circles in Fig. 5.2) and edge (blue circles in Fig. 5.2) states come out from the original edge and/or bulk regions. For the lattice configuration in Fig. 5.1(a), new corner states evolve from the two branches of edge states [Fig. 5.2(a)] and coalesce to an exceptional point (see more details in section 5.2.3) at $\Delta\gamma / \kappa_1 = 2$. At the same time, the new edge states, coming from the gapped bulk regions, gradually merge into the existing edge states as the loss contrast grows.

In addition, the loss-induced new corner states can reside not only at the edges but also in the bulk sites [see Fig. 5.1(d)] via reshaping the loss configuration to the one presented in Fig. 5.1(b). In this case, two pairs of new corner states coming from the edge and bulk states coalesce at $\Delta\gamma / \kappa_1 = 2$ and $\Delta\gamma / \kappa_1 = 2.8$, respectively, creating two EPs, as shown in Figs. 5.2(b) and 5.2(d). After exceeding the EPs, they share the same real part but different imaginary parts of eigenvalues. The states with lower imaginary parts mainly reside in the LLS, while those with higher imaginary parts locate in the HLS, which evidence that they decouple with each other.

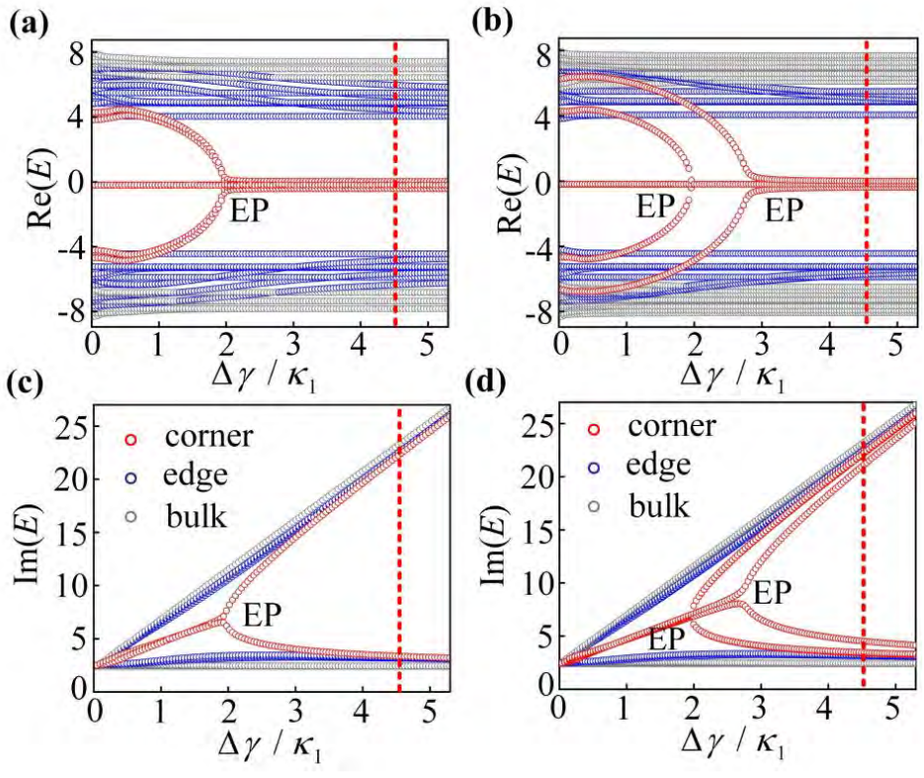

Figure 5.2 The evolution of the eigenvalue versus the loss contrast. (a), (b) Calculated real parts of the complex eigenvalues for the lattice illustrated in Fig. 5.1(a) and Fig. 5.1(b), respectively. (c), (d) Calculated imaginary parts of the complex eigenvalues for the lattice illustrated in Fig. 5.1(a) and Fig. 5.1(b), respectively. The red dashed lines denote the value used in the following measurements. In all calculations, the loss coefficient $\gamma_1 = 2.4$, the intracell coupling strength $\varepsilon_1 = 1$ and intercell coupling strength $\kappa_1 = 4.56$.

5.2.3 Exceptional Point

The EP, at which two or more eigenstates as well as their eigenvalues coalesce, is vital in our non-Hermitian models as it is the transition point to induce topologically protected new corner modes. Here, we utilize the 72-site TBM with the configuration shown in Fig. 5.3(a) as an example to investigate the EP. We use $n \in [1, 72]$ to mark the position of every cavity, therefore, the expected locations of the eight newly formed corner states [similar to Fig. 5.1(c)] are $n \in \{4, 5, 8, 9, 64, 65, 68, 69\}$.

Here, we chose a larger hopping ratio, i.e., $\kappa_1/\varepsilon_1 = 12.8$ ($\kappa_1 = 4.56$, $\varepsilon_1 = 0.36$) and plot the eigenfrequency evolution with the increased loss contrast of the lattice in Fig. 5.3(b). Before the EP ($\Delta\gamma/\kappa_1 = 1.4$), both the sites in the LLSs and HLSs possess higher field intensities, revealing that the coupling effect takes the dominant position [Fig. 5.3(c)]. At the EP ($\Delta\gamma/\kappa_1 = 2$), the two branches of corner modes coalesce into one [Fig. 5.3(d)]. After the EP ($\Delta\gamma/\kappa_1 = 4.5$), the corner states are decoupled, with one branch of corner states experiencing low-loss and the other branch undergoing high-loss, which are localized at the turning corners of the LLS [$n \in \{4, 9, 64, 69\}$, right panel of Fig. 5.3(e)] and HLS [$n \in \{5, 8, 65, 68\}$, left panel of Fig. 5.3(e)], respectively.

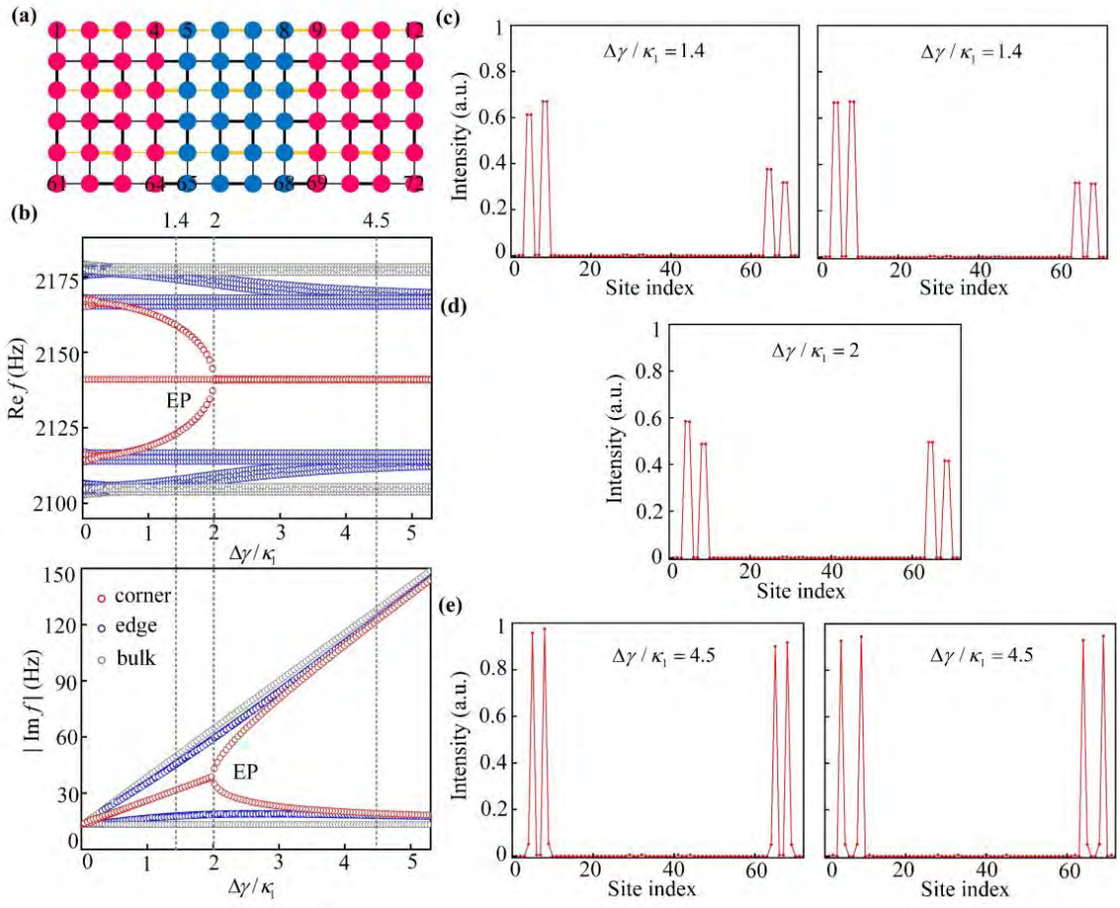

Figure 5.3 Probing the existence of the EP by checking the corresponding eigenstates. (a) Schematics of the 72-site TBM. (b) The eigenfrequency evolution as a function of increased loss contrast, showing the bifurcation characteristic of the corner states. (c)-(e) The eigenstates of corner states, which are induced by imbalanced loss, before (c), at (d) and after (e) the EP, corresponding to the three gray dotted lines in (b). The intensity distributions in the 72-site lattice before, at and after the EP show the coupling, coalescence and decoupling effect between the high-loss and low-loss corner states, respectively.

5.2.4 Robustness of the Corner States

The new corner states located at the imbalanced interfaces are also robust to certain kinds of defects as long as they cross the EPs. As an illustration, we use the configuration in Fig. 5.1(a) with $\Delta\gamma / \kappa_1 = 4.5$ to investigate the robustness against three different types of random defects on the coupling terms (δ_κ), on-site losses (δ_γ), and on-site potentials (δ_f), which are three typical perturbations. Specifically, some random numbers, defined as $\kappa' = X\delta_k E_{\text{gap}}$, $\gamma' = X\delta_\gamma E_{\text{gap}}$ and $f' = X\delta_f E_{\text{gap}}$ are added to the coupling terms, on-site loss terms and resonant frequency terms in the TBM, respectively. Wherein $X \in [-1,1]$ is randomly selected, δ_κ, δ_γ and δ_f denote the strengths of ddefects with respect to E_{gap} (the complete band gap), respectively. With the increase of δ_κ and δ_γ, the corner states remain to localize around the zero-energy with only negligible changes in the eigenfrequency, indicating their robustness against coupling and loss defectss, as depicted in Figs. 5.4(a) and 5.4(b). On the other hand, for the on-site potential disorder, the real parts of the eigenvalues of corner states are no longer degenerate as δ_f increased [Fig. 5.4(c)], due to the broken chiral symmetry [138].

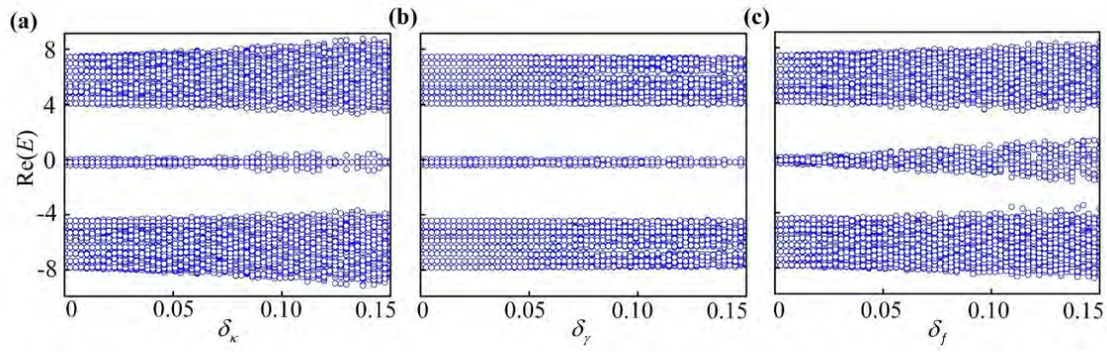

Figure 5.4 Robustness of the newly emerged corner states. The real parts of eigenvalue evolution with increased (a) coupling defect, (b) loss defect and (c) on-site potential defect.

5.3 Experimental Results

5.3.1 Acoustic Quadrupole Topological Insulator

We utilize coupled resonant cavities to realize the above TBMs [31-34, 154] in acoustic lattice. Each unit cell in the designed acoustic QTI includes four cuboid acoustic cavities connected via thin waveguides [the inset in Fig. 5.5]. The length, width and height of the cavities are 80 mm, 40 mm and 10 mm, respectively. The thin waveguides have the same length of 40 mm, while the cross-sectional areas are $2.5\times2.5\ \text{mm}^2$ for the intracell ones and $5\times5\ \text{mm}^2$ for the intercell ones. The cavities colored in blue (red) denote the high-loss (low-loss) area. The waveguides colored in orange (gray) represent positive (negative) coupling. Its quantized bulk quadrupole moment can be described by the quantized edge polarization $p_x^{v_y^{+(-)}} = p_y^{v_x^{+(-)}} = 0.5$ (see more details in Appendix E), following the nested-Wilson-loop approach [74]. The sign of coupling can be well tuned by changing the location of the connecting

waveguides, without influencing the coupling amplitudes [31]. The intracell and intercell coupling strengths are $\varepsilon_1 = -5.5$ Hz , $\kappa_1 = -25.6$ Hz , respectively (details see Appendix E).

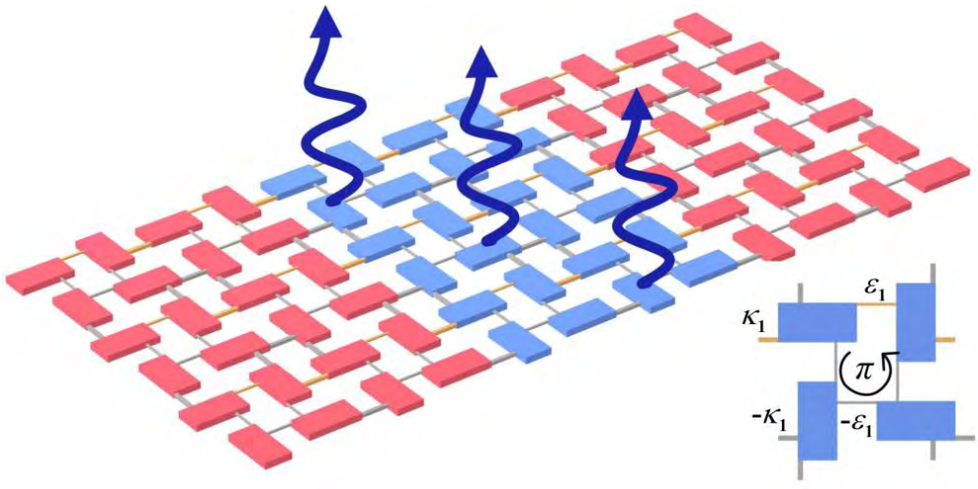

Figure 5.5 Schematic of an acoustic lattice which stringently satisfies the TBM in Fig. 5.1(a). The inset shows a unit cell of the lattice.

5.3.2 Measured Response Spectra for the Single Cavities

The loss coefficients of the cavity with only intrinsic loss (γ_1) and with additional loss (γ_2) can be extracted by fitting the simulated response spectra to the measured ones. By perforating the cavity with small leaky holes (the radius is 1.2 mm) and then inserting sound absorptive materials [19, 20], the additional loss $\Delta\gamma = \gamma_2 - \gamma_1$ is introduced. As illustrated by the blue circles in Fig. 5.6(a) [Fig. 5.6(b)], the measured spectrum of a single cavity with γ_1 (γ_2) has a peak at 2141 Hz with the quality factor of 80 (8). In simulations, we can treat the losses as the imaginary parts of sound speed, that is, $c_1 = 343\times(1+0.0062i)$ m/s for the cavity with γ_1 and $c_2 = 343\times(1+0.06i)$ m/s for the cavity with γ_2. Therefore, the loss coefficients, which are also the imaginary parts of the resonant frequency, are

$\gamma_1 = 2141 \times 0.0062 = 13.3$ Hz and $\gamma_2 = 2141 \times 0.06 = 128.5$ Hz, respectively. Here, $\Delta\gamma / \kappa_1 = 4.5$, denoted by the red dashed line in Fig. 5.2, is sufficient enough to exceed the EPs and separate the corner, edge and bulk modes.

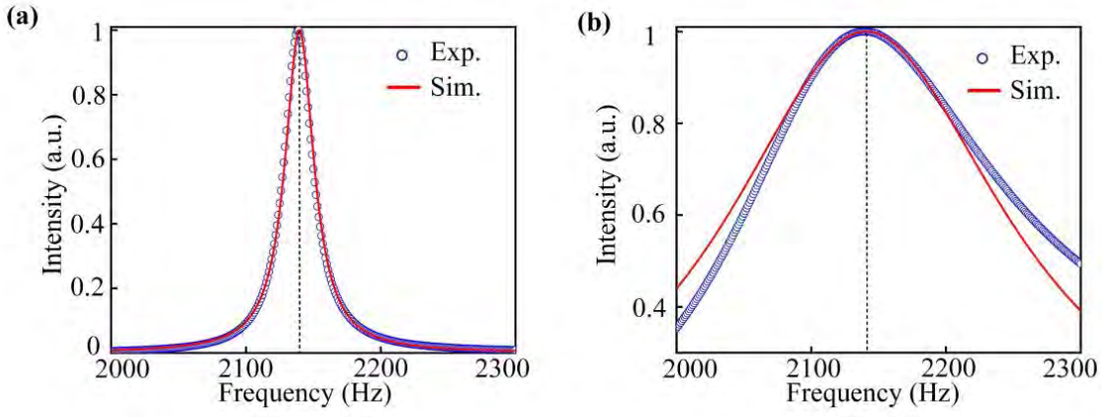

Figure 5.6 Measured and simulated response spectra for the single cavities. Response spectrum for a single cavity with loss coefficient of γ_1 (a) and γ_2 (b). The blue circles are the measured results, and the red solid lines denote the fitted simulated results.

5.3.3 Measured Profiles of a Lattice with Rectangular High Loss Subarea

A rectangular acoustic sample consists of coupled six-by-twelve cavities [Fig. 5.7(a)]. It is fabricated by stereo-lithography 3D printing technique to experimentally explore new topological corner and edge states, as predicted by the above theoretical calculations. The middle region of the sample (containing six-by-four cuboid cavities) is applied with additional loss, which corresponds to the TBM in Fig. 5.1(a). Small pieces of sound-absorbing sponge (black) are added into the leaky holes of these cavities to minimize the frequency deviation induced by the additional loss. Two identical holes are also drilled on the upper and lower sides (the radius is 1 mm) of each cavity to launch and measure the sound signals. When not used, the holes are

sealed by the matched cover lids [round protrusions in Fig. 5.7(a)].

In the measurement, the exciting loudspeaker and measuring microphone are inserted at the same cavity, and this process is repeated for all the cavities. The non-Hermiticity-controlled new topological states located in the LLS dominate that in the HLS as they show almost the same quality factors when compared with the original topological states (around 71), but for the topological states in the HLS, the quality factors are extremely small (around 9). Hence, the measured acoustic intensity spectra for cavities in the LLS that we focused on are enough high in amplitude to characterize the topological sates and band gap, while the intensity spectra for cavities in the HLS are much lower.

Firstly, a bulk cavity labelled “3” in Fig. 5.7(a) is excited and measured to study the band gap feature. Its response spectrum [the gray area in Fig. 5.7(b)] shows two peaks, which correspond to the two branches of bulk states with lower imaginary parts around 14 Hz [see Fig. A7(a) in Appendix F]. Then, we measure a bulk cavity resided in the middle of the interface [marked as “2” in Fig. 5.7(a)], where the newly formed edge states are expected to be detected. The two peaks in the measured spectrum [the blue one in Fig. 5.7(b)] possess a smaller interval, evidencing the prediction in Fig. 5.2. In contrast, for the spectrum measured in the lowermost cavity of the interface [labelled as “1” in Fig. 5.7(a)], only one peak at the mid-gap frequency of 2141 Hz can be observed [depicted by the red plot in Fig. 5.7(b)], manifesting the existence of the new corner states.

By repeating the measurements to all the sites, the site-resolved intensity field

distributions at peak frequencies of the three spectra [indicated by the black dotted lines in Fig. 5.7(b)] can be obtained and plotted in Figs. 5.7(c)-5.7(e), respectively. The intensity profile at 2141 Hz in Fig. 5.7(c) verifies the eight corner localizations. In addition to the original four corners, four new energy concentrations emerge at the interface corners. Moreover, the edge states profile [Fig. 5.7(d)] manifests that the overall intensity along the edges and interfaces is relatively higher than that in the interior, different from the bulk states profile [Fig. 5.7(e)].

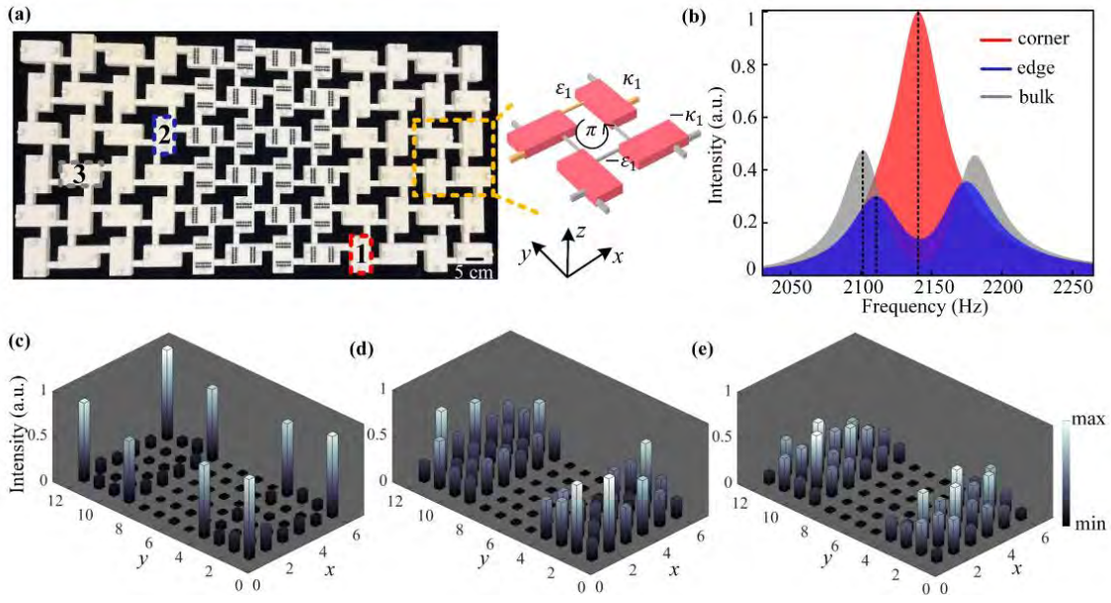

Figure 5.7 Measured acoustic responses of the lattice with a rectangular HLS. (a) Photo of a sample with six-by-twelve site cavities. The inset illustrates one unit cell of the lattice. (b) Response spectra measured at cavities “1”, “2” and “3” marked in (a), corresponding to the edge-evolved corner (in red), bulk-evolved edge (in blue) and bulk (in gray) modes, respectively. (c)-(e) Measured intensity distributions at 2141 Hz, 2114 Hz and 2100 Hz, correspond to the peaks of the new corner, new edge, and bulk spectra, respectively.

5.3.4 Measured Profiles of a Lattice with L-shaped High Loss Subarea

Non-Hermiticity improves the topological edge transport and corner localization by using various patterns inside the lattice. To show such flexible reconfigurability, the rectangular pattern of the HLS is shifted to an “L” shape [Figs. 5.1(b) and 5.8(a)]. Surprisingly, in the measured spectrum of an interior bulk cavity [site “1” in Fig. 5.8(a)], only one peak appears [red area in Fig. 5.8(b)], similar with the one in Fig. 5.7(b). These results demonstrate that the bulk-evolved corner states have almost the same characteristics as the edge-evolved ones if they exceed the corresponding EPs. The intensity spectrum measured in cavity “2” (or cavity “3”), which is resided in the other turning corner in the lattice, is represented by the green area in Fig. 5.8(b). In contrast, three separated peaks are observed, implying that a mid-gap corner state coexists with the gapped bulk states in these two cavities [see Fig. A7(d) in Appendix F]. The bulk and new edge spectra measured in cavity “5” and cavity “4” are represented by the gray and blue colors in Fig. 5.8(b), respectively, showing consistency with the measured ones in Fig. 5.7(b), which further evidence their stability no matter of the subarea patterns.

In a same way, we also measure the responses of the whole sample for the corner (2141 Hz), edge (2114 Hz) and bulk (2100 Hz) states, as indicated in Figs. 5.8(c)-5.8(e), respectively, which demonstrate the energy localizations at the predicted

corner and edge positions.

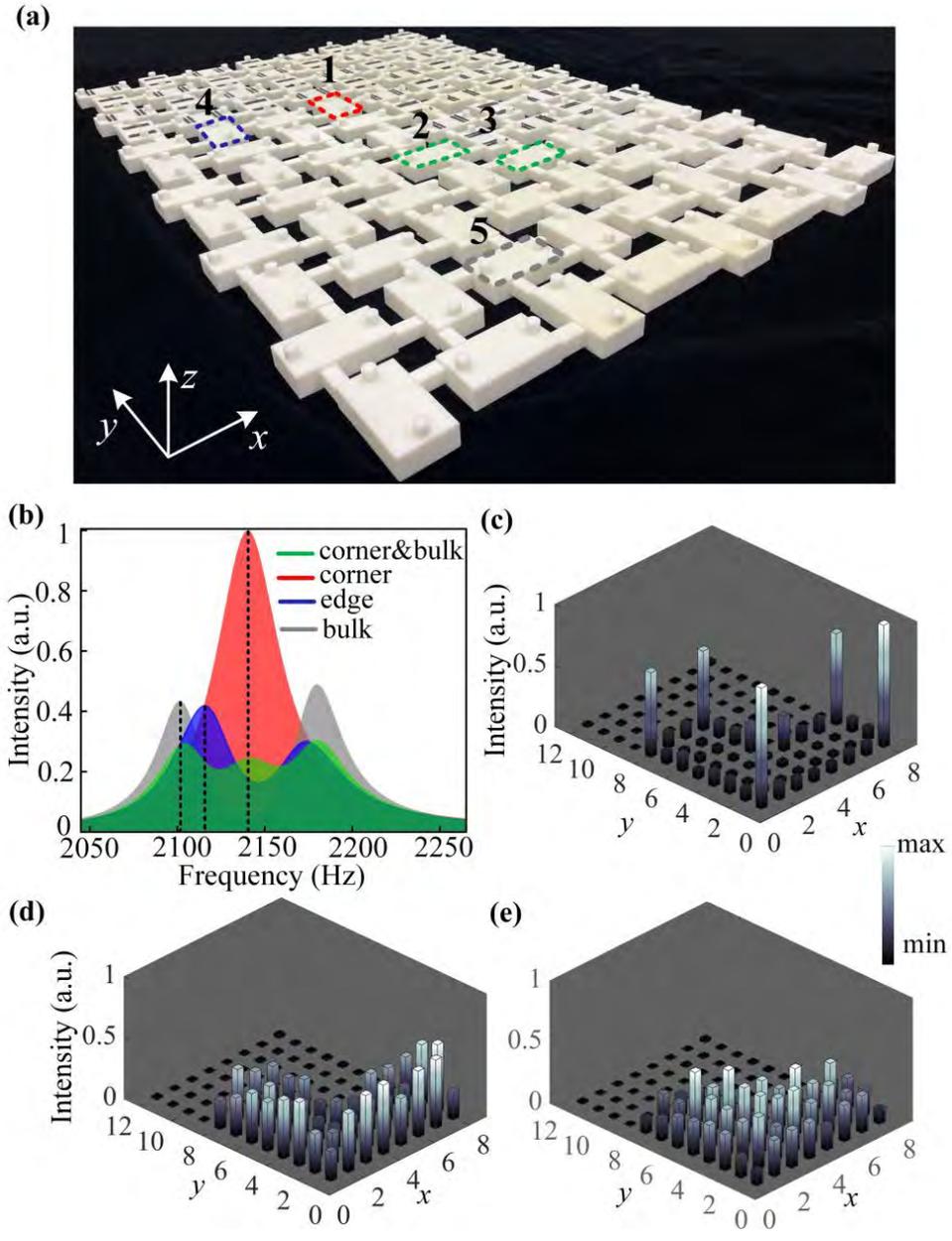

Figure 5.8 Measured acoustic responses of the lattice with an "L" shaped HLS. (a) Photo of the sample with eight-by-twelve site cavities. (b) Measured spectra in cavities "1", "4" and "5" labelled in (a), respectively, corresponding to the bulk-evolved corner (in red), bulk-evolved edge (in blue) and bulk (in gray) modes. The green spectrum is measured in cavity "2", which is occupied by a bulk-evolved corner mode and two bulk modes. (c)-(e) Measured acoustic intensity profiles at 2141 Hz, 2114 Hz and 2100 Hz.

5.4 Numerically Simulated Field Intensity Distribution

To compare with the measured results presented in Figs. 5.7 and 5.8, we perform the full-wave simulation for the acoustic lattices with a rectangular HLS and an “L” shaped HLS, respectively. For the former one, the response spectra in the same cavities, labelled as “1”, “2” and “3” in Fig. 5.7(a), are numerically calculated and denoted by the red, blue and gray spectra in Fig. 5.9(a), respectively. The separated peaks in the gray spectrum manifest two branches of bulk states, while the two closer peaks in the blue spectrum verify the newly formed edge states inside the bulk band gap. Since the red spectrum only has one peak located at 2141 Hz, the existence of edge-evolved corner states is confirmed. The field intensity distributions at the three peak frequencies, indicated by the three black dotted lines in Fig. 5.9(a), are also calculated and plotted in Fig. 5.9(b)-(d), which further evidence the edge-evolved corner, bulk-evolved edge and bulk states.

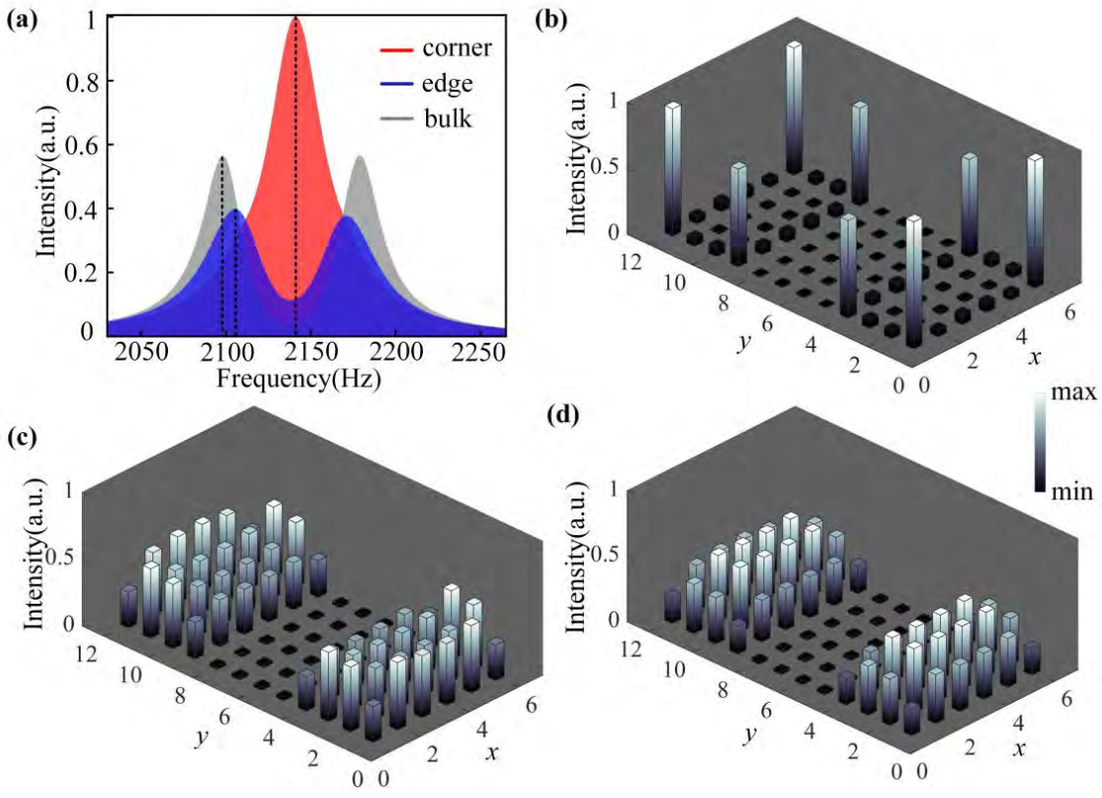

Figure 5.9 Full-wave simulation on the acoustic lattice with a rectangular HLS. (a) Simulated acoustic intensity spectra. Red, blue and gray spectra denote the edge-evolved corner, bulk-evolved edge, bulk spectra calculated at cavity "1", "2" and "3" in Fig. 5.7(a), respectively. (b)-(d) Simulated field intensity distributions at the peak frequencies of the corner, edge and bulk intensity spectra, corresponding to the three black dotted lines in (a), respectively.

For the latter lattice with an "L" shaped HLS, the simulated bulk spectrum, bulk-evolved edge spectrum and the bulk-evolved corner spectrum share the similar modal characteristics with the previous ones with a rectangular HLS, as confirmed by the gray, blue and red spectra in Fig. 5.10(a). However, at the other turning corner of imbalanced losses in the interior bulk, the single-site localization property of the new corner modes is shifted to the double-site localization due to the fact that these two sites [cavities "2" and "3" in Fig. 5.8(a)] are not only occupied by the new corner

state but also the gapped bulk states, which can be confirmed by the simulated response spectrum in the cavity “2” or “3” [green spectrum in Fig. 5.10(a)]. Similarly, the field intensity profiles at the three peak frequencies are also given in Fig. 5.10(b)-(d). In summary, all these simulated results are consistent with the experimental ones indicated in Figs. 5.7 and 5.8.

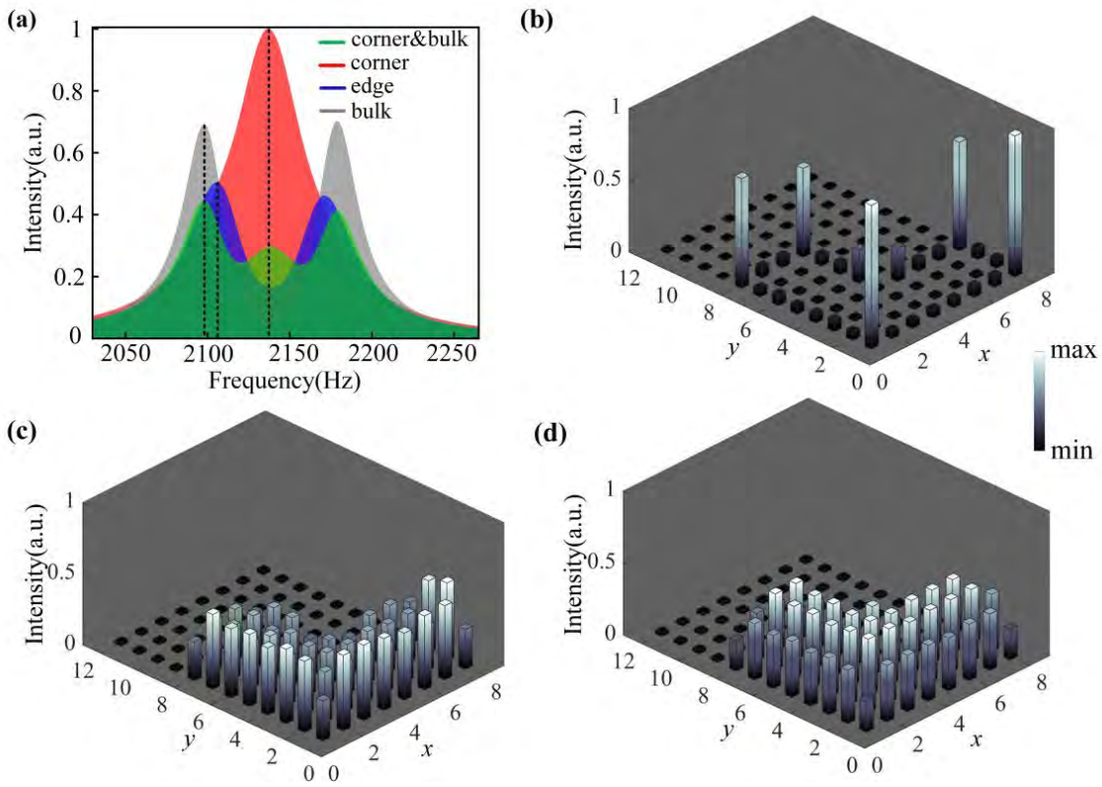

Figure 5.10 Full-wave simulation on the acoustic lattice with an “L” shaped HLS. (a) Simulated acoustic intensity. The simulated bulk-evolved corner, bulk-evolved edge, and bulk spectra are represented by the red, blue and gray areas, respectively. (b)-(d) Simulated field intensity profiles at the peak frequencies of the corner, edge and bulk intensity spectra, respectively.

5.5 Summary

In conclusion, we have proposed and experimentally evidenced a non-Hermitian scheme to create the topological interfaces, which are formed by setting imbalanced losses. The interfaces hold both first-order and second-order topological states and can be flexibly adjusted via setting different patterns of HLS. The newly emerged first-order edge states are evolved from the original bulk modes, whereas the new corner states can come both from the original edge and bulk statess depending on the shapes of HLS, which show different EPs as the overall coupling strength of a bulk site is larger than an edge site.

Our work shows that non-Hermiticity is an effective method by which the topological states can be flexibly controlled to guide and localize energy on demand, such that the originally useless bulk sites can be occupied by an edge or corner states leading to a significant improvement of the reconfigurability of the topological states. Other types of topological states, for example, the higher-order topological defect states in the honeycomb or hexagonal lattices [35, 113, 155, 156] and third-order topological states in the three-dimensional octupole topological insulators [33] can also be flexibly modulated.

CHAPTER 6

Topological Phenomena Arising from Fluid-solid Interactions in a Three-dimensional Phononic Crystal

6.1 Introduction

The investigation of topological phononic systems is generally limited to sound waves in either fluids or solids alone to simplify the physical picture, just like what we have done in Chapters 3, 4 and 5. As a mechanical wave [24], sound propagates in the manners of a pressure perturbation in fluids or an elastic stress perturbation in solids and is represented by a scalar wave or vector wave, respectively (recent study about acoustic spin have the potential to realize the counterpart of the QSHE in acoustic waves). This fundamental point leads to intrinsic differences in the dynamics and symmetries for sound in fluids and solids. However, such intrinsic differences and their possible interactions have yet to be considered in the development of topological phononics, even for the underwater environment where

the interactions can become considerable [26, 27].

In this chapter, we propose a novel approach to create and control topological properties in acoustic wave systems by utilizing the interplay of scalar sound in fluids and its vectorial counterpart in solids. With this approach absent in photonics and unique for phononics, we demonstrate type-II nodal rings in a simple 3D phononic crystal composed of identical perforated metallic plates immersed in water. Through near-field scanning of the fabricated sample, we experimentally confirm our findings and observe associated strongly tilted DSSs as well as nodal chains in the simple structure. Our study reveals that the sophisticated interaction between fluids and solids for sound, previously often disregarded for simplicity in topological phononics research, contains rich physics beyond sound wave systems supporting solely fluid-borne or solid-borne sound. It can thus serve as a novel platform for exploring unique topological physics and acoustic applications.

6.2 Nodal Rings Induced by Fluid-solid Interaction

6.2.1 Simulated Band Diagram of the Three-dimensional Unit Cell

We consider a 3D phononic crystal, comprised of identical aluminum plates, immersed in water [Fig. 6.1(a)]. Each plate is perforated with a square lattice of

circular through holes. Water, dissimilar to air, possess comparable acoustic impedance with aluminum, significantly improving fluid-solid interaction. The phononic crystal belongs to the space group P4/mmm (No. 123). In Fig. 6.1(a), the bottom right inset depicts the 3D first BZ and the red dashed box shows a basic unit cell (z direction not shown). The diameter of holes d_0 = 2 mm, the in-plane lattice constant a_0 = 3 mm, the distance between adjacent plates t_w = 2 mm, the thickness of plates t_m = 2 mm, leading to out-of-plane lattice constant $a_z = t_m + t_w$ = 4 mm.

The first four bands of the phononic crystal stem from the three lowest plate modes and one waterborne sound mode. The simulated band diagram [Fig. 6.1(b)] along the high-symmetry lines of the first BZ characterizes their emergence from zero frequency at Γ point. The first band degenerates with the second band on high-symmetry planes of the first BZ. Their intersecting points, as marked by the red, blue, and green dots in Fig. 6.1(b), form different nodal rings, respectively. Moreover, these intersecting points are all gapped slightly away from corresponding high-symmetry planes in the momentum space, which are the features of nodal rings (see Appendix G).

The detailed shapes of the nodal rings [Fig. 6.1(c)] in the whole first BZ further reveals that the blue and green nodal rings are chained together, forming nodal chains. The frequency variations of the nodal rings are plotted in Fig. 6.1(d). According to

the touching band slopes beside the nodal rings, the red and blue ones are type-II nodal rings, while the green ones are hybrid nodal rings [Fig. 6.1(e)]. The hybrid green nodal rings have a relatively large frequency dispersion ($\Delta\omega/\omega_{mid}$ ~ 12.3%, with $\Delta\omega$ being the frequency variation and ω_{mid} being the middle of frequencies), while the type-II red and blue nodal rings have smaller frequency dispersions ($\Delta\omega/\omega_{mid}$ ~ 6.6% and ~ 1.4% for the red and blue ones). Other nodal rings may also emerge between the second and higher-order bands, but they all reside in the sound cone (bulk acoustic waves in water) when projected along the *z* direction, which are out of our interest.

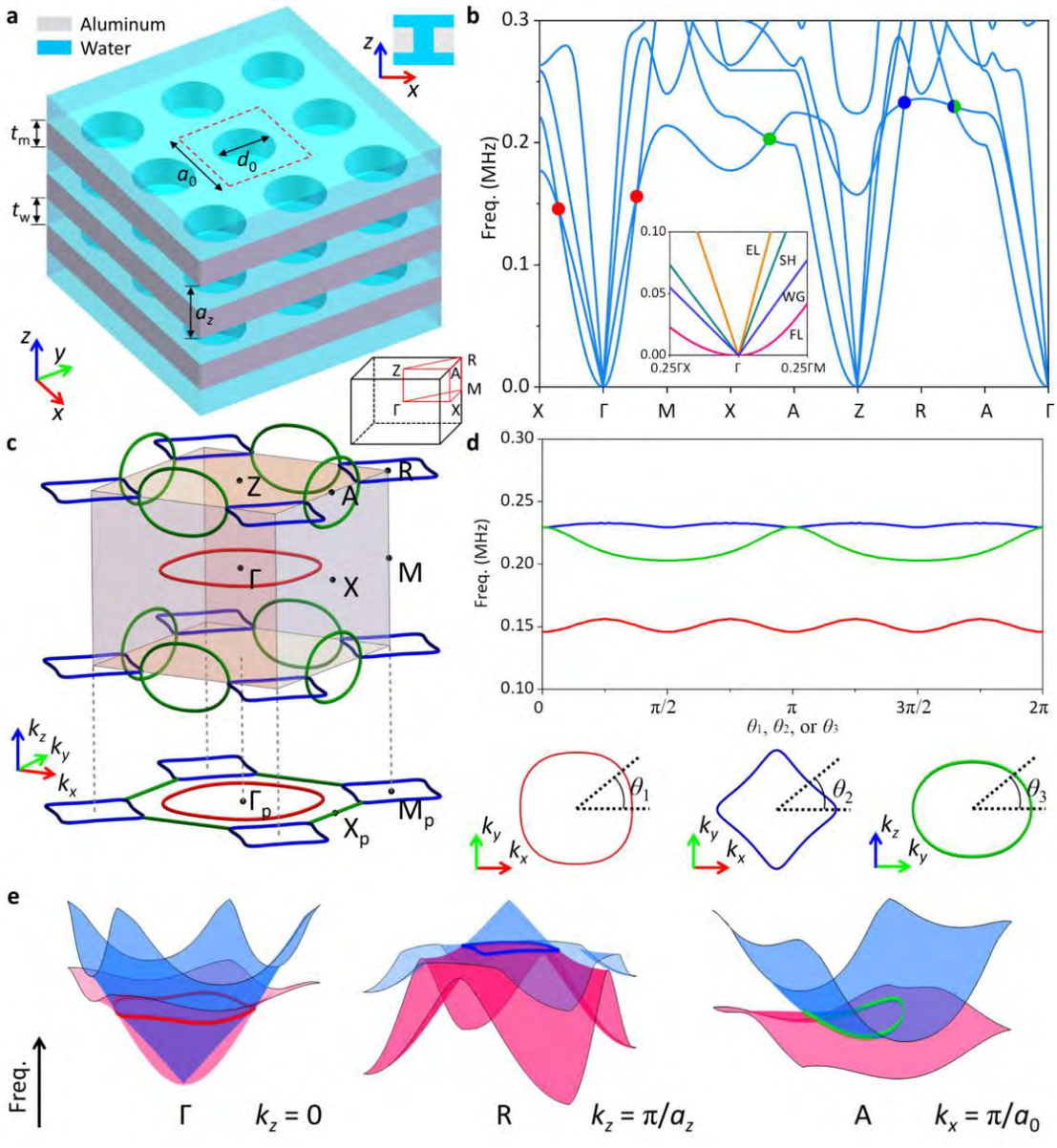

Figure 6.1 Type-II nodal rings induced by fluid-solid interaction. (a) Perspective and cross-sectional views of the 3D phononic crystal. (b) Simulated band diagram along high-symmetry lines in first BZ. (c) Distribution of the nodal rings in the first BZ. The colors of the nodal rings are the same as the corresponding dots in (b). (d) Spectral variations of the three nodal rings. (e) 3D band diagrams of the first two modes on specified cross sections of the first BZ. Nodal rings formed by their crossings are denoted.

6.2.2 Origin and Analysis of the Nodal Rings

Notably, the nodal rings arise from the fluid-solid interaction, because transverse components of the plates' displacements cannot be neglected. We first evaluate band diagram near Γ point [inset in Fig. 6.1(b)], around which the first four bands are classified as the lowest-order waterborne guided (WG) mode and the three lowest-order plate modes: the flexure Lamb (FL) mode, the extensional Lamb (EL) mode, and the shear horizontal (SH) mode [see Fig. 6.2 for their mode shapes at $\boldsymbol{k}$ = $(0.1\pi/a_0, 0, 0)$]. Far away from the Γ point, the hybridizations between these modes become significant, so that the bands cannot be simply distinguished.

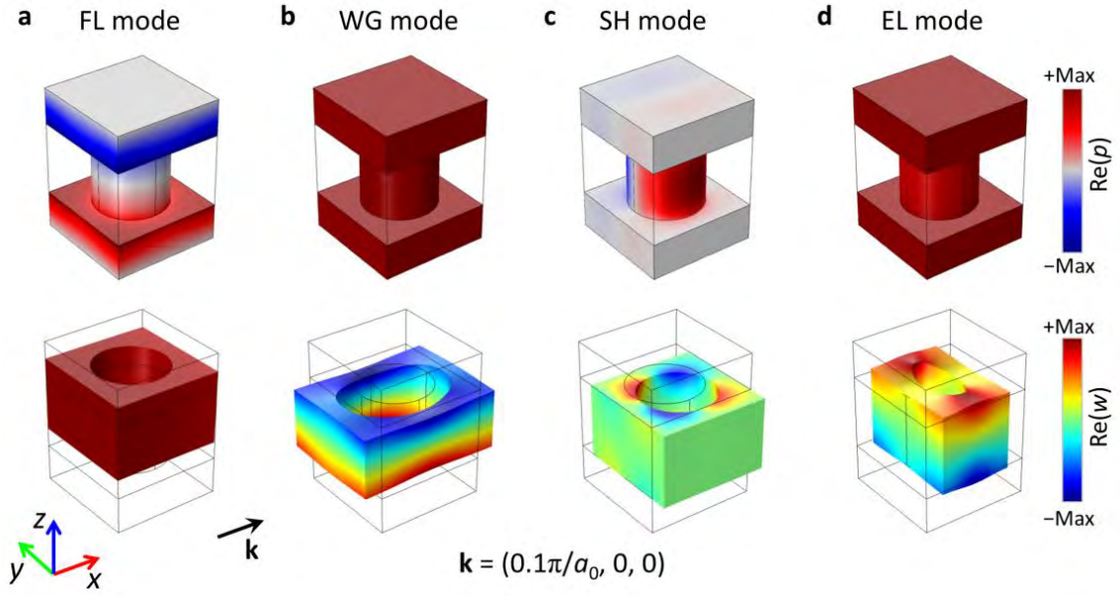

Figure 6.2 Mode profiles of the first four bands around Γ point. (a)-(d) Calculated field maps of the modes at $\boldsymbol{k}$ = $(0.1\pi/a_0, 0, 0)$, including the acoustic pressure (Re(p)) and elastic displacements (Re(u), Re(v), Re(w)). The thin solid lines outline the profile of the unit cells without elastic displacements.

To verify that the fluid-solid interaction cannot be neglected in the "mixture"

phononic crystal, we give the simulated band diagram without the interaction. In this situation, the phononic crystal are modelled only with the Pressure Acoustics module in COMSOL Multiphysics. The longitudinal sound speed of aluminium c_l = 6100 m/s is used in the simulations, and the calculated band diagram is depicted in Fig. 6.3. Only one mode, namely, the WG mode, emerges from Γ point. The SH mode and Lamb modes (both FL and EL modes) originating from solid displacements all disappear.

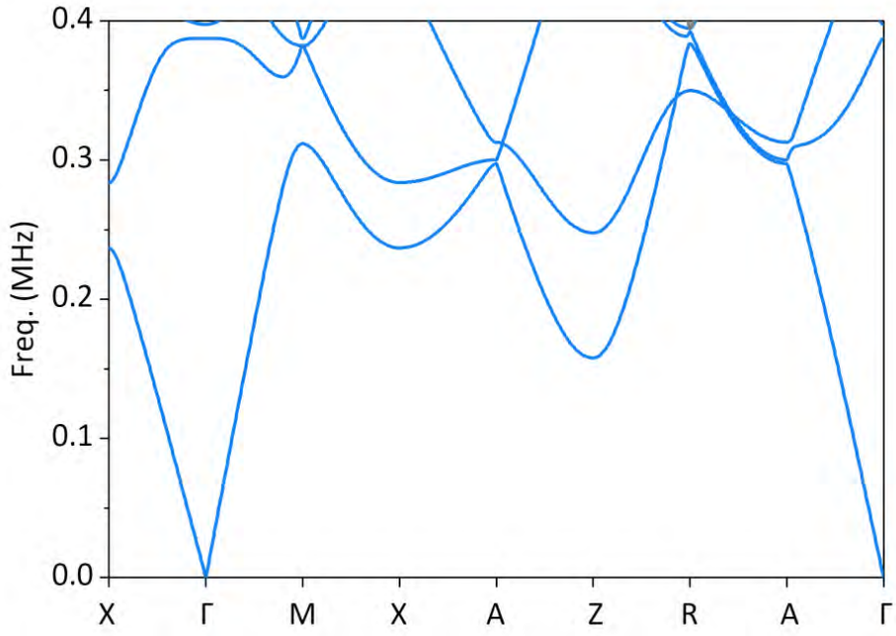

Figure 6.3 Band diagram of the phononic crystal without fluid-solid interaction. We only consider the longitudinal component of the system in the numerical calculations. Resultantly, the SH modes and Lamb modes (both FL and EL modes) that involve shear components disappear.

To shed light on the emergence of the nodal rings, we explore the situation that periodic aluminium plates are arranged in the same manner but without any perforations. The calculated bands still have the intersecting point between the first

and second bands on $k_z = 0$ plane [Fig. 6.4(a)]. In this case, around Γ point with $k_z = 0$, we obtain the band dispersions based on the transfer matrix method (see Appendix H)

$$\omega_{\mathrm{WG}} = c_w k_r$$
$$\omega_{\mathrm{FL}} = \sqrt{\frac{D}{\rho_m t_m + \rho_w t_w}} k_r^2 , \tag{6.1}$$

where $k_r = \sqrt{k_x^2 + k_y^2}$, D and ρ_m are the bending stiffness and density of the plates, c_w and ρ_w are the sound speed and density of the background water. Hence, in the long-wavelength limit, for the FL mode, a quadratic asymptotic behavior $\omega_{\mathrm{FL}} \sim k_r^2$ is observed, which is similar to the case of flexural waves on a free-standing thin plate. In contrast, for the WG mode coinciding with sound cone, a typical linear asymptotic behavior $\omega_{\mathrm{WG}} \sim k_r$ is observed. As they emerge together from Γ point when $k_z = 0$, they will eventually touch each other along a closed loop with both slopes positive, forming a type-II nodal ring [Fig. 6.4(b)]. It is worth noting that this red nodal ring is very robust against various choices of material and geometric parameters.

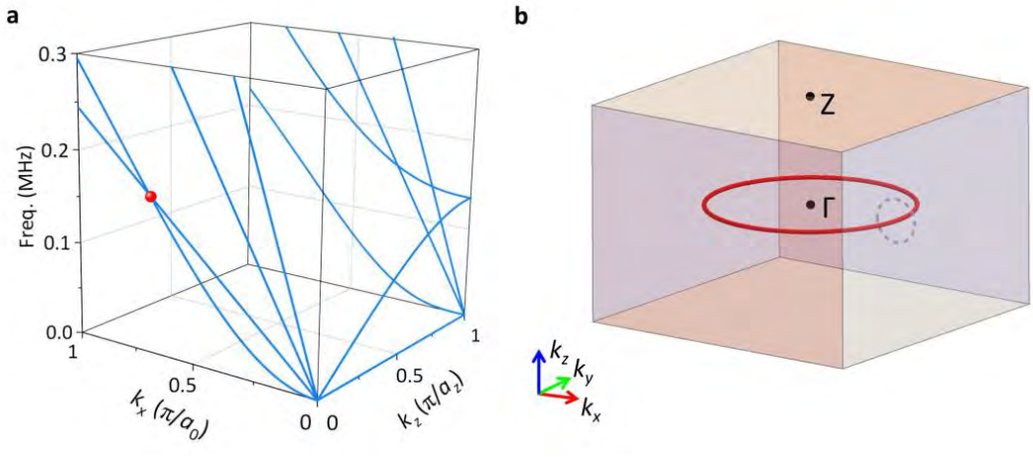

Figure 6.4 Origins and analysis of the nodal rings. (a) Band diagram of periodic metallic plates without perforations. (b) Distribution of the ideal type-II nodal ring for (a).

For example, in Fig. 6.5(a), we show the band diagram of the phononic crystal immersed in air. It can be seen that the inevitable type-II nodal ring on $k_z = 0$ plane still exists. However, the size of the nodal ring is significantly shrunken since the sound speed of air is much smaller when compared with water. Moreover, the sound is also much harder to be transmitted because of the significant impedance mismatch between air and aluminum which gives rise to much weaker fluid-solid interaction. In fact, we have simulated excited of the phononic crystal in water and air at the corresponding frequency of the red nodal ring on $k_z = 0$, respectively. In simulations, the phononic crystal contains 10 layers of the drilled aluminum plates, and the average out-of-plane displacement for each layer is illustrated in Fig. 6.5(b). It can be seen that the sound can hardly be transmitted when the phononic crystal is immersed in air, since the impedance of aluminum is four orders of magnitude than that of air.

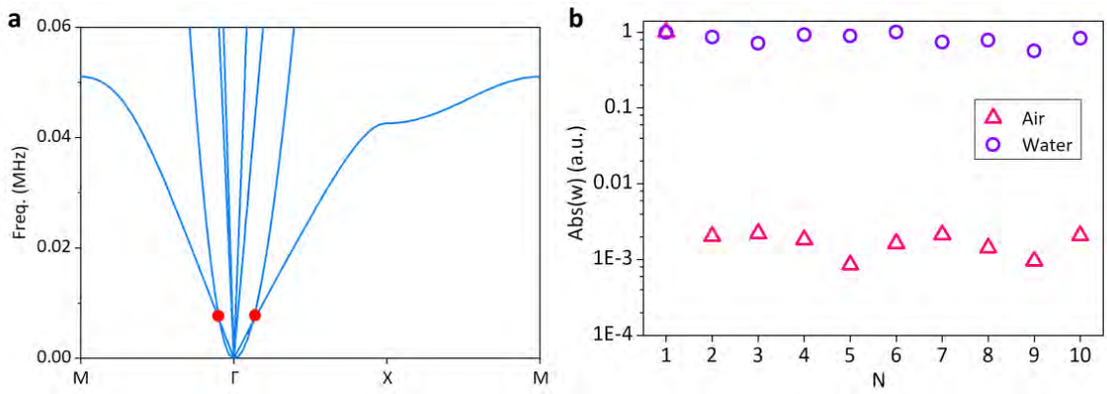

Figure 6.5 Comparison with the phononic crystal immersed in air. (a) The calculated band diagram with $k_z = 0$ when the phononic crystal is immersed in air. (b) The normalized amplitude of averaged out-of-plane displacement (Abs(w)) for each layer of the aluminum plates when excited at the frequency of the nodal ring on $k_z = 0$ for air and water, respectively. The excitation source is placed at the surface (N = 1).

The red nodal ring is related to the plate thickness. We consider the evolution of the nodal rings when we tune the thickness of plates t_m. The calculated band diagrams and distribution of nodal rings are demonstrated in Fig. 6.6. It can be seen that the red nodal ring is shrunken when we increase the thickness of plates t_m, as shown in Figs. 6.6(a) and 6.6(b). On the other hand, if we decrease the thickness of plates t_m, the red nodal ring will expand, touch each other, reconnect, and become centered around M point of first BZ, as shown in Fig. 6.6(c). With further expansion, the red nodal ring will disappear, as shown in Fig. 6.6(d).

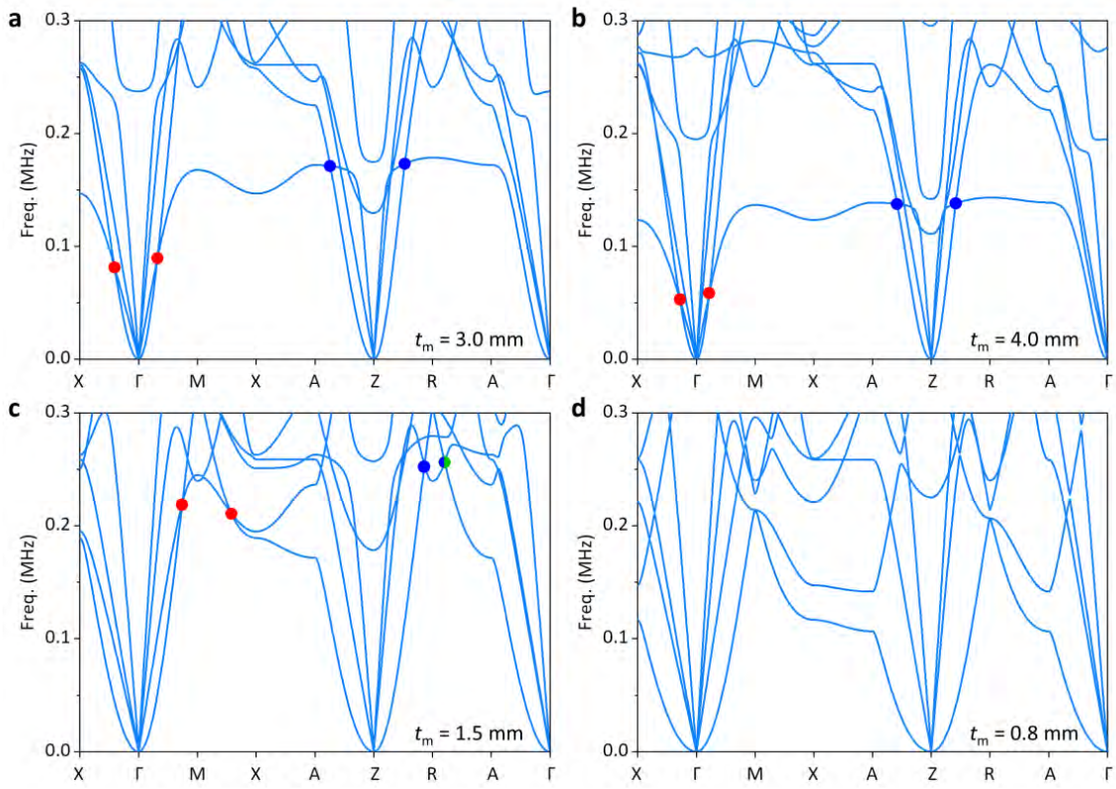

Figure 6.6 Evolution of nodal rings when tuning thickness of plates. (a), (b) Calculated band diagrams when increasing thickness of plates, with t_m = 3.0 mm (a) and t_m = 4.0 mm (b), respectively. (c), (d) Calculated band diagrams when decreasing thickness of plates, with t_m = 1.5 mm (a) and t_m = 0.8 mm (b), respectively.

Different from the robust red nodal rings associated with the plate thickness, the green and blue nodal rings are directly related to the through holes. To make this point clear, we also probe the case of blind holes on the aluminium plates, with the limiting situation that they perforate the plates. The evolution of the band diagram reveals that only the red nodal ring, arising solely from the fluid-solid interaction, can exist with blind holes (Fig. 6.7). The blue and green nodal rings are largely dependent on the acoustic resonance mode of the through holes.

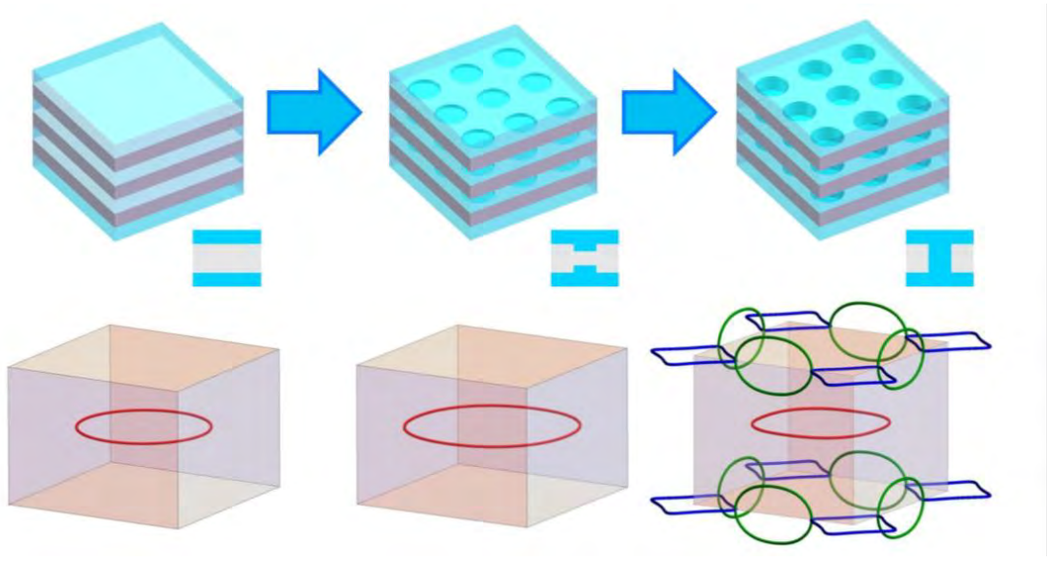

Figure 6.7 Evolution of the nodal rings, from uniform plates to plates with blind holes and finally through holes.

The perforated holes are critical for the emergence of other nodal rings except the red one. To confirm this point, we have calculated the bands of the phononic crystal with the metallic plate assumed to be acoustically rigid. The calculated band diagram is shown in Fig. 6.8(a), and only the blue nodal ring on $k_z = \pi/a_z$ exists, as demonstrated in Fig. 6.8(b). On the other hand, the red nodal ring arising from the fluid-solid

interaction is missing because the plates are now acoustically rigid and cannot support flexural Lamb modes. The results suggest that the blue nodal ring on $k_z = \pi/a_z$ is due to the degeneracy between the WG mode and the acoustic resonance mode of the through holes. Both modes still exist when the plates are acoustically rigid. To demonstrate this point, we plot the field maps of the two modes around the blue nodal ring at $\mathbf{k} = (0.83\pi/a_0, 0.75\pi/a_0, \pi/a_z)$. As shown in Fig. 6.8(c), the two modes indeed have opposite parities with respect to the mirror symmetry M_z, as expected. On the other hand, if the holes are blind holes on the rigid plates, for example, with a separation $t_h = 1.0$ mm between holes on two sides of the plates, we can see that the blue nodal rings will disappear, as shown in Fig. 6.8(d). This fact is because if the holes are blind holes, the frequency of their first-order acoustic resonance will be significantly increased because the effective length of the holes are greatly reduced.

In other words, we can effectively tune the blue nodal rings by tuning the acoustic resonance mode, through changing the thickness of the plates t_m. For example, we consider the case that the holes are through holes, and the thickness of rigid plates is $t_m = 1.0$ mm, while other geometric parameters remain unchanged. The calculated band diagram is shown in Fig. 6.8(e). The blue nodal rings expand and reconnect after touching each other, now centered around R point in the reciprocal space, as demonstrated in Fig. 6.8(f). The green nodal rings now also appear on $k_x = \pi/a_0$ and

$k_y = \pi/a_0$ planes, connected with the blue nodal rings. In fact, the existence of green nodal rings, when the blue nodal rings are centered around R point, is guaranteed by the mirror symmetries with respect to the $k_x = \pi/a_0$ and $k_y = \pi/a_0$ planes in the reciprocal space. The mirror symmetries lead to the opposite orientations of the blue nodal rings on opposite sides of the $k_x = \pi/a_0$ and $k_y = \pi/a_0$ planes [157].

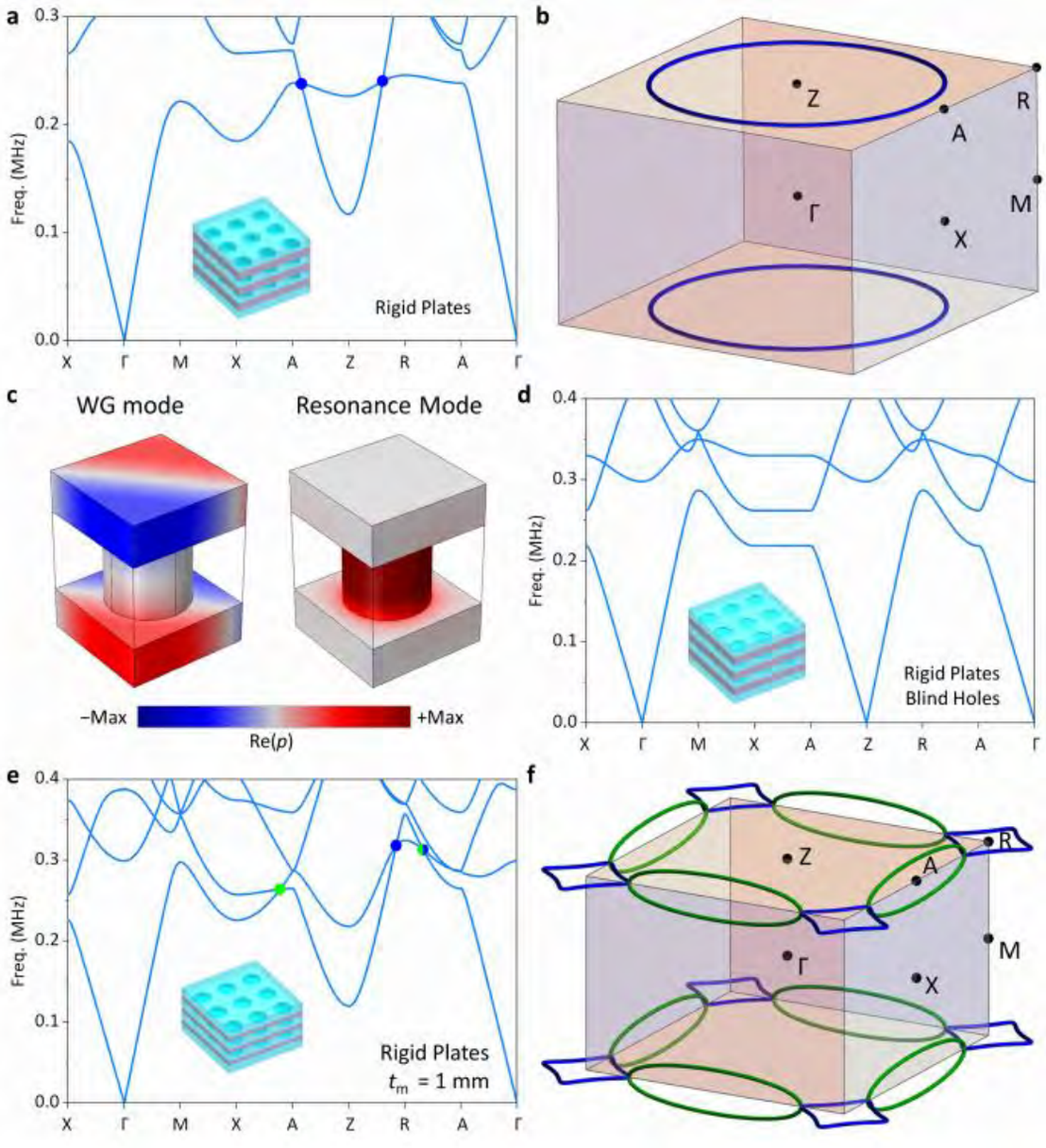

Figure 6.8 Band diagrams when the plates are rigid. (a) Calculated band diagram of the unit cell when its solid domain is acoustically rigid, while geometric parameters are all the same. (b) Distribution of the nodal ring. (c) The field maps of the first two

bands around the blue nodal ring. (d) Calculated band diagaram of the unit cell when the holes are blind holes. (e) Calculated band diagram when the thickness of rigid plates t_m = 1.0 mm. (f) Distribution of the nodal rings.

6.2.3 Experimental Observation of Type-II Nodal Rings

Then, we carry out ultrasonic near-field scanning in fluid to experimentally investigate the type-II nodal rings [158]. When exploring bulk bands with the experimental setup [Fig. 6.9(a)], out-of-plane displacement is produced by a piezoelectric actuator, which couples efficiently with underwater ultrasound. The piezoelectric actuator is attached on one side (facet 1) of the sample by glue, and the ultrasound field on the opposite side (facet 2) is measured point-by-point [Fig. 6.9(b)] by a needle hydrophone. To extract the intensity spectra outside the sound cone in the reciprocal space, the measured fields are then Fourier transformed [159]. The bright strips in the intensity spectra correspond to the excited bulk modes outside sound cone in experiments that is projected over k_z. Their evolution with respect to frequency is indicated in Fig. 6.9(c).

We also extract the intensity spectra along high symmetry lines of the first BZ and compare them with the simulated band diagram projected over k_z [black circles in Fig. 6.9(d)]. In general, the spectra overlap with the black circles from full-wave simulations. For further confirmation, we also performed control experiments with in-plane lattice constant shifted to a_0 = 4 mm, and the measured results also

consistent with corresponding simulations (see Appendix I).

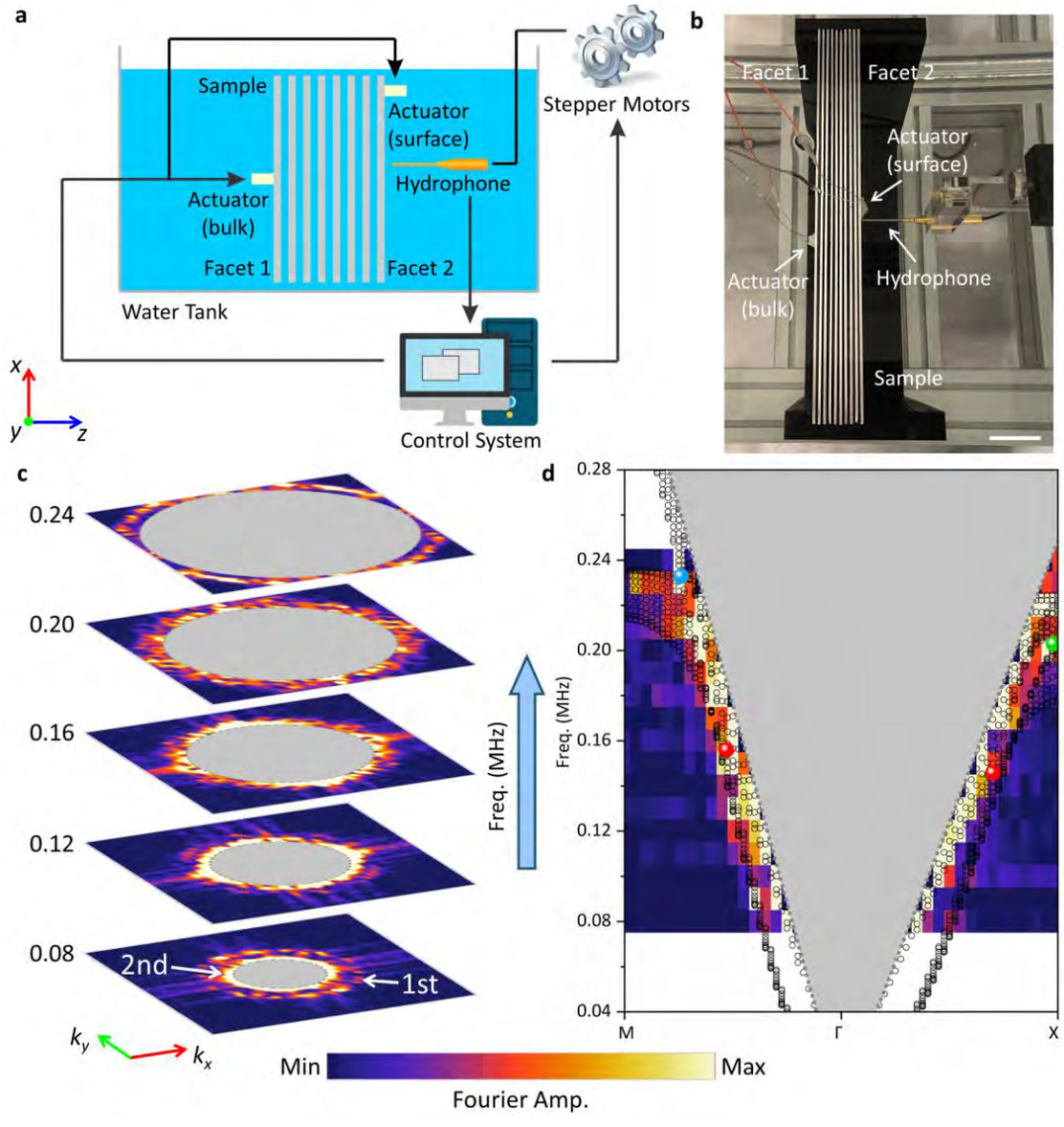

Figure 6.9 Experimental observation of type-II nodal rings. (a) Schematic of experimental setup for near-field scanning. (b) Photograph of the sample and experimental setup. White scale bar: 40mm. (c) Spatial Fourier spectra of experimentally imaged fields at corresponding frequencies. Gray shaded regions: the sound cone projected on the k_x-k_y plane. (d) Experimental Fourier spectra along high-symmetry lines of the first BZ. The coloured dots represent the nodal rings of the same colour denoted in Fig. 6.1(b).

6.3 Strongly Tilted Drumhead Surface State

6.3.1 Distribution of Zak Phase

To further elaborate the topological effects of type-II nodal rings, we also note the existence of drumhead surface state (DSS) between the red type-II nodal ring on k_z = 0 and the blue type-II nodal ring on $k_z = \pm\pi/a_z$. The DSS is closely related to the Zak phase along k_z direction that is quantized owing to the mirror symmetry M_z ($z \to -z$) of the phononic crystal. An eigenmode of the phononic crystal which includes fluid-solid interaction is generally comprised of ultrasound in both the fluid domains (described by acoustic pressure p) and the solid domains (described by displacement **u**). We can define the inner product of two eigenmodes $|n_1\rangle$ and $|n_2\rangle$ of the phononic crystal as [160, 161]

$$\begin{aligned}\langle n_1|n_2\rangle = &\int_{V_\mathrm{w}} \frac{1}{4\rho_\mathrm{w}c_\mathrm{w}^2}\, p_1^*(\mathbf{r})\, p_2(\mathbf{r})\mathrm{d}^3\mathbf{r} + \int_{V_\mathrm{w}} \frac{\rho_\mathrm{w}}{4}\, \mathbf{v}_{\mathrm{w}1}^*(\mathbf{r})\cdot\mathbf{v}_{\mathrm{w}2}(\mathbf{r})\mathrm{d}^3\mathbf{r} \\ &+\int_{V_\mathrm{m}} \frac{1}{4}\, \mathbf{e}_1^*(\mathbf{r})\cdot\mathbf{C}\cdot\mathbf{e}_2(\mathbf{r})\mathrm{d}^3\mathbf{r} + \int_{V_\mathrm{m}} \frac{\rho_\mathrm{m}}{4}\, \mathbf{v}_{\mathrm{m}1}^*(\mathbf{r})\cdot\mathbf{v}_{\mathrm{m}2}(\mathbf{r})\mathrm{d}^3\mathbf{r}\end{aligned}, \tag{6.2}$$

where V_w and V_m denoting the fluid and solid domains of the unit cell, respectively. In the integrals, $p_1(\mathbf{r})$ and $p_2(\mathbf{r})$ are periodic part of pressure field for $|n_1\rangle$ and $|n_2\rangle$, $\mathbf{e}_1(\mathbf{r})$ and $\mathbf{e}_2(\mathbf{r})$ are periodic part of strain field for $|n_1\rangle$ and $|n_2\rangle$. The elastic strain tensor **e** is defined as

$$e_{ij} = \frac{1}{2}\left(\frac{\partial u_i}{\partial x_j} + \frac{\partial u_j}{\partial x_i}\right), \tag{6.3}$$

where u_i (i=1,2,3) are components of displacement and x_i (i=1,2,3) are coordinates, respectively. **C** is the stiffness tensor connecting stress and strain of the solid, which is expressed as

$$\begin{bmatrix} \sigma_{11} \\ \sigma_{22} \\ \sigma_{33} \\ \sigma_{12} \\ \sigma_{13} \\ \sigma_{23} \end{bmatrix} = \mathbf{C} \begin{bmatrix} e_{11} \\ e_{22} \\ e_{33} \\ 2e_{12} \\ 2e_{13} \\ 2e_{23} \end{bmatrix}, \tag{6.4}$$

with

$$\mathbf{C} = \frac{E}{(1+\nu)(1-2\nu)} \begin{bmatrix} 1-\nu & \nu & \nu & & & \\ \nu & 1-\nu & \nu & & & \\ \nu & \nu & 1-\nu & & & \\ & & & \frac{1}{2}-\nu & & \\ & & & & \frac{1}{2}-\nu & \\ & & & & & \frac{1}{2}-\nu \end{bmatrix}. \tag{6.5}$$

For simplicity, the symmetric 3×3 strain tensor is rearranged into a 6-component vector $\mathbf{e} = [e_{11}, e_{22}, e_{33}, 2e_{12}, 2e_{13}, 2e_{23}]^{\mathrm{T}}$. The particle velocity of ultrasound in the fluid is

$$\mathbf{v}_{\mathrm{w}} = \frac{\nabla p}{i\omega\rho_{\mathrm{w}}}, \tag{6.6}$$

while the particle velocity of ultrasound in the solid is

$$\mathbf{v}_{\mathrm{m}} = -i\omega\mathbf{u}. \tag{6.7}$$

Then, the eigenmodes can be normalized, and the Berry connection of the l-th band is then

$$B_l(\mathbf{k}) = i\left\langle n_{l,\mathbf{k}} \middle| \nabla_{\mathbf{k}} n_{l,\mathbf{k}} \right\rangle, \tag{6.8}$$

where $\left|n_{l,\mathbf{k}}\right\rangle$ is the normalized eigenstate of l-th band at $\mathbf{k}$ in the reciprocal space. Correspondingly, the Zak phase $\theta_l^{\text{Zak}}(k_x, k_y)$ along k_z direction of l-th band can be directly evaluated as (up to 2π)

$$\theta_l^{\text{Zak}}(k_x, k_y) = \int_{-\pi/a_z}^{\pi/a_z} B_{l,z}(\mathbf{k}) \mathrm{d}k_z \,. \tag{6.9}$$

In our numerical calculations, we discretize Eq. (6.9), and the results for the first band of selected lines in the surface first BZ are plotted in Fig. 6.10. It can be seen that the numerical results agree quite well with the theoretical results inferred from the distribution of nodal rings. The numerical errors are within ±0.05 and can be further decreased by refining the discretization of k_z.

In fact, since the phononic crystal has mirror symmetry with respect to z direction, the Zak phase θ_1^{Zak} can also be inferred from parities of the eigenmodes at high symmetry points along the k_z path ($k_z = 0$ and π/a_z). Namely, we have [161]

$$\frac{\theta_1^{\text{Zak}}}{\pi} = \{\frac{1}{2}[M_{z,1}(k_z = 0) - M_{z,1}(k_z = \pi / a_z)]\} \bmod 2\,, \tag{6.10}$$

where $M_{z,1}$ are parities (±1) for mirror symmetry M_z ($z \to -z$) of the 1st band at $k_z = 0$ and π/a_z, respectively. The field maps of the eigenmodes at $k_z = 0$ and $k_z = \pi/a_z$ for $\mathbf{k}_r = (k_x, k_y) = (0.6\pi/a_0, 0)$ and $(0.8\pi/a_0, 0)$ are shown in Figs. 6.10(c) and 6.10(d), respectively. It shows that, for mirror symmetry M_z, the eigenmodes at $k_z = 0$ and π/a_z have the same parity when $\mathbf{k}_r = (0.6\pi/a_0, 0)$, but opposite parities when $\mathbf{k}_r = (0.8\pi/a_0, 0)$. This contrast confirms that the Zak phase takes the value 0 for the former case

and π for the latter case, as we have numerically demonstrated.

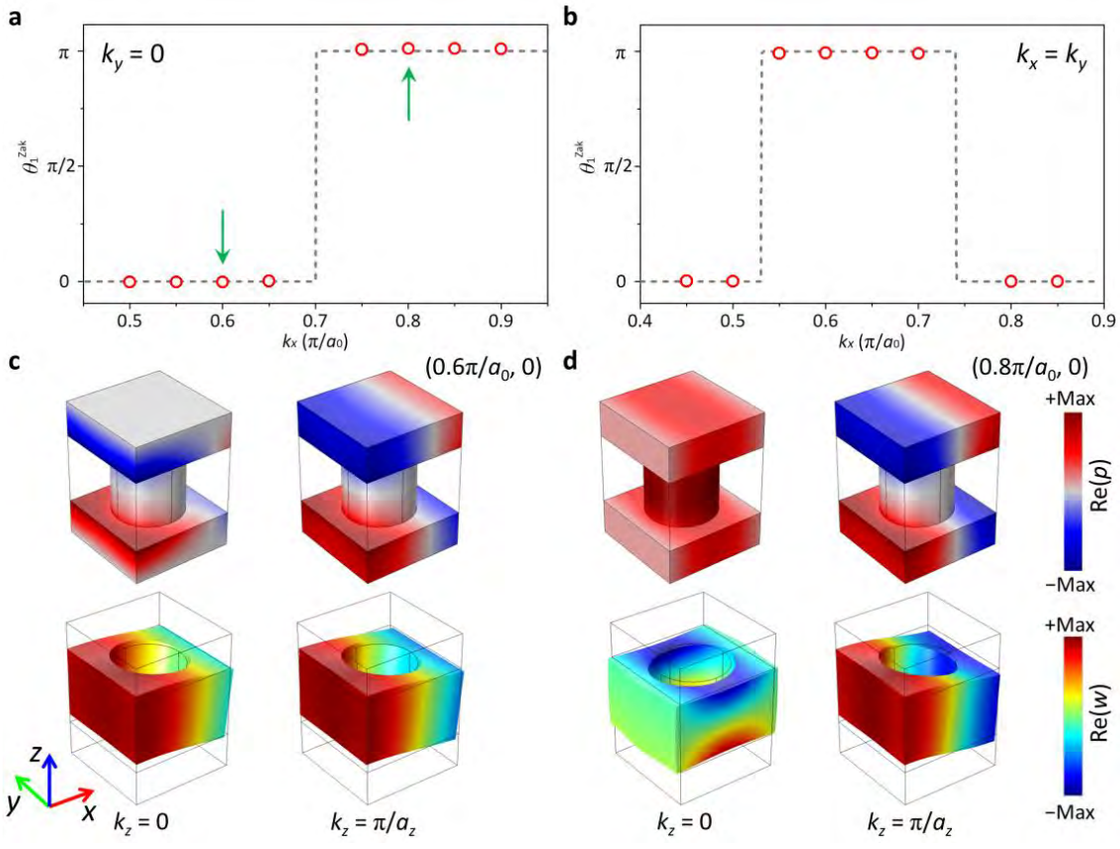

Figure 6.10 Numerical calculation of Zak phases. (a), (b) Numerically calculated Zak phases along the line $k_y = 0$ (a) and $k_x = k_y$ (b) in the surface first BZ. The dots represent numerical values calculated from full-wave simulations, and dashed lines represent theoretical values obtained from the distribution of nodal rings. (c), (d) Field maps of the eigenmodes of the first band at $k_z = 0$ and $k_z = \pi/a_z$, respectively, corresponding to $k_r = (0.6\pi/a_0, 0)$ (c) and $k_r = (0.8\pi/a_0, 0)$, indicated by arrows in (a).

6.3.2 Experimental Observation of the Drumhead Surface State

The different values of the Zak phase in the surface first BZ [Fig. 6.11(a)] is just distinguished by the projection of the two nodal rings on k_x-k_y plane [162], implying possible existence of DSS in the region with nonzero Zak phase [163]. The calculated projected band diagram of a ribbon supercell terminated by its *x*-*y* surface

demonstrates that a strongly tilted DSS appears in the partial band gap [Fig. 6.11(b)], a typical characteristic of the topological effect of the type-II nodal rings. This strong tilting property is different form DSSs of type-I nodal rings, where they are generally flat. The field profiles of the strongly tilted DSS [Fig. 6.11(c)], including both acoustic pressure (left panel) and out-of-plane displacement (right panel), confirm that the DSS is a hybridized states with energy, both in water and plates, localized on the surface of the phononic crystal.

Lastly, based on the generally same experimental setup but the actuator and hydrophone now on the same *x*-*y* surface [facet 2 in Fig. 6.9(a)], we experimentally observe the strongly tilted DSS. We carry out the similar near-field scanning and the measured field profiles (see Appendix J) are then Fourier transformed again to show band diagram in the reciprocal space. The excited modes manifested in the extracted intensity spectra [Fig. 6.11(d)] show good consistency with numerical simulations, thereby evidencing the existence of the DSS together with its critical feature, the strong tilting shape. Since we cannot completely avoid exciting bulk states, bright stripes at low frequency range also observed in Fig. 6.11(d). To further support our findings, control experiments are also performed (see Appendix I).

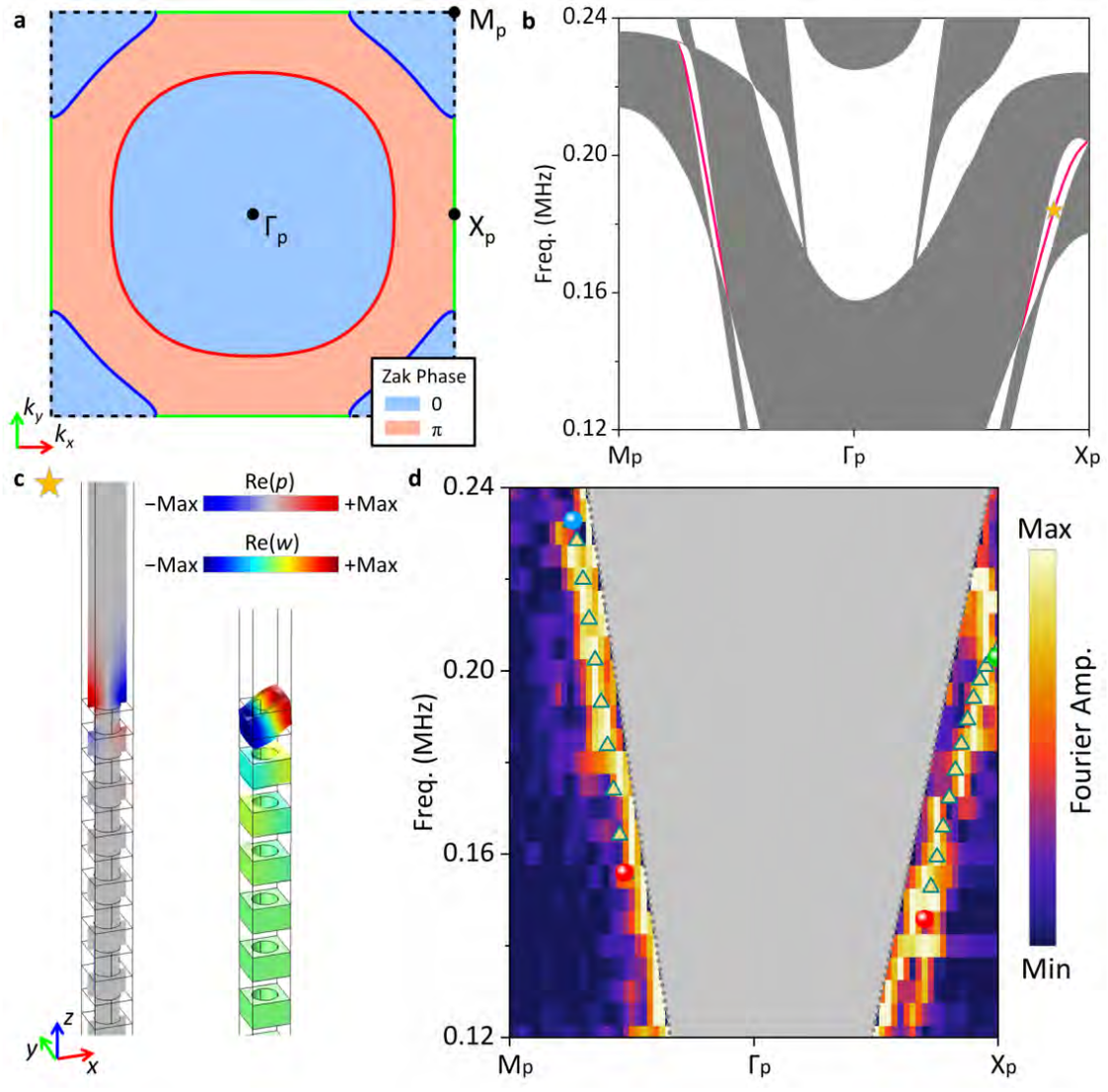

Figure 6.11 Strongly tilted DSS between nodal rings. (a) Distribution of Zak phase on the surface first BZ projected along *z* direction. (b) Calculated band diagram of a supercell terminated by *x*-*y* surface. Red lines denote the strongly tilted DSSs. Gray shaded regions denote the projected bulk bands. (c) Calculated field profiles of acoustic pressure (Re(*p*)) and elastic displacements (Re(*u*), Re(*v*), Re(*w*)) for the marked point in (b). The thin solid lines outline the profile of the supercell without elastic displacements. (d) Experimental Fourier spectra along high-symmetry lines when launching and measuring the ultrasound at the same side of the phononic crystal. Triangle scatters: the simulated dispersion of the strongly tilted DSSs along the high-symmetry lines.

6.4 Summary

In this chapter, we present an approach for constructing topological phononic systems, based on which we realize type-II nodal rings in a phononic crystal and experimentally demonstrate the associated critical features with a underwater ultrasonic experimental environment. In view of the fact that the simple design only involves perforation during manufacturing, it can be readily rescaled to shorter wavelength regimes and may inspire on-chip devices. Using symmetry representation as a guidance, our approach reveals how fluid-solid interaction for sound can lead to unique behavior and hence enrich topological physics. Our findings expand topological systems and can serve as platforms to explore topological physics in a much simpler manner, not to mention the significantly reduced thermo-viscous losses of sound in water compared with air [96]. Remarkably, the rich physics discovered in this platform may also advance theoretical studies and experimental realizations of other nodal-line topologies, such as non-Abelian nodal links [157] and topological charges [164].

CHAPTER 7

Concluding Remarks and Recommendations for Future Study

7.1 Concluding Remarks

Topological phononics is an interdisciplinary subject combining condensed matter physics, acoustics and solid mechanics. Taking advantages of topological protection, these designed artificial structures can flexibly and robustly manipulate sound waves. Early works on topological phononics were restricted to searching the counterparts of TIs and TSMs that were previously proposed in condensed matter systems. Nowadays, topological phononics can even advance the study of TIs, shedding a new light on general topological physics and innovating novel applications not accessible with conventional materials, e.g., topological phases with non-Hermiticity and synthetic dimensions [46]. In this thesis, we have experimentally demonstrated three different topological phenomena induced solely by non-Hermiticity, that are, in-gap and in-band topological edge localizations based on the 1D elastic lattices and reconfigurable first-order and second-order topological states in 2D acoustic lattices, respectively. Furthermore, by combining the fluid-borne and solid-borne sound together by immersing the layer-stacked perforated elastic plates into water in

experiments, the formed 3D phononic crystal with fluid-solid interaction shows fascinating type-II nodal rings and associated DSSs. Our works open up new approaches to exploring unique topological physics for sound applications such as noise control, ultrasound imaging, underwater communications and so on.

In the designed 1D topological structures, we have proposed the elastic analogues of the SSH model under Hermitian and non-Hermitian modulations, with perturbative elastic metamaterials consisting of square plates connected by thin beams. By setting alternating coupling strengths in the hypothetically Hermitian case and judiciously tailored damping treatments in the non-Hermitian case, the in-gap and in-band topological edge states have been experimentally observed, in which non-Hermiticity stands out as a non-trivial factor that fundamentally alters the system's topology beyond conventional Hermitian configurations. This new non-Hermitian mechanism for achieving topological edge states is generally applicable to diverse systems and is simple to realize.

By further extending the 1D lattice to 2D, we have utilized an acoustic QTI to evidently demonstrate that all the topological states could be flexibly engineered to arbitrary sites, simply by tailoring the non-Hermitian configurations. This strategy is fundamentally distinct from the Hermitian counterpart, where the inter-cell and intra-cell hopping strengths should be changed to induce the phase transition. Moreover, in light of the rising demand of miniaturized and integrated topological devices, our study could facilitate the practical application due to the full usage of the lattice. This non-Hermitian scheme can be readily generalized to other topological systems in

various dimensions, such as the 3D photonic/phononic lattices, which offers advanced and externally controllable recipes for observing topological phenomena.

Previous searches for phononic topological phases only concern sound in either fluids or solids alone, overlooking any prospect of novel topological physics stemming from their interactions. What if we “mix” them in a phononic system? In Chapter 6, we report the first experimental obserbation of type-II topological nodal rings in phononics by considering both vectorial and scalar nature of the sound. Specifically, with a strong band tilting, type-II nodal lines show many special physical phenomena in contrast to their conventional type-I counterparts, including anisotropic transports, conical diffractions, and tilted DSSs. Among them, the tilted DSSs are also experimentally observed. As nodal lines are basic building blocks of topological phenomena in the momentum space, our approach could reveal more complex topological physics in phononics. We believe that this approach can be regarded as a vital milestone in topological phononics and offers a much simple and flexible platform to implement interesting topological physics.

7.2 Recommendations for Future Study

With the promising outcomes listed in this PhD thesis, we envisage that this trend for studying topological phnonics will hold for the next several years. But still, we would like to point out several existing challenges and potential research directions.

To date, the experimental studies of non-Hermitian topology remain dominated by classical wave (including sound waves) platforms. We expect that the interest on non-Hermitian topological phononics, as our main works discussed in this thesis, will continue to increase in future studies especially if further introducing active elements [165, 166] to enable gain effect and control the topological states externally. Non-Hermiticity is usually created by the interaction of a system with external elements that excluded by Hermitian frameworks that regard the external DOFs as perturbations. The suitable treatments of the external DOFs are formed when the non-Hermitian parameters go beyond perturbations but play vital roles in the topology therein. Non-Hermitian topology in sound waves may also inspire insightful designs such as non-Hermitian topological whispering-gallery [167].

When it comes to topological phenomena in 3D, many types of band degeneracies are still unexplored in sound waves, such as higher-order Weyl points, higher-order DPs and different types of nodal lines. Our work on 3D phononic crystals immersed in water reveals that the interaction between the fundamentally different wave dynamics of fluid-borne and structure-borne sounds can be a key to the rich topological properties absent in pure fluid or solid environments, especially under the guidance of symmetry representation. For example, the type-II nodal rings can be gapped into ideal type-II Weyl points [168, 169] by lowering the symmetry of the phononic crystal. In Figs. 7.1(a) and (b), we lower the symmetry of the unit cell by adding two orthogonal through holes on the aluminum plates. The geometric

parameters are t_m = 3.0 mm, t_w = 2.0 mm, d_0 = 1.6 mm, d_1 = 1.0 mm, and δ_z = 0.9 mm. The calculated band diagram shown in Fig. 7.1(c) confirm that the red nodal ring in Fig.6.1(b) is now broken, giving rise to two pairs of type-II Weyl points at the diagonals of k_z = 0 plane.

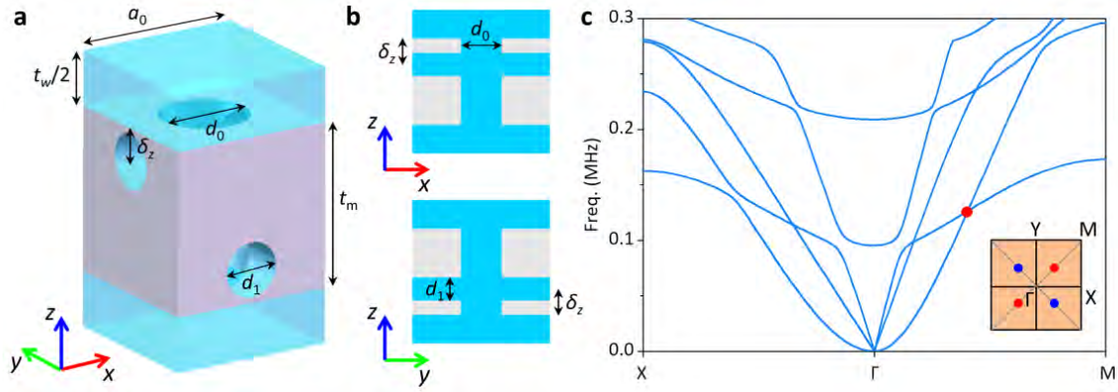

Figure 7.1 Type-II Weyl points from lowering symmetries. (a) Schematic of the unit cell with lower symmetries. (b) Sectional schematics of the unit cell. (c) The calculated band structure on k_z = 0. Inset shows the distribution of type-II Weyl points of opposite charges on k_z = 0 plane.

For potential applications, topologically protected surface, edge and corner states could benefit some engineering areas, such as sound or vibration energy harvesting [170] when combined with piezoelectric materials, topological sensors [171, 172] with high quality factor, and acoustic or elastic wave filters [173]. In addition, by redistributing the wave field based on topology, structural failure induced by concentration of vibration energy may be avoided. However, some challenges still need to be overcome to push topological phononics research into real-world applications. For example, to achieve high efficiency energy harvesting, we need to seek methods to improve the energy exchange rate from vibration to electricity. Besides, for better application of topological phnonics in medical field, how to

increase the effective frequency into the ultrasound and even hypersound ranges is still a question as most works have been focused on audible frequency ranges with long wavelengths.

Appendix

A. Tight-binding Model Calculation

The physics of our elastic counterparts of the SSH chain can be described by a TBM only involving the first non-rigid mode and nearest-neighbor couplings between plates. For the tight-binding Hamiltonian given by Eq. (3.1) in the main text, by setting f_0 = 1536 Hz, γ = 10 Hz and λ = 50 Hz, the calculated band diagram shown in Fig. A1(a) matches well with the bule dotted bands in Fig. 3.2(c) obtained from full-wave simulation. In the same way, for Eq. (3.5) in the main text, the band diagram from the TBM [Fig. A1(b)] generally overlaps with the dotted bands in Fig. 3.7(c) from full-wave simulation due to the fitted parameters as $f_0^{'} = 1133$ Hz, $\kappa = 18.85$ Hz, d_0 = 0.0061 and d_1 = 0.041. Note that, the lower two bands and upper two bands in Fig. A1(b) are fully overlapped because of the ignorance of other higher-order modes and non-nearest-neighbor couplings in the TBM.

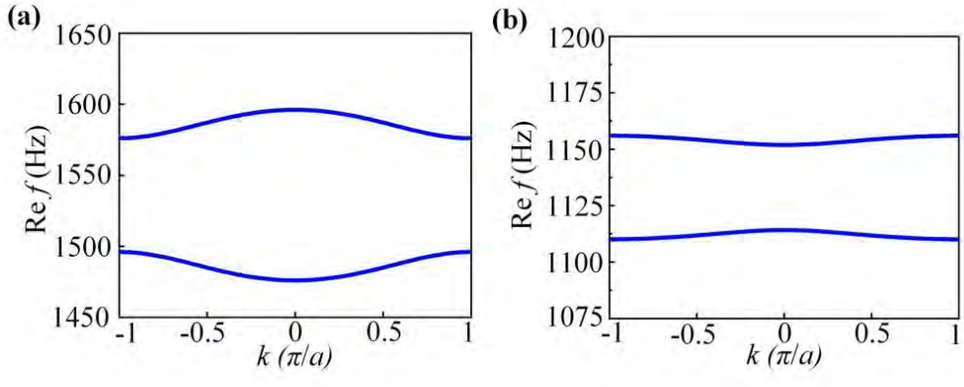

Figure A1 Band diagrams of the lattice in (a) Fig. 3.2(a) and (b) Fig. 3.7(a) in the main text based on TBM.

The eigenfrequency distributions rely on the coupling difference, $\lambda-\gamma$, for the Hermitian case, and on the damping difference, d_1-d_0, for the non-Hermitian case. To evaluate their effect on each case, we calculate the eigenvalues based on the TBM by keeping γ = 10 Hz (or d_0 = 0.0061) intact and increasing the value of λ (or d_1) in the Hermitian (or non-Hermitian) chain. As depicted in Fig. A2(a), under Hermitian modulation, the band gap is gradually enlarged with the increase of $\lambda-\gamma$, and the edge states always pinned on the mid-gap. In comparison, the band gap in the non-Hermitian case is broadened at the beginning but keeps unchanged after the damping difference reaching a typical value ($d_1-d_0=0.332$) limited by the coupling terms (κ = 18.85 Hz). In both cases, the in-gap edge states emerge for a non-zero coupling or damping difference. The red lines denote the parameter values used in the main text, which are also chosen for experiments as the edge states and bulk states are clearly separated at these values.

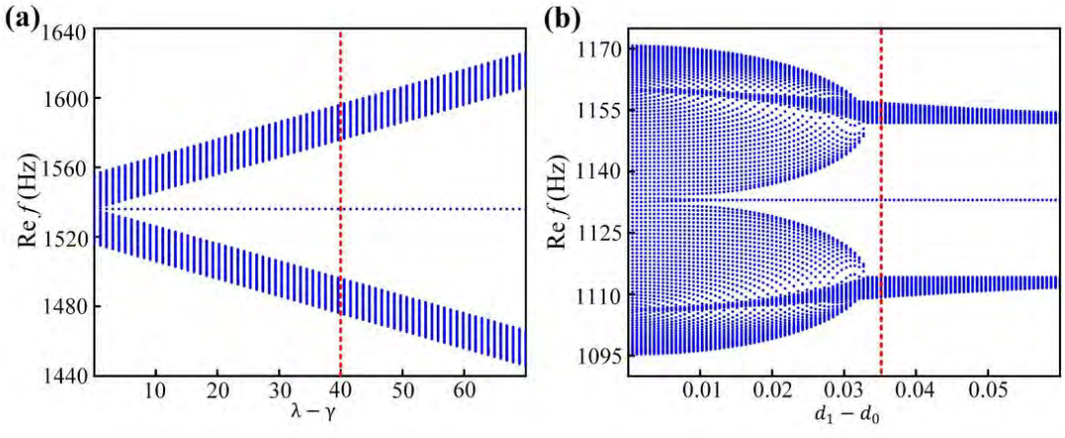

Figure A2 Calculated eigenfrequencies for a 1D finite-sized Hermitian chain as a function of (a) $\lambda-\gamma$ and (b) d_1-d_0.

B. Adjusting the Frequency Deviation due to Coupling Beams

The deviated frequency of zero-energy edge states [δf in Eq. (4.1) of the main text] is introduced due to the perturbation of connecting beams. This global offset of eigenfrequencies does not affect the topological properties of the structure and can be modulated to approach zero by optimizing the geometric parameters of the connecting beams. In Figs. A3(a) and A3(b), as the plates are still those in Fig. 4.1, the concerned resonance frequency of the single plate (f_0) remains to be 2640 Hz. By setting the sizes of the linking beams to be 22.5 mm × 1.5 mm × 0.69 mm and the distance to the horizontal nodal line [also the central line of the plate due to the mode profile in Fig. 4.2(d)] to be h = 9 mm, the value of δf can be tuned to zero, and the in-band topological states fixed at the zero-energy frequency of $f_0 = 2640$ Hz.

Here, the tight binding Hamiltonian matrices without frequency deviation take the form of

$$H(k) = \begin{pmatrix} (1 - d_0 i) f_0 & \kappa & \kappa e^{-ika} \\ \kappa & [1 - (d_0 + d_1) i] f_0 & \kappa \\ \kappa e^{ika} & \kappa & (1 - d_0 i) f_0 \end{pmatrix} \quad \text{(A1)}$$

where a = 187.5 mm, $f_0 = 2640$ Hz, $\kappa = 22$ Hz, $d_0 = 0.0041$ and $d_1 = 0.02$. As depicted in Figs. A3(c) and A3(d), the calculated band diagrams based on the TBM

agree well with those obtained from numerical simulation. Note that the thickness of linking beams must be smaller than the plates to eliminate the frequency deviation, which greatly increases the difficulty for sample manufacturing by laser cutting. Hence, the frequency deviation is kept in the theoretical consideration in the main text to facilitate the experimental investigation.

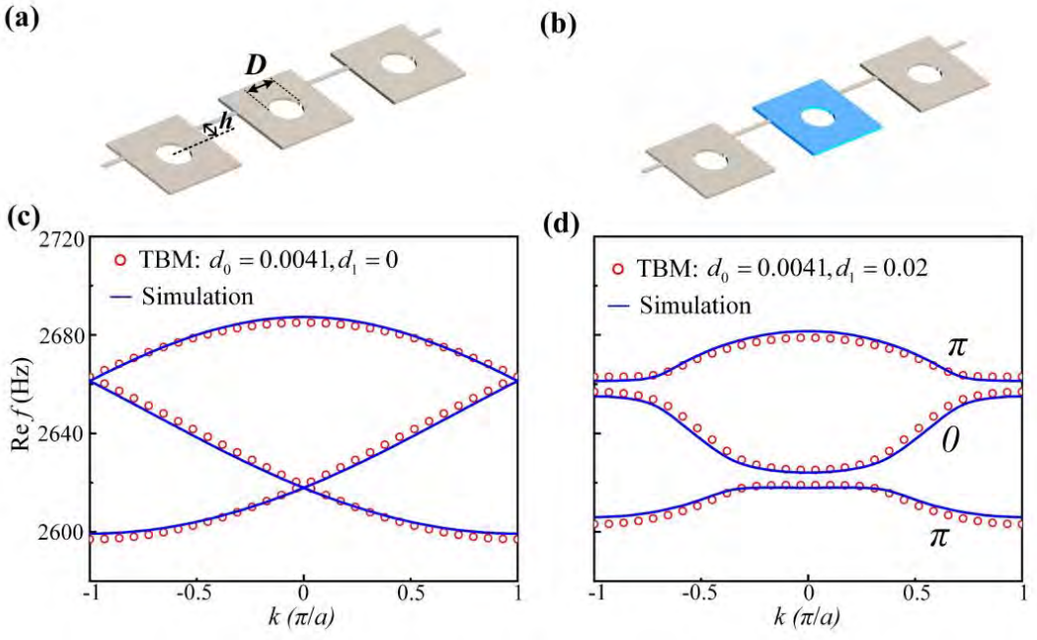

Figure A3 Eliminating the deviation in frequency through design optimization. (a), (b) Schematics of the unit cells for the trimerized lattices with only intrinsic material damping and with AD treatment in the middle plate colored in blue, respectively. (c), (d) Calculated band diagrams corresponding to the unit cells in (a) and (b), respectively. The red circles present the TBM results, and the blue solid lines denote the numerical results.

C. Eigenfrequency Evolution with Increased non-Hermitian Modulation

Based on the TBM, here we consider two finite-sized chains similar to those in the

main text (with and without boundary defects) but having much more unit cells and examine the evolution of their eigestates with respect to increased non-Hermitian modulation. The first chain contains 40 complete non-trivial unit cells (120 sites in total), and the second one contains 39 complete non-trivial unit cells and 2 defective unit cells at the two ends (119 sites in total). The calculation results as given in Fig. A4 are derived by fixing the intrinsic loss $d_0 = 0.0041$ and gradually increasing the value of the modulation loss (non-Hermitian modulation) d_1. As can be seen from Figs. A4(a) and A4(d), the eigenfrequencies of the two chains vary similarly as a function of the loss difference $d_1 - d_0$. No obvious band gap exists at relatively small value of $d_1 - d_0$ (< 0.004), and then two band gaps emerge and are gradually broadened until the value of $d_1 - d_0$ reaches 0.027, beyond which the band gaps become unchanged due to the limited coupling terms (κ = 16 Hz). However, only the chain without defects possesses the edge states which locate at 2676 Hz among the bulk eigenstates, as marked by the red boxes in Figs. A4(a) and A4(b). The vertical red dotted lines in Fig. A4 indicate the value used in the main text, that is $d_1 - d_0 = 0.0159$. The corresponding displacement field profiles at this value are respectively plotted in Figs. A4(c) and Figs. A4(f), demonstrating that the edge states are well located at the leftmost and rightmost sites, which are consistent with the mode profiles in Fig. 4.2(c).

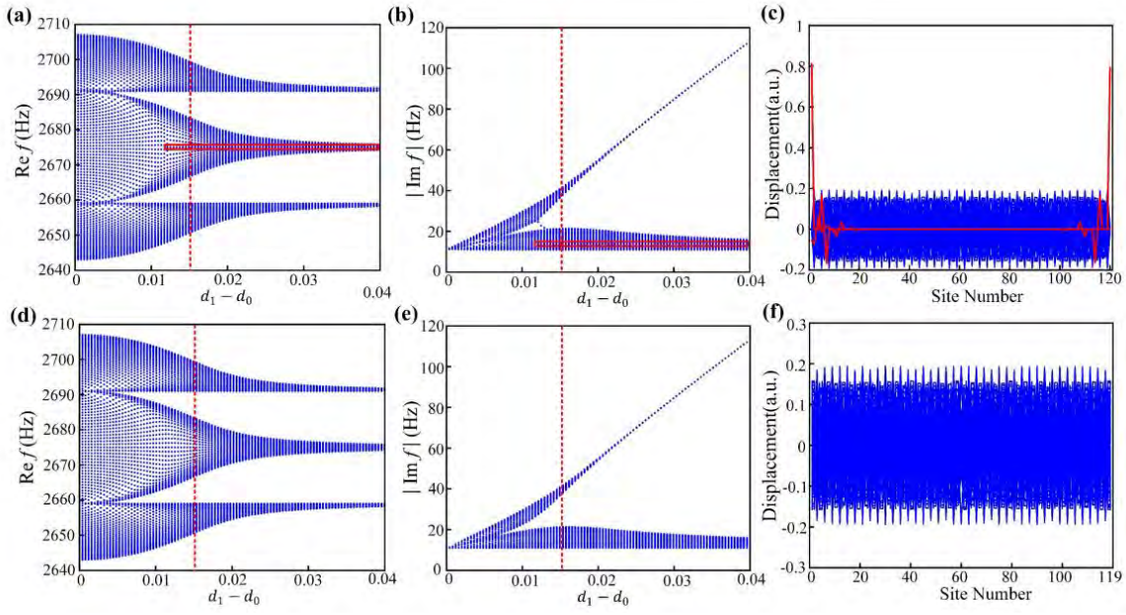

Figure A4 Eigenfrequency evolution as a function of increased non-Hermitian modulation for two long chains. Calculated real parts (a) and imaginary parts (b) of the complex eigenfrequencies for a finite-sized chain without defect. (c) Displacement field profiles of the eigenstatess at $d_1 - d_0 = 0.0159$ marked by the vertical red dotted line in (a). The red curves indicate the field distributions of two edge states. Calculated real parts (d) and imaginary parts (e) of the complex eigenfrequencies for a chain with a defect at each end. (f) Displacement field distributions of the eigenmodes at $d_1 - d_0 = 0.0159$ marked by the vertical red dotted line in (d).

D. Frequency Response Function Spectrum for the Host Plate without the Hole

We measure the FRF curve of the host plate [Fig. A5(a), which is also the yellowish layer of Fig. 4.6(a)], and its resonant peak is observed at 2922 Hz with a quality factor of ~115. Therefore, the circular hole in Fig. 4.6(b) is introduced to facilitate the tuning of the resonant frequency in experiment. It is especially useful in

eliminating the resonance frequency shift induced by the damping treatment.

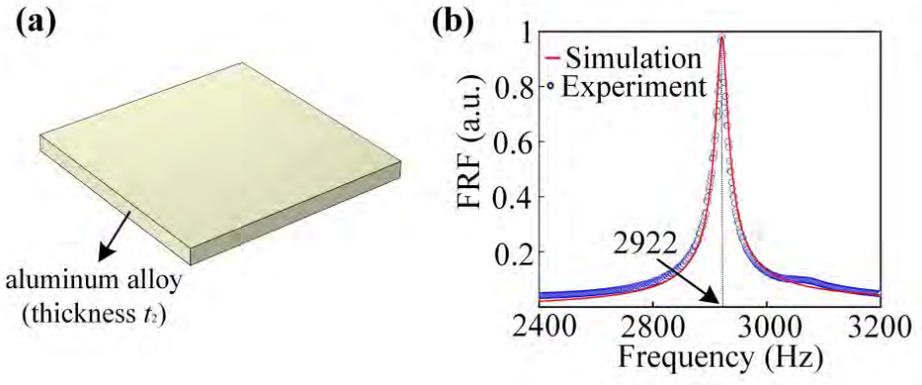

Figure A5 FRF spectra for the host plate. (a) Schematic of the host plate without the hole. (b) FRF spectra for the plate in (a). The blue circles and the red line present the measured and simulation results, respectively.

E. Quadrupole Topological Insulator

The coupled acoustic resonators with a π flux per plaquette can fulfill the requirements of square-lattice TBM which proposed by the QTI theory. The momentum space Hamiltonian of the lattice is

$$H(k_x,k_y)=\begin{pmatrix} f_0 & \varepsilon_1+\kappa_1 e^{ik_y a} & 0 & \varepsilon_1+\kappa_1 e^{ik_x a} \\ \varepsilon_1+\kappa_1 e^{-ik_y a} & f_0 & e^{i\pi}(\varepsilon_1+\kappa_1 e^{ik_x a}) & 0 \\ 0 & e^{-i\pi}(\varepsilon_1+\kappa_1 e^{-ik_x a}) & f_0 & \varepsilon_1+\kappa_1 e^{-ik_y a} \\ \varepsilon_1+\kappa_1 e^{-ik_x a} & 0 & \varepsilon_1+\kappa_1 e^{ik_y a} & f_0 \end{pmatrix}, \quad \text{(A2)}$$

where f_0 corresponds to the zero-energy frequency, ε_1 and κ_1 represent the intracell and intercell coupling strength, respectively, a is the lattice constant. The eigenvalues of Eq. (A2) are

$$f_{1,2}(k_x,k_y)=f_0-\sqrt{2[\varepsilon_1^{\,2}+\kappa_1^{\,2}+\varepsilon_1\kappa_1(\cos k_x a+\cos k_y a)]},$$
$$f_{3,4}(k_x,k_y)=f_0+\sqrt{2[\varepsilon_1^{\,2}+\kappa_1^{\,2}+\varepsilon_1\kappa_1(\cos k_x a+\cos k_y a)]}, \tag{A3}$$

forming two pairs of degenerate bands if $\varepsilon_1 \neq \kappa_1$, as shown by the red circles in Fig. A6(a). By matching this band diagram with the one derived from full-wave simulation, depicted by the blue solid lines in Fig. A6(a), we obtain the parameters in Eq. (A2) as: $\kappa_1 = -25.6$ Hz, $\varepsilon_1 = -5.5$ Hz and $f_0 = 2141$ Hz. Hence, the band gap

$$E_{\text{gap}} = 2\sqrt{2}\left|\kappa_1-\varepsilon_1\right| = 56.8 \text{ Hz} \tag{A4}$$

which is the minimal value of $f_{3,4}-f_{1,2}$.

Not only the eigenvalues of Eq. (A2) can characterize the band feature, its eigenvectors with components $\left[u_n(k)\right]^{\alpha}$ also play a pivotal role in revealing a second-order nontrivial topology. Here n = 1, 2 represent the occupied two bands below the band gap, α = 1, 2, 3, 4 refer to the four acoustic resonators in a unit cell, $k=(k_x,k_y)$ is the wavenumber in the first BZ. After orthogonalized and normalized by $\langle u_m(k)|u_n(k)\rangle = \delta_{mn}$, we define

$$\left[F_x(k)\right]^{mn} = \left\langle u_m(k)\middle|\partial k_x\middle|u_n(k)\right\rangle \tag{A5}$$

with fixed k_y and discretized k_x. The bracket notation $\left|u_{n(m)}(k)\right\rangle$ denote the eigenvector. Then the Wilson loop operator along a closed loop in the k_x direction takes the form of

$$W_x(k_y) = F_x(k+N_x\Delta k_x)\cdots F_x(k+\Delta k_x)F_x(k), \tag{A6}$$

where N_x is the number of discrete points and $\Delta k_x = 2\pi/a/N_x$. The corresponding

Wannier Hamiltonian is defined as

$$H_{W_x}(k_y) = -\frac{i}{2\pi}\log(W_x(k_y)). \tag{A7}$$

As $H_{W_x}(k_y)$ is a two-by-two matrix, it has two eigenvalues $v_x^j(k_y)$, $j=+,-$ represent the upper and lower Wannier bands in Fig. A6(b), and their separation is named as Wannier gap. Each Wannier band can possess its own topological invariant owing to the gap property. The nest Wilson loop approach is an effective way to obtain the topological invariant of Wannier bands. Firstly, in order to split the original degenerated bands below the original band gap in Fig. A6(a), a well-defined subspace can be written as

$$\left|\omega_x^{+(-)}(k)\right\rangle = \sum_{n=1,2}\left|u_n(k)\right\rangle\left[v_x^{+(-)}(k_y)\right]^n, \tag{A8}$$

where $\left[v_x^{+(-)}(k_y)\right]^n$ is the components of Wannier Hamiltonian's eigenvector, $\left|u_n(k)\right\rangle$ is the eigenvector of Eq. (A2). Therefore, it is a four-by-one vector here. Then the nest Wilson loop operator along k_y direction is

$$\tilde{W}_y^{+(-)}(k_x) = F_y^{+(-)}(k+N_y\Delta k_y)\cdots F_y^{+(-)}(k+\Delta k_y)F_y^{+(-)}(k), \tag{A9}$$

where $\left[F_y^{+(-)}(k)\right]^{mn} = \left\langle\omega_x^{+(-)}(k)\middle|\partial k_y\middle|\omega_x^{+(-)}(k)\right\rangle$, N_y is the number of discrete points and $\Delta k_y = 2\pi/a/N_y$. Finally, the nested polarization along *y* direction is

$$p_y^{v_x^{+(-)}} = -\frac{i}{2\pi}\frac{1}{N_x}\sum_{k_x} log[\tilde{W}_y^{+(-)}(k_x)] = 0.5. \tag{A10}$$

Similarly, $p_x^{v_y^{+(-)}} = 0.5$, when $|\varepsilon/\kappa| < 1$. These nonzero polarizations along the *x* and *y* edges reveal the topological property of the edges with quantized dipole moments which are brought by a quantized bulk quadrupole moment.

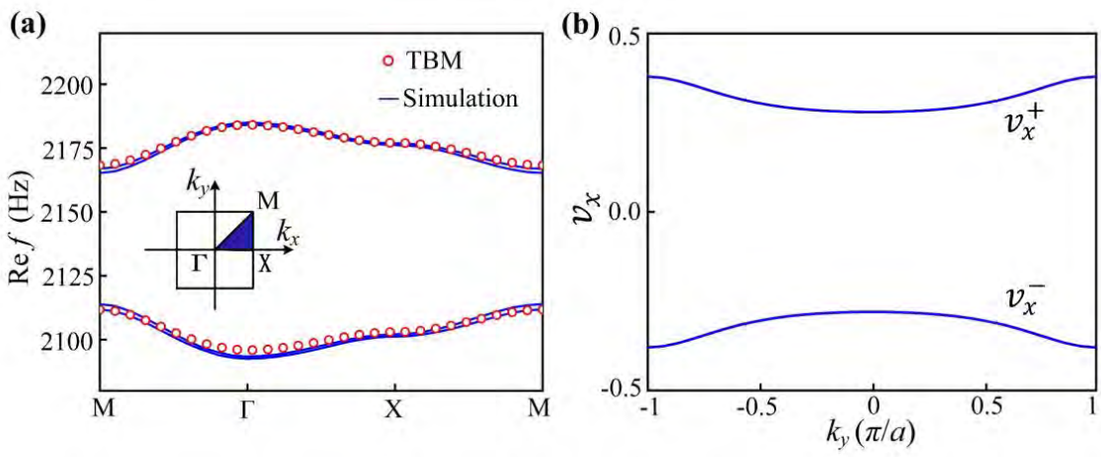

Figure A6 Energy Bands and Wannier bands. (a) Energy Band diagrams. The blue solid lines are numerical results, which are well-captured by the TBM results (red circles). The inset denotes the first BZ of the square lattice. (b) Wannier bands $v_x^{+(-)}(k_y)$ for Wannier Hamiltonian in Eq. (A7).

The quantized bulk quadrupole moment is not changed by adding uniform loss to the lattice sites, whose momentum space Hamiltonian can be written as

$$H_{loss}=H(k_x,k_y)-i\gamma_{1(2)}I_{4\times4} \tag{A11}$$

F. Eigenfrequencies for Different High-loss Subareas

To clearly see the eigenfrequency distributions in different acoustic lattices, numerical calculations based on the TBM are performed at $\Delta\gamma/\kappa_1=4.5$. For the acoustic lattice in Fig. 5.1(a) and Fig. 5.1(b) in the main text, the resultant eigenfrequencies are shown in Fig. A7(a) and Fig. A7(c), respectively. As we can see, the bulk states, denoted by the gray dots, are divided into four branches with a real frequency gap from 2103 Hz to 2177 Hz and an imaginary frequency gap from 14 Hz

to 125 Hz, arising from the uneven coupling strengths and the imbalanced losses, respectively. The eigenfrequencies of gapped edge states (blue dots) and twelve corner states (red dots) have different imaginary parts. The states with high imaginary parts mainly localized in the HLS [encircled by the black dashed lines in Figs. A7(b) and A7(d)], while those with lower imaginary parts mainly localized in the LLS. The sum of probability distributions of the bulk modes in Fig. A7(a) is presented in Fig. A7(b). Similarly, the eigenstates of the bulk states for the lattice with the "L" shaped HLS are plotted in Fig. A7(d), which further confirms that the increased turning corners in the interior bulk sites can cause the bulk and corner states to occupy the same sites.

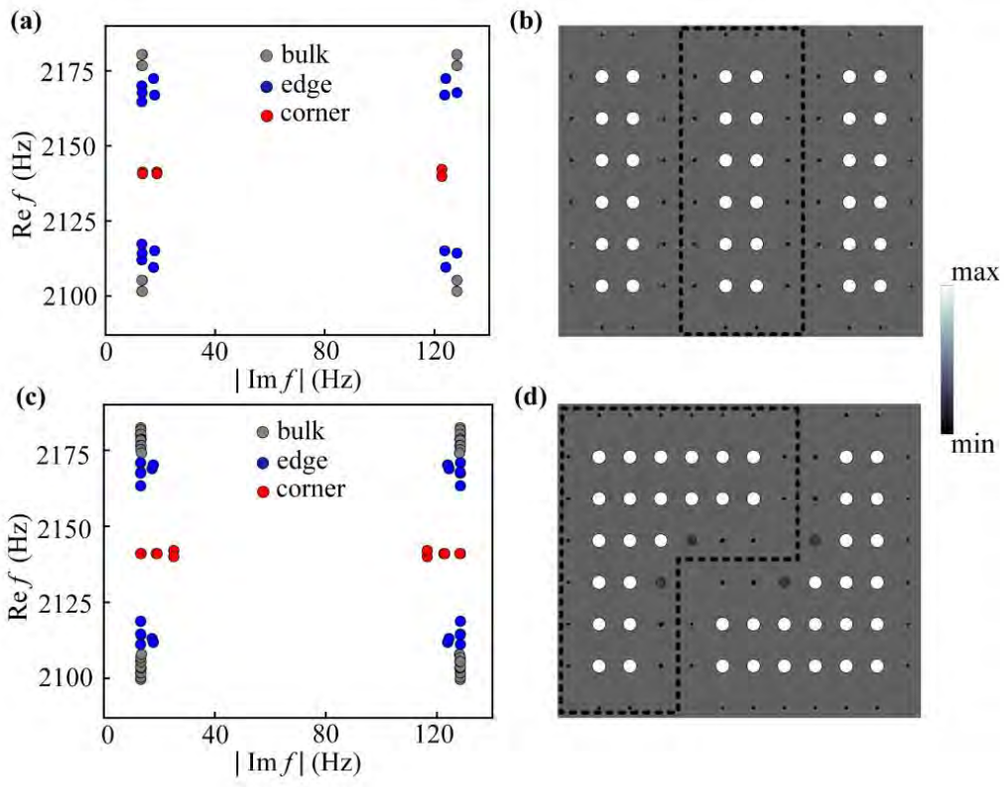

Figure A7 Eigenfrequencies distributions of the lattices with (a) rectangular HLS and (c) "L" shaped HLS when $\Delta\gamma / \kappa_1 = 4.5$. (b), (d) The sum of probability distributions of the bulk modes in (a) and (c), respectively.

G. Band Diagrams Slightly Away from High-symmetry Planes

To confirm the touching points between the first and second bands are nodal rings, we calculate band diagrams along directions that are slightly away from high-symmetry planes. For comparison, the band diagrams on high-symmetry planes k_z = 0 and $k_z = \pi/a_z$ are plotted in Figs. A8(a) and A8(b). The calculated band diagram with $k_z = 0.1\pi/a_z$ is shown in Fig. A8(c), which confirms that the red touching points in Fig. A8(a) are now gapped. We then consider the band diagram with $k_z = 0.9\pi/a_z$, and the result in Fig. A8(d) confirms that the blue and green touching points in Fig. A8(b) are also gapped when slightly away from the high-symmetry planes.

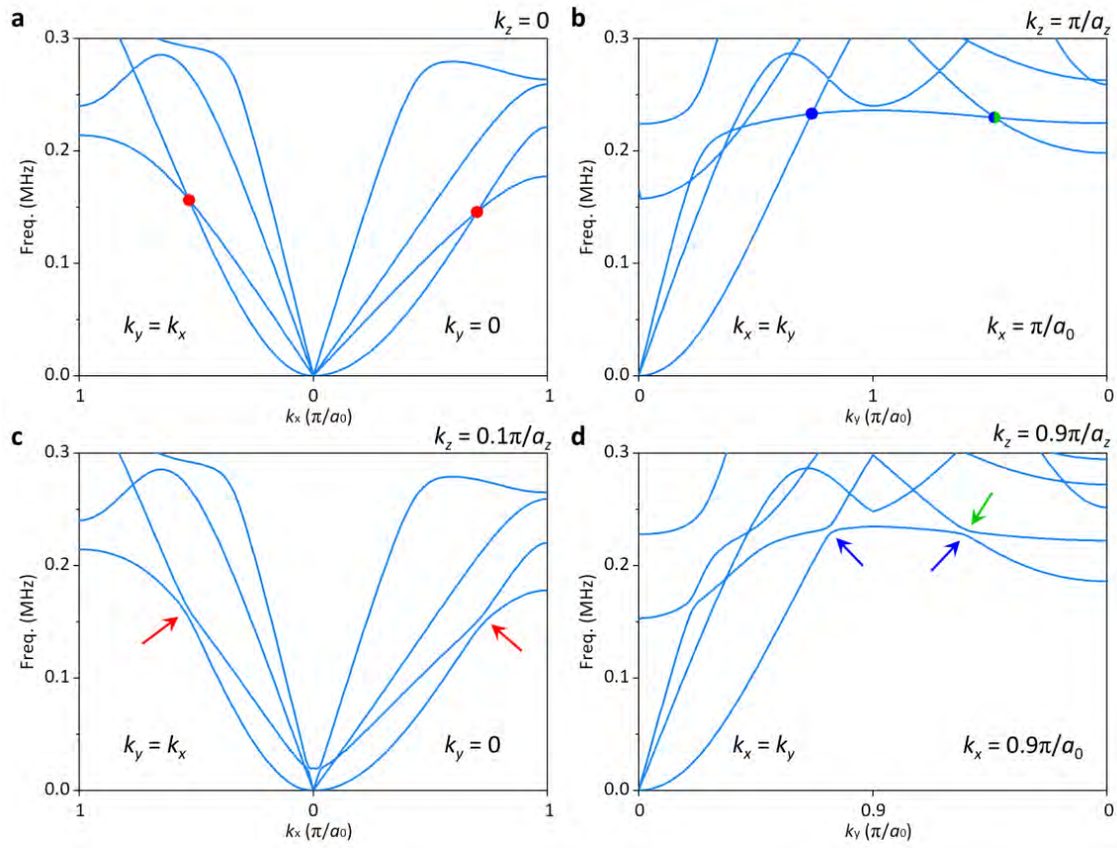

Figure A8 Calculated band diagrams on planes slightly away from high-symmetry ones. (a)-(d) Calculated band diagrams on $k_z = 0$ (a), $k_z = \pi/a_z$ (b), $k_z = 0.1\pi/a_z$ (c) and $k_z = 0.9\pi/a_z$ (d), respectively. The paths are indicated by equations in the figures, such as $k_y = k_x$ and $k_y = 0$. The touching points of the nodal rings demonstrated in (a) and (b), as denoted by the colored dots, are gapped correspondingly in (c) and (d), as indicated by the colored arrows.

H. Transfer Matrix Method

Here, we use a transfer matrix method to model the phononic crystal that is comprised of periodic solid plates (aluminum) without holes immersed in the background fluid (water). To obtain an analytical model, we first calculate the dispersions of the first two modes of the phononic crystal in the long-wavelength

limit, which allows us to model the solid plates based on the thin plate theory. We assume the time-harmonic condition and follow the $e^{-i\omega t}$ sign convention. As shown in Fig. A9, we assume $k_y = 0$ for simplicity as the system is rotation-invariant, and the acoustic pressure in the n-th water region can be written as

$$p_n(x,z) = A_n e^{ik_x x} e^{i\kappa_z z} + B_n e^{ik_x x} e^{-i\kappa_z z}, \tag{A12}$$

in which $\kappa_z = \sqrt{\omega^2 / c_w^2 - k_x^2}$ is the wave number of acoustic wave in z direction, while A_n and B_n are complex amplitudes of the forward and backward going acoustic waves, respectively. Likewise, the acoustic pressure in the (n+1)-th water region is then

$$p_{n+1}(x,z) = A_{n+1} e^{ik_x x} e^{ik_z (z-a_z)} + B_{n+1} e^{ik_x x} e^{-ik_z (z-a_z)}. \tag{A13}$$

The out-of-plane displacement in the n-th solid plate can be written as

$$w_n(x) = C_n e^{ik_x x}. \tag{A14}$$

The thin plate theory then gives the dynamic equation for the n-th solid plate

$$D\nabla_r^4 w(x) - p_n(x,z)\big|_{z=t_w} + p_{n+1}(x,z)\big|_{z=a_z} = \rho_m t_m \omega^2 w(x), \tag{A15}$$

where $D = \dfrac{E t_m^3}{12(1-\nu^2)}$ is the bending stiffness of the thin plate, and $\nabla_r = (\partial_x, \partial_y)$ is the gradient on the plate surface. From Eq. (A15), we can solve C_n as the function of A_n, B_n, A_{n+1}, and B_{n+1}

$$C_n = \frac{A_n e^{i\kappa_z t_w} + B_n e^{-i\kappa_z t_w} - A_{n+1} - B_{n+1}}{D k_x^4 - \omega^2 \rho_m t_m}. \tag{A16}$$

Then, we use the boundary conditions of continuous velocity on two surfaces of the n-th solid plate, which give

$$\left.\frac{\partial w_n(x)}{\partial t}\right|_{z=t_w} = v_{z,n}(x,z)\Big|_{z=t_w} \\ \left.\frac{\partial w_n(x)}{\partial t}\right|_{z=a_z} = v_{z,n+1}(x,z)\Big|_{z=a_z}, \tag{A17}$$

and it can be simplified under the time-harmonic condition as

$$-i\omega w_n(x)\Big|_{z=t_w} = \frac{1}{i\omega\rho_w}\left.\frac{\partial p_n(x,z)}{\partial z}\right|_{z=t_w} \\ -i\omega w_n(x)\Big|_{z=a_z} = \frac{1}{i\omega\rho_w}\left.\frac{\partial p_{n+1}(x,z)}{\partial z}\right|_{z=a_z}. \tag{A18}$$

Combining Eqs. A16 and A18, we can eliminate C_n and solve A_{n+1} and B_{n+1} as the function of A_n and B_n, and we obtain the transfer matrix M

$$\begin{bmatrix} A_{n+1} \\ B_{n+1} \end{bmatrix} = M \begin{bmatrix} A_n \\ B_n \end{bmatrix} = \begin{bmatrix} M_{11} & M_{12} \\ M_{21} & M_{22} \end{bmatrix} \begin{bmatrix} A_n \\ B_n \end{bmatrix}, \tag{A19}$$

with the matrix element

$$M_{11} = M_{22}^* = \frac{1}{2\omega^2\rho_w} e^{i\kappa_z t_w}\left[-ik_x^4\kappa_z D + \omega^2(2\rho_w + i\kappa_z\rho_m t_m)\right] \\ M_{12} = M_{21}^* = \frac{1}{2\omega^2\rho_w} ie^{-i\kappa_z t_w}\kappa_z(k_x^4 D - \omega^2\rho_m t_m), \tag{A20}$$

where * denotes the complex conjugate. Since the system is periodic and Hermitian, we can utilize the criteria on the trace of the transfer matrix which states that [174]

$$\mathrm{tr}(M) = 2\cos(k_z a_z), \tag{A21}$$

where k_z is the Bloch wave number in z direction. Then, it gives the equation which determines the dispersions of the modes

$$\frac{2\omega^2\rho_m\cos(\kappa_z t_w) + \kappa_z(Dk_x^4 - \omega^2\rho_m t_m)\sin(\kappa_z t_w)}{\omega^2\rho_w} = 2\cos(k_z a_z). \tag{A22}$$

When $k_z = 0$, one solution gives the WG mode,

$$\omega_{\mathrm{WG}} = k_x c_w, \tag{A23}$$

which coincides with the sound cone projected over k_z. The other solution in the long-wavelength limit when $k_z = 0$ gives the FL mode,

$$\omega_{\mathrm{FL}} = k_x^2 \sqrt{\frac{D}{\rho_m t_m + \rho_w t_w}}. \tag{A24}$$

As can be seen, this dispersion is similar to that of a thin plate in free space $\omega = k_x^2 \sqrt{D/(\rho_m t_m)}$, except its quadratic coefficient is reduced due to the fluid-solid interaction.

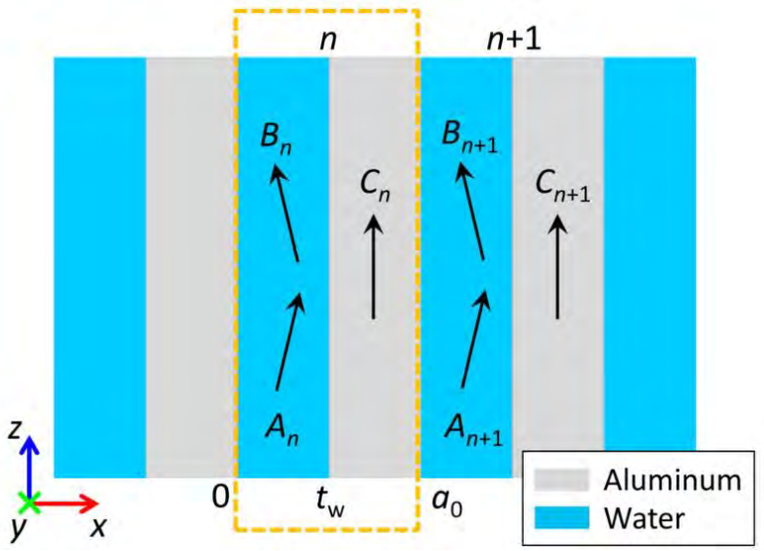

Figure A9 Schematic of the setup used to calculate dispersions with the transfer matrix method.

I. Control Experiment with Lattice Constant 4 mm

We change the in-plane lattice constant of the perforated holes to a_0 = 4 mm and perform additional experiments on the new control sample. Other geometric parameters are kept unchanged. The simulated band diagram along high-symmetry

directions is shown in Fig. A10(a). The photographs of the new control sample is shown in Fig. A10(b). The new Fourier spectra experimentally retrieved along high-symmetry directions for bulk bands is shown in Fig. A10(c).

For the new sample, good agreement is observed between the bright stripes in the experimental Fourier spectra and the calculated bulk bands projected along k_z direction. For comparison, the retrieved Fourier spectra when a_0 = 3 mm in the main text is also demonstrated here as Fig. A10(d). From the shift of the bright stripes which generally overlap with the projected bulk modes calculated from full-wave simulations, we can conclude that the observed signals are indeed owing to the bulk bands of the phononic crystals.

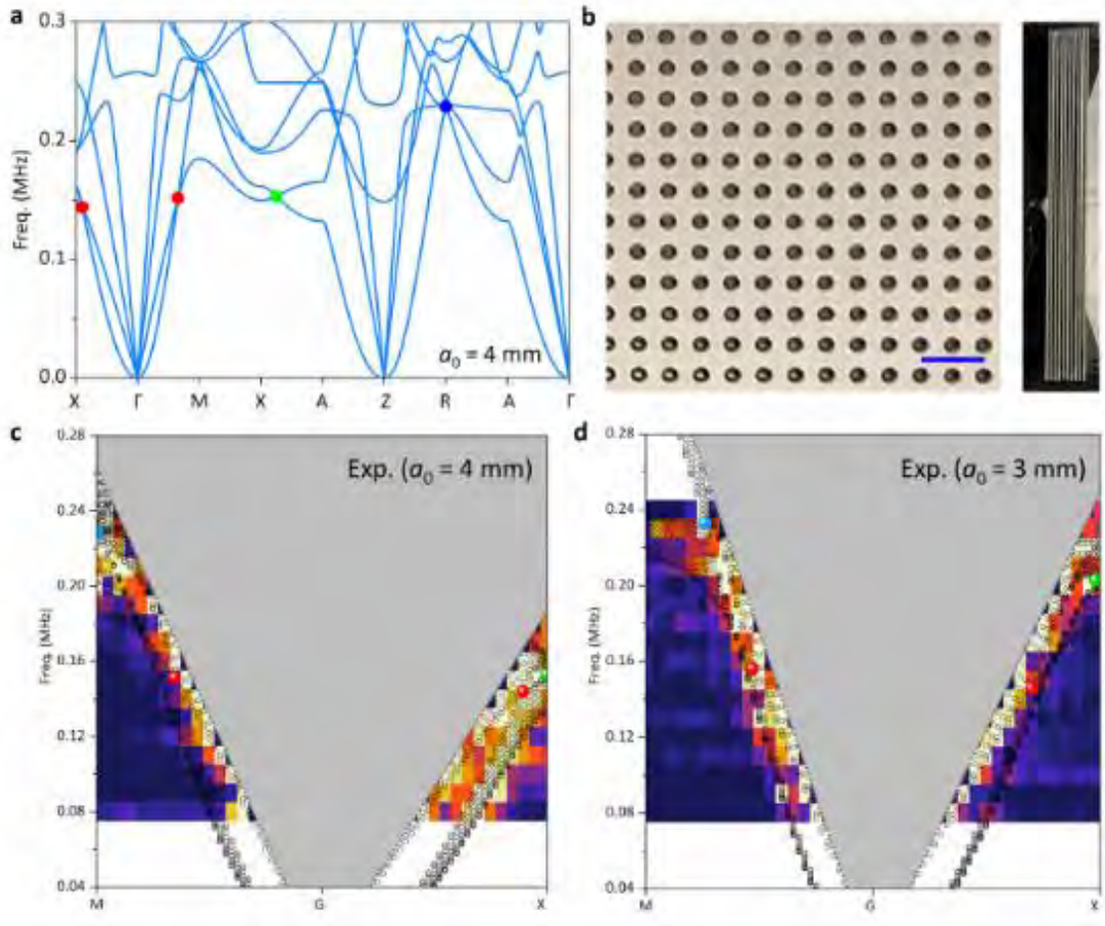

Figure A10 Experimentally retrieved Fourier spectra for bulk bands. (a) Calculated band diagram when the in-plane lattice constant a_0 = 4 mm. (b) Photographs of the control sample with a_0 = 4 mm. Left panel: close view of the perforated holes. Blue scale bar: 8 mm. Right panel: top view. (c) Experimentally retrieved Fourier spectra along high-symmetry directions when a_0 = 4 mm. (d) Experimentally retrieved Fourier spectra along high-symmetry directions when a_0 = 3 mm for comparison, essentially the same as Fig. 6.9(d) in the main text.

We can consider about the DSSs. The projected band diagram and the retrieved Fourier spectra for detection of surface states when a_0 = 4 mm are shown in Figs. A11(a) and Fig. A11(b), respectively. For comparison, the results for a_0 = 3 mm in the main text are also demonstrated here as Figs. A11(c) and A11(d), respectively. In

both cases, good agreement is observed between the bright stripes in the experimentally retrieved Fourier spectra and the numerically calculated dispersion of the drumhead surface states in both cases. The comparison between the experimentally retrieved Fourier spectra for different lattice constants also confirms that the detected signal includes contribution from the excited drumhead surface state.

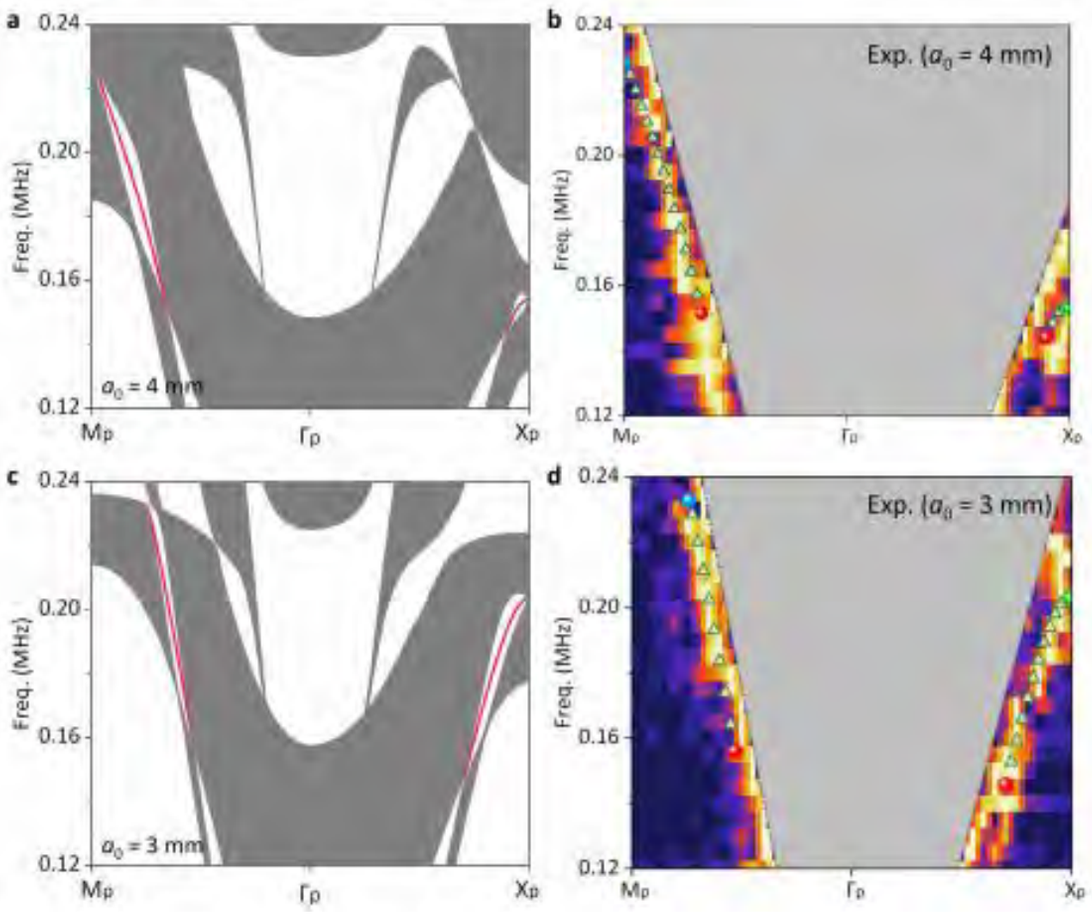

Figure A11 Experimentally retrieved Fourier spectra for surface states. (a) Projected band diagram for the supercell with a_0 = 4 mm. (b) Experimentally retrieved Fourier spectra with a_0 = 4 mm when probing surface states. (c) Projected band diagram for the supercell with a_0 = 3 mm for comparison. (d) Experimentally retrieved Fourier spectra with a_0 = 3 mm for comparison when probing surface states, essentially the same as Fig. 6.10(d) in the main text.

J. Experimentally Imaged Field Maps

The field maps that are experimentally imaged when we probe the surface states are plotted in Fig. A12.

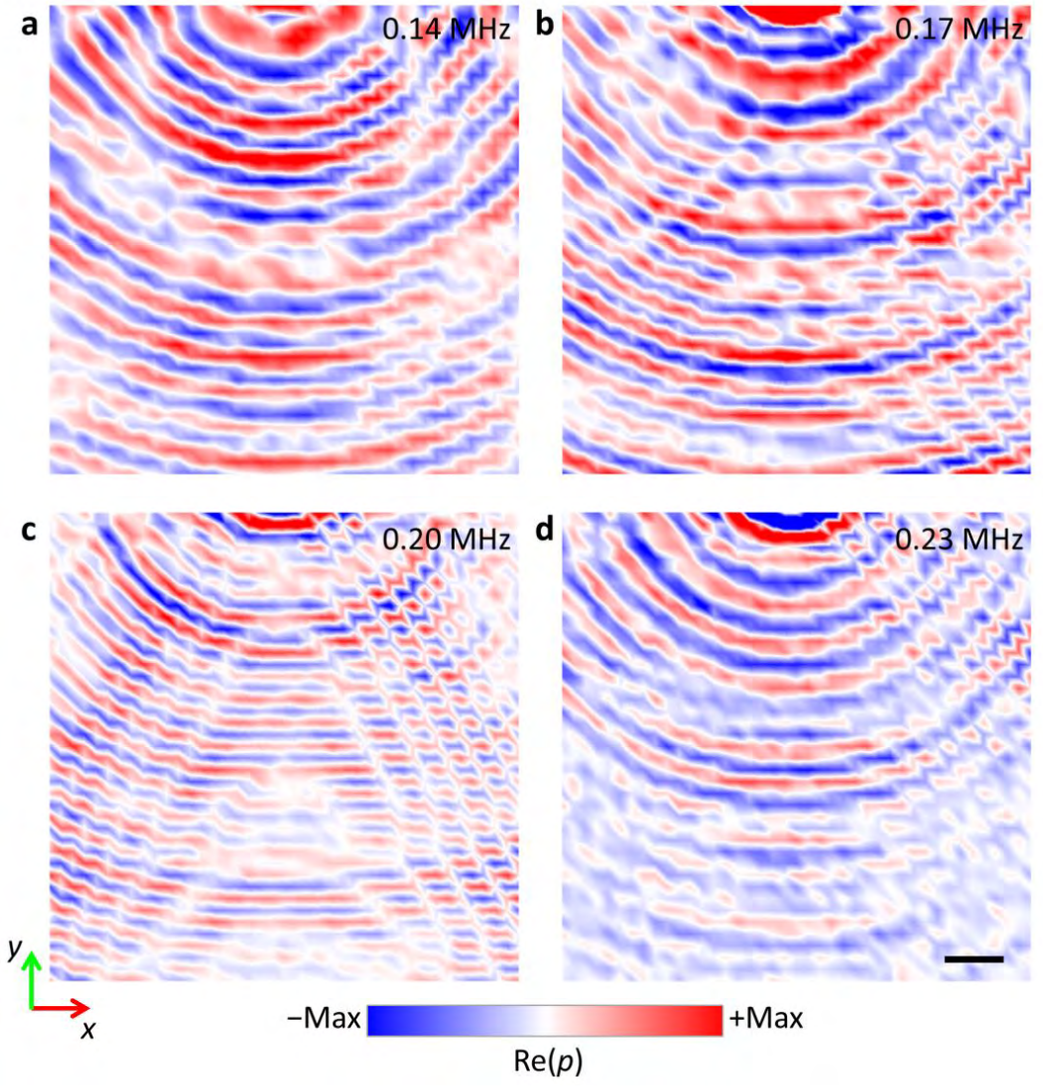

Figure A12 Experimentally imaged field maps. (a)-(d) The experimentally imaged field maps when probing surface states, exciting at the frequency (a) f = 0.14 MHz, (b) 0.17 MHz, (c) 0.20 MHz, and (d) 0.23 MHz, respectively. The scale bar is 15 mm.

Bibliography

[1] Klitzing Kv, Dorda G, Pepper M. New Method for High-Accuracy Determination of the Fine-Structure Constant Based on Quantized Hall Resistance. Physical Review Letters. 1980;45(6):494-7.

[2] Thouless DJ, Kohmoto M, Nightingale MP, den Nijs M. Quantized Hall Conductance in a Two-Dimensional Periodic Potential. Physical Review Letters. 1982;49(6):405-8.

[3] Halperin BI. Quantized Hall conductance, current-carrying edge states, and the existence of extended states in a two-dimensional disordered potential. Physical Review B. 1982;25(4):2185-90.

[4] Laughlin RB. Quantized Hall conductivity in two dimensions. Physical Review B. 1981;23(10):5632-3.

[5] Graf GM, Porta M. Bulk-Edge Correspondence for Two-Dimensional Topological Insulators. Communications in Mathematical Physics. 2013;324(3):851-95.

[6] Bernevig BA, Zhang SC. Quantum spin Hall effect. Phys Rev Lett. 2006;96(10):106802.

[7] Kane CL, Mele EJ. Quantum spin Hall effect in graphene. Phys Rev Lett. 2005;95(22):226801.

[8] Armitage NP, Mele EJ, Vishwanath A. Weyl and Dirac semimetals in three-dimensional solids. Reviews of Modern Physics. 2018;90(1).

[9] Fang C, Chen Y, Kee H-Y, Fu L. Topological nodal line semimetals with and without spin-orbital coupling. Physical Review B. 2015;92(8).

[10] Wang Z, Sun Y, Chen X-Q, Franchini C, Xu G, Weng H, et al. Dirac semimetal and topological phase transitions inA3Bi (A=Na, K, Rb). Physical Review B. 2012;85(19).

[11] Qi X-L, Zhang S-C. Topological insulators and superconductors. Reviews of Modern Physics. 2011;83(4):1057-110.

[12] Hasan MZ, Kane CL. Colloquium: Topological insulators. Reviews of Modern Physics. 2010;82(4):3045-67.

[13] Fleury R, Sounas D L, Sieck C F, Haberman M R, Alù A. Sound Isolation and Giant Linear Nonreciprocity in a Compact Acoustic Circulator. Science. 2014;343(6170): 516-519.

[14] Wang H-X, Guo G-Y, Jiang J-H. Band topology in classical waves: Wilson-loop approach to topological numbers and fragile topology. New Journal of Physics. 2019;21(9).

[15] El-Ganainy R, Makris KG, Khajavikhan M, Musslimani ZH, Rotter S, Christodoulides DN. Non-Hermitian physics and PT symmetry. Nature Physics. 2018;14(1):11-9.

[16] Feng L, El-Ganainy R, Ge L. Non-Hermitian photonics based on parity–time symmetry. Nature Photonics. 2017;11(12):752-62.

[17] Fan H, Gao H, An S, Gu Z, Liang S, Zheng Y, et al. Hermitian and non-hermitian topological edge states in one-dimensional perturbative elastic metamaterials. Mechanical Systems and Signal Processing. 2022;169.

[18] Fan H, Gao H, An S, Gu Z, Chen Y, Huang S, et al. Observation of non-Hermiticity-induced topological edge states in the continuum in a trimerized elastic lattice. Physical Review B. 2022;106(18).

[19] Gao H, Xue H, Gu Z, Liu T, Zhu J, Zhang B. Non-Hermitian route to higher-order topology in an acoustic crystal. Nat Commun. 2021;12(1):1888.

[20] Gao H, Xue H, Wang Q, Gu Z, Liu T, Zhu J, et al. Observation of topological edge states induced solely by non-Hermiticity in an acoustic crystal. Physical Review B. 2020;101(18).

[21] Xiao L, Deng T, Wang K, Zhu G, Wang Z, Yi W, et al. Non-Hermitian bulk–boundary correspondence in quantum dynamics. Nature Physics. 2020;16(7):761-6.

[22] Helbig T, Hofmann T, Imhof S, Abdelghany M, Kiessling T, Molenkamp LW, et al. Generalized bulk–boundary correspondence in non-Hermitian topolectrical circuits. Nature Physics. 2020;16(7):747-50.

[23] Kunst FK, Edvardsson E, Budich JC, Bergholtz EJ. Biorthogonal Bulk-Boundary Correspondence in Non-Hermitian Systems. Phys Rev Lett. 2018;121(2):026808.

[24] Cummer SA, Christensen J, Alù A. Controlling sound with acoustic metamaterials. Nature Reviews Materials. 2016;1(3).

[25] Watanabe H, Lu L. Space Group Theory of Photonic Bands. Phys Rev Lett. 2018;121(26):263903.

[26] Shen Y, Qiu C, Cai X, Ye L, Lu J, Ke M, et al. Valley-projected edge modes observed in underwater sonic crystals. Applied Physics Letters. 2019;114(2).

[27] Fan X, Qiu C, Shen Y, He H, Xiao M, Ke M, et al. Probing Weyl Physics with One-Dimensional Sonic Crystals. Phys Rev Lett. 2019;122(13):136802.

[28] Zhu R, Liu XN, Hu GK, Yuan FG, Huang GL. Microstructural designs of plate-type elastic metamaterial and their potential applications: a review. International Journal of Smart and Nano Materials. 2015;6(1):14-40.

[29] Heeger AJ, Kivelson S, Schrieffer JR, Su WP. Solitons in conducting polymers. Reviews of Modern Physics. 1988;60(3):781-850.

[30] Su WP, Schrieffer JR, Heeger AJ. Solitons in Polyacetylene. Physical Review Letters. 1979;42(25):1698-701.

[31] Li T, Du J, Zhang Q, Li Y, Fan X, Zhang F, et al. Acoustic Mobius Insulators from Projective Symmetry. Phys Rev Lett. 2022;128(11):116803.

[32] Xue H, Jia D, Ge Y, Guan YJ, Wang Q, Yuan SQ, et al. Observation of Dislocation-Induced Topological Modes in a Three-Dimensional Acoustic Topological Insulator. Phys Rev Lett. 2021;127(21):214301.

[33] Xue H, Ge Y, Sun HX, Wang Q, Jia D, Guan YJ, et al. Observation of an acoustic octupole topological insulator. Nat Commun. 2020;11(1):2442.

[34] Qi Y, Qiu C, Xiao M, He H, Ke M, Liu Z. Acoustic Realization of Quadrupole Topological Insulators. Phys Rev Lett. 2020;124(20):206601.

[35] Xue H, Yang Y, Gao F, Chong Y, Zhang B. Acoustic higher-order topological insulator on a kagome lattice. Nat Mater. 2019;18(2):108-12.

[36] Zak J. Berry's phase for energy bands in solids. Phys Rev Lett. 1989;62(23):2747-50.

[37] Xiao M, Ma G, Yang Z, Sheng P, Zhang ZQ, Chan CT. Geometric phase and band inversion in periodic acoustic systems. Nature Physics. 2015;11(3):240-4.

[38] Ma G, Xiao M, Chan CT. Topological phases in acoustic and mechanical systems. Nature Reviews Physics. 2019;1(4):281-94.

[39] Bahari B, Hsu L, Pan SH, Preece D, Ndao A, El Amili A, et al. Photonic quantum Hall effect and multiplexed light sources of large orbital angular momenta. Nature Physics. 2021;17(6):700-3.

[40] Raghu S, Haldane FDM. Analogs of quantum-Hall-effect edge states in photonic crystals.

Physical Review A. 2008;78(3).

[41] Roux P, Rosny J, Tanter M, Fink M. The Aharonov-Bohm Effect Revisited by an Acoustic Time-Reversal Mirror. Phys Rev Lett. 1997;79(17):3170.

[42] Yang Z, Gao F, Shi X, Lin X, Gao Z, Chong Y, et al. Topological acoustics. Phys Rev Lett. 2015;114(11):114301.

[43] Ni X, He C, Sun X-C, Liu X-p, Lu M-H, Feng L, et al. Topologically protected one-way edge mode in networks of acoustic resonators with circulating air flow. New Journal of Physics. 2015;17(5).

[44] Khanikaev AB, Fleury R, Mousavi SH, Alu A. Topologically robust sound propagation in an angular-momentum-biased graphene-like resonator lattice. Nat Commun. 2015;6:8260.

[45] Ding Y, Peng Y, Zhu Y, Fan X, Yang J, Liang B, et al. Experimental Demonstration of Acoustic Chern Insulators. Phys Rev Lett. 2019;122(1):014302.

[46] Xue H, Yang Y, Zhang B. Topological acoustics. Nature Reviews Materials. 2022;7(12):974-90.

[47] Bernevig B. A, Hughes T L., Zhang S. Quantum Spin Hall Effect and Topological Phase Transition in HgTe Quantum Wells. Science. 2006;314(5806): 1757-1761.

[48] Mei J, Chen Z, Wu Y. Pseudo-time-reversal symmetry and topological edge states in two-dimensional acoustic crystals. Sci Rep. 2016;6:32752.

[49] He C, Ni X, Ge H, Sun X-C, Chen Y-B, Lu M-H, et al. Acoustic topological insulator and robust one-way sound transport. Nature Physics. 2016;12(12):1124-9.

[50] Zhang Z, Wei Q, Cheng Y, Zhang T, Wu D, Liu X. Topological Creation of Acoustic Pseudospin Multipoles in a Flow-Free Symmetry-Broken Metamaterial Lattice. Phys Rev Lett. 2017;118(8):084303.

[51] Deng Y, Ge H, Tian Y, Lu M, Jing Y. Observation of zone folding induced acoustic topological insulators and the role of spin-mixing defects. Physical Review B. 2017;96(18).

[52] Yves S, Fleury R, Lemoult F, Fink M, Lerosey G. Topological acoustic polaritons: robust sound manipulation at the subwavelength scale. New Journal of Physics. 2017;19(7).

[53] Xia B-Z, Liu T-T, Huang G-L, Dai H-Q, Jiao J-R, Zang X-G, et al. Topological phononic insulator with robust pseudospin-dependent transport. Physical Review B. 2017;96(9).

[54] Zhang Z, Tian Y, Cheng Y, Wei Q, Liu X, Christensen J. Topological Acoustic Delay Line.

Physical Review Applied. 2018;9(3).

[55] Lu J, Qiu C, Ke M, Liu Z. Valley Vortex States in Sonic Crystals. Phys Rev Lett. 2016;116(9):093901.

[56] Lu J, Qiu C, Ye L, Fan X, Ke M, Zhang F, et al. Observation of topological valley transport of sound in sonic crystals. Nature Physics. 2016;13(4):369-74.

[57] Lu J, Qiu C, Xu S, Ye Y, Ke M, Liu Z. Dirac cones in two-dimensional artificial crystals for classical waves. Physical Review B. 2014;89(13).

[58] He C, Lai HS, He B, Yu SY, Xu X, Lu MH, et al. Acoustic analogues of three-dimensional topological insulators. Nat Commun. 2020;11(1):2318.

[59] Xie B, Liu H, Cheng H, Liu Z, Tian J, Chen S. Dirac points and the transition towards Weyl points in three-dimensional sonic crystals. Light Sci Appl. 2020;9(1):201.

[60] Cheng H, Sha Y, Liu R, Fang C, Lu L. Discovering Topological Surface States of Dirac Points. Phys Rev Lett. 2020;124(10):104301.

[61] Cai X, Ye L, Qiu C, Xiao M, Yu R, Ke M, et al. Symmetry-enforced three-dimensional Dirac phononic crystals. Light Sci Appl. 2020;9:38.

[62] Wan X, Turner AM, Vishwanath A, Savrasov SY. Topological semimetal and Fermi-arc surface states in the electronic structure of pyrochlore iridates. Physical Review B. 2011;83(20).

[63] Zhang X, Yu Z-M, Lu Y, Sheng X-L, Yang HY, Yang SA. Hybrid nodal loop metal: Unconventional magnetoresponse and material realization. Physical Review B. 2018;97(12).

[64] Chen YF, Chen ZG, Ge H, He C, Li X, Lu MH, et al. Various topological phases and their abnormal effects of topological acoustic metamaterials. Interdisciplinary Materials. 2023;2(2):179-230.

[65] Yan Q, Liu R, Yan Z, Liu B, Chen H, Wang Z, et al. Experimental discovery of nodal chains. Nature Physics. 2018;14(5):461-4.

[66] Ge H, Ni X, Tian Y, Gupta SK, Lu M-H, Lin X, et al. Experimental Observation of Acoustic Weyl Points and Topological Surface States. Physical Review Applied. 2018;10(1).

[67] Xiao M, Chen W-J, He W-Y, Chan CT. Synthetic gauge flux and Weyl points in acoustic systems. Nature Physics. 2015;11(11):920-4.

[68] Li F, Huang X, Lu J, Ma J, Liu Z. Weyl points and Fermi arcs in a chiral phononic crystal. Nature

Physics. 2017;14(1):30-4.

[69] Xiao D, Chang M-C, Niu Q. Berry phase effects on electronic properties. Reviews of Modern Physics. 2010;82(3):1959-2007.

[70] He H, Qiu C, Ye L, Cai X, Fan X, Ke M, et al. Topological negative refraction of surface acoustic waves in a Weyl phononic crystal. Nature. 2018;560(7716):61-4.

[71] Qiu H, Qiu C, Yu R, Xiao M, He H, Ye L, Ke M, Liu Z. Straight nodal lines and waterslide surface states observed in acoustic metacrystals. Physical Review B. 2019; 100(041303(R)).

[72] Deng W, Lu J, Li F, Huang X, Yan M, Ma J, et al. Nodal rings and drumhead surface states in phononic crystals. Nat Commun. 2019;10(1):1769.

[73] Lu J, Huang X, Yan M, Li F, Deng W, Liu Z. Nodal-Chain Semimetal States and Topological Focusing in Phononic Crystals. Physical Review Applied. 2020;13(5).

[74] Benalcazar WA, Bernevig BA, Hughes TL. Electric multipole moments, topological multipole moment pumping, and chiral hinge states in crystalline insulators. Physical Review B. 2017;96(24).

[75] Benalcazar W A, Bernevig B A, Hughes T L. Quantized electric multipole insulators. Science. 2017; 357(6346):61-66.

[76] Kang B, Shiozaki K, Cho GY. Many-body order parameters for multipoles in solids. Physical Review B. 2019;100(24).

[77] Wheeler WA, Wagner LK, Hughes TL. Many-body electric multipole operators in extended systems. Physical Review B. 2019;100(24).

[78] Schindler F, Cook A M, Vergniory M G, Wang Z, Parkin S S P, Bernevig B A, Neupert T. Higher-order topological insulators. Science Advances. 2018;4(6).

[79] Schindler F, Wang Z, Vergniory MG, Cook AM, Murani A, Sengupta S, et al. Higher-Order Topology in Bismuth. Nat Phys. 2018;14(9):918-24.

[80] Zhang X, Lin ZK, Wang HX, Xiong Z, Tian Y, Lu MH, et al. Symmetry-protected hierarchy of anomalous multipole topological band gaps in nonsymmorphic metacrystals. Nat Commun. 2020;11(1):65.

[81] Chen K, Weiner M, Li M, Ni X, Alu A, Khanikaev AB. Nonlocal topological insulators: Deterministic aperiodic arrays supporting localized topological states protected by nonlocal

symmetries. Proc Natl Acad Sci U S A. 2021;118(34).

[82] Ni X, Weiner M, Alu A, Khanikaev AB. Observation of higher-order topological acoustic states protected by generalized chiral symmetry. Nat Mater. 2019;18(2):113-20.

[83] Zhang X, Liu L, Lu MH, Chen YF. Valley-Selective Topological Corner States in Sonic Crystals. Phys Rev Lett. 2021;126(15):156401.

[84] Zhang X, Xie BY, Wang HF, Xu X, Tian Y, Jiang JH, et al. Dimensional hierarchy of higher-order topology in three-dimensional sonic crystals. Nat Commun. 2019;10(1):5331.

[85] Weiner M, Ni X, Li M, Alù A, Khanikaev A B. Demonstration of a third-order hierarchy of topological states in a three-dimensional acoustic metamaterial. Science Advances. 2020;6(13).

[86] Xue H, Yang Y, Liu G, Gao F, Chong Y, Zhang B. Realization of an Acoustic Third-Order Topological Insulator. Phys Rev Lett. 2019;122(24):244301.

[87] Zhang X, Wang H-X, Lin Z-K, Tian Y, Xie B, Lu M-H, et al. Second-order topology and multidimensional topological transitions in sonic crystals. Nature Physics. 2019;15(6):582-8.

[88] Zhou W, Wu B, Chen Z, Chen W, Lim CW, Reddy JN. Actively controllable topological phase transition in homogeneous piezoelectric rod system. Journal of the Mechanics and Physics of Solids. 2020;137.

[89] Huang H, Chen J, Huo S. Simultaneous topological Bragg and locally resonant edge modes of shear horizontal guided wave in one-dimensional structure. Journal of Physics D: Applied Physics. 2017;50(27).

[90] Chaunsali R, Kim E, Thakkar A, Kevrekidis PG, Yang J. Demonstrating an In Situ Topological Band Transition in Cylindrical Granular Chains. Phys Rev Lett. 2017;119(2):024301.

[91] Wang W, Jin Y, Wang W, Bonello B, Djafari-Rouhani B, Fleury R. Robust Fano resonance in a topological mechanical beam. Physical Review B. 2020;101(2).

[92] Vila J, Paulino GH, Ruzzene M. Role of nonlinearities in topological protection: Testing magnetically coupled fidget spinners. Physical Review B. 2019;99(12).

[93] Wang P, Lu L, Bertoldi K. Topological Phononic Crystals with One-Way Elastic Edge Waves. Phys Rev Lett. 2015;115(10):104302.

[94] Nash LM, Kleckner D, Read A, Vitelli V, Turner AM, Irvine WT. Topological mechanics of

gyroscopic metamaterials. Proc Natl Acad Sci U S A. 2015;112(47):14495-500.

[95] Süsstrunk R, Huber S D. Observation ofphononic helical edge states in a mechanical topological insulator. Science. 2015;349(6243):47-50.

[96] Mousavi SH, Khanikaev AB, Wang Z. Topologically protected elastic waves in phononic metamaterials. Nat Commun. 2015;6:8682.

[97] Miniaci M, Pal RK, Morvan B, Ruzzene M. Experimental Observation of Topologically Protected Helical Edge Modes in Patterned Elastic Plates. Physical Review X. 2018;8(3).

[98] Yu SY, He C, Wang Z, Liu FK, Sun XC, Li Z, et al. Elastic pseudospin transport for integratable topological phononic circuits. Nat Commun. 2018;9(1):3072.

[99] Vila J, Pal RK, Ruzzene M. Observation of topological valley modes in an elastic hexagonal lattice. Physical Review B. 2017;96(13).

[100] Yan M, Lu J, Li F, Deng W, Huang X, Ma J, et al. On-chip valley topological materials for elastic wave manipulation. Nat Mater. 2018;17(11):993-8.

[101] Liu T-W, Semperlotti F. Tunable Acoustic Valley–Hall Edge States in Reconfigurable Phononic Elastic Waveguides. Physical Review Applied. 2018;9(1).

[102] Pal RK, Ruzzene M. Edge waves in plates with resonators: an elastic analogue of the quantum valley Hall effect. New Journal of Physics. 2017;19(2).

[103] Chen J-J, Huo S-Y, Geng Z-G, Huang H-B, Zhu X-F. Topological valley transport of plate-mode waves in a homogenous thin plate with periodic stubbed surface. AIP Advances. 2017;7(11).

[104] Huo S-y, Chen J-j, Huang H-b, Wei Y-j, Tan Z-h, Feng L-y, et al. Experimental demonstration of valley-protected backscattering suppression and interlayer topological transport for elastic wave in three-dimensional phononic crystals. Mechanical Systems and Signal Processing. 2021;154.

[105] Liu Y, Xu Y, Duan W. Three-Dimensional Topological States of Phonons with Tunable Pseudospin Physics. Research (Wash D C). 2019;2019:5173580.

[106] Shi X, Chaunsali R, Li F, Yang J. Elastic Weyl Points and Surface Arc States in Three-Dimensional Structures. Physical Review Applied. 2019;12(2).

[107] Ganti SS, Liu T-W, Semperlotti F. Weyl points and topological surface states in a three-dimensional sandwich-type elastic lattice. New Journal of Physics. 2020;22(8).

[108] Wang Y-T, Tsai Y-W. Multiple Weyl and double-Weyl points in an elastic chiral lattice. New Journal of Physics. 2018;20(8).

[109] Wu Y, Yan M, Lin ZK, Wang HX, Li F, Jiang JH. On-chip higher-order topological micromechanical metamaterials. Sci Bull (Beijing). 2021;66(19):1959-66.

[110] Huo S-y, Huang H-b, Feng L-y, Chen J-j. Edge states and corner modes in second-order topological phononic crystal plates. Applied Physics Express. 2019;12(9).

[111] Wu Q, Chen H, Li X, Huang G. In-Plane Second-Order Topologically Protected States in Elastic Kagome Lattices. Physical Review Applied. 2020;14(1).

[112] Serra-Garcia M, Peri V, Susstrunk R, Bilal OR, Larsen T, Villanueva LG, et al. Observation of a phononic quadrupole topological insulator. Nature. 2018;555(7696):342-5.

[113] Fan H, Xia B, Tong L, Zheng S, Yu D. Elastic Higher-Order Topological Insulator with Topologically Protected Corner States. Phys Rev Lett. 2019;122(20):204301.

[114] Dorey P, Dunning C, Tateo R. Spectral equivalences, Bethe ansatz equations, and reality properties in PT-symmetric quantum mechanics. J. Phys. A: Math. Gen. 2001; 34: 5679–5704.

[115] Berry M V. Physics of nonhermitian degeneracies. Czechoslovak Journal of Physics, 2004;54(10): 1039–1047.

[116] Peng B, Özdemir S. K., Rotter S., Yilmaz H., Liertzer M., Monifi F., Bender C. M., Nori F., Yang L. Loss-induced suppression and revival of lasing. Science. 2014;346(6207): 328-332.

[117] Lin Z, Ramezani H, Eichelkraut T, Kottos T, Cao H, Christodoulides DN. Unidirectional invisibility induced by PT-symmetric periodic structures. Phys Rev Lett. 2011;106(21):213901.

[118] Liu T, Zhu X, Chen F, Liang S, Zhu J. Unidirectional Wave Vector Manipulation in Two-Dimensional Space with an All Passive Acoustic Parity-Time-Symmetric Metamaterials Crystal. Phys Rev Lett. 2018;120(12):124502.

[119] Chiu C-K, Teo JCY, Schnyder AP, Ryu S. Classification of topological quantum matter with symmetries. Reviews of Modern Physics. 2016;88(3).

[120] Kawabata K, Shiozaki K, Ueda M, Sato M. Symmetry and Topology in Non-Hermitian Physics. Physical Review X. 2019;9(4).

[121] Takata K, Notomi M. Photonic Topological Insulating Phase Induced Solely by Gain and Loss.

Phys Rev Lett. 2018;121(21):213902.

[122] Schomerus H. Topologically protected midgap states in complex photonic lattices. Opt Lett. 2013;38(11):1912-4.

[123] Yuce C, Ramezani H. Topological states in a non-Hermitian two-dimensional Su-Schrieffer-Heeger model. Physical Review A. 2019;100(3).

[124] Luo XW, Zhang C. Higher-Order Topological Corner States Induced by Gain and Loss. Phys Rev Lett. 2019;123(7):073601.

[125] Gu Z, Gao H, Cao P-C, Liu T, Zhu X-F, Zhu J. Controlling Sound in Non-Hermitian Acoustic Systems. Physical Review Applied. 2021;16(5).

[126] Zhao H, Qiao X, Wu T, Midya B, Longhi S, Feng L. Non-Hermitian topological light steering. Science. 2019;365(6458):1163–1166.

[127] Lee CH, Thomale R. Anatomy of skin modes and topology in non-Hermitian systems. Physical Review B. 2019;99(20).

[128] Yao S, Wang Z. Edge States and Topological Invariants of Non-Hermitian Systems. Phys Rev Lett. 2018;121(8):086803.

[129] Ghatak A, Brandenbourger M, van Wezel J, Coulais C. Observation of non-Hermitian topology and its bulk-edge correspondence in an active mechanical metamaterial. Proc Natl Acad Sci U S A. 2020;117(47):29561-8.

[130] Song W, Sun W, Chen C, Song Q, Xiao S, Zhu S, et al. Breakup and Recovery of Topological Zero Modes in Finite Non-Hermitian Optical Lattices. Phys Rev Lett. 2019;123(16):165701.

[131] Zhu X, Wang H, Gupta SK, Zhang H, Xie B, Lu M, et al. Photonic non-Hermitian skin effect and non-Bloch bulk-boundary correspondence. Physical Review Research. 2020;2(1).

[132] Scheibner C, Irvine WTM, Vitelli V. Non-Hermitian Band Topology and Skin Modes in Active Elastic Media. Phys Rev Lett. 2020;125(11):118001.

[133] Harari G, Bandres MA, Lumer Y, Rechtsman MC, Chong YD, Khajavikhan M, et al. Topological insulator laser: Theory. Science. 2018;359(6381).

[134] Liu S, Ma S, Yang C, Zhang L, Gao W, Xiang YJ, et al. Gain- and Loss-Induced Topological Insulating Phase in a Non-Hermitian Electrical Circuit. Physical Review Applied. 2020;13(1).

[135] Poli C, Bellec M, Kuhl U, Mortessagne F, Schomerus H. Selective enhancement of topologically induced interface states in a dielectric resonator chain. Nat Commun. 2015;6:6710.

[136] Matlack KH, Serra-Garcia M, Palermo A, Huber SD, Daraio C. Designing perturbative metamaterials from discrete models. Nat Mater. 2018;17(4):323-8.

[137] Delplace P, Ullmo D, Montambaux G. Zak phase and the existence of edge states in graphene. Physical Review B. 2011;84(19).

[138] Zangeneh-Nejad F, Fleury R. Topological analog signal processing. Nat Commun. 2019;10(1):2058.

[139] Weimann S, Kremer M, Plotnik Y, Lumer Y, Nolte S, Makris KG, et al. Topologically protected bound states in photonic parity-time-symmetric crystals. Nat Mater. 2017;16(4):433-8.

[140] Vaidya S, Benalcazar WA, Cerjan A, Rechtsman MC. Point-Defect-Localized Bound States in the Continuum in Photonic Crystals and Structured Fibers. Phys Rev Lett. 2021;127(2):023605.

[141] Hsu CW, Zhen B, Stone AD, Joannopoulos JD, Soljačić M. Bound states in the continuum. Nature Reviews Materials. 2016;1(9).

[142] Zhen B, Hsu CW, Lu L, Stone AD, Soljacic M. Topological nature of optical bound states in the continuum. Phys Rev Lett. 2014;113(25):257401.

[143] Hsu CW, Zhen B, Lee J, Chua SL, Johnson SG, Joannopoulos JD, et al. Observation of trapped light within the radiation continuum. Nature. 2013;499(7457):188-91.

[144] Yang BJ, Saeed Bahramy M, Nagaosa N. Topological protection of bound states against the hybridization. Nat Commun. 2013;4:1524.

[145] Xiao YX, Ma G, Zhang ZQ, Chan CT. Topological Subspace-Induced Bound State in the Continuum. Phys Rev Lett. 2017;118(16):166803.

[146] Benalcazar WA, Cerjan A. Bound states in the continuum of higher-order topological insulators. Physical Review B. 2020;101(16).

[147] Chen Z-G, Xu C, Al Jahdali R, Mei J, Wu Y. Corner states in a second-order acoustic topological insulator as bound states in the continuum. Physical Review B. 2019;100(7).

[148] Chen Z-G, Wang L, Zhang G, Ma G. Chiral Symmetry Breaking of Tight-Binding Models in Coupled Acoustic-Cavity Systems. Physical Review Applied. 2020;14(2).

[149] Jin L. Topological phases and edge states in a non-Hermitian trimerized optical lattice. Physical Review A. 2017;96(3).

[150] Ding K, Zhang ZQ, Chan CT. Coalescence of exceptional points and phase diagrams for one-dimensionalPT-symmetric photonic crystals. Physical Review B. 2015;92(23).

[151] Physik FB. Unfolding a diabolic point: a generalized crossing scenario. J. Phys. A: Math. Gen. 2003;36:2125–2137.

[152] Cao L, Yang Z, Xu Y, Fan S-W, Zhu Y, Chen Z, et al. Flexural wave absorption by lossy gradient elastic metasurface. Journal of the Mechanics and Physics of Solids. 2020;143.

[153] Li Y, Fan C, Hu X, Ao Y, Lu C, Chan CT, et al. Effective Hamiltonian for Photonic Topological Insulator with Non-Hermitian Domain Walls. Phys Rev Lett. 2022;129(5):053903.

[154] Deng Y, Benalcazar WA, Chen Z-G, Oudich M, Ma G, Jing Y. Observation of Degenerate Zero-Energy Topological States at Disclinations in an Acoustic Lattice. Physical Review Letters. 2022;128(17).

[155] Noh J, Benalcazar WA, Huang S, Collins MJ, Chen KP, Hughes TL, et al. Topological protection of photonic mid-gap defect modes. Nature Photonics. 2018;12(7):408-15.

[156] Li M, Zhirihin D, Gorlach M, Ni X, Filonov D, Slobozhanyuk A, et al. Higher-order topological states in photonic kagome crystals with long-range interactions. Nature Photonics. 2019;14(2):89-94.

[157] Yang E, Yang B, You O, Chan HC, Mao P, Guo Q, et al. Observation of Non-Abelian Nodal Links in Photonics. Phys Rev Lett. 2020;125(3):033901.

[158] Estrada H, Candelas P, Belmar F, Uris A, de Abajo FJG, Meseguer F. Engineering surface waves in flat phononic plates. Physical Review B. 2012;85(17):174301.

[159] Wu X, Li X, Zhang R-Y, Xiang X, Tian J, Huang Y, et al. Deterministic Scheme for Two-Dimensional Type-II Dirac Points and Experimental Realization in Acoustics. Physical Review Letters. 2020;124(7):075501.

[160] Xiong Z, Wang H-X, Ge H, Shi J, Luo J, Lai Y, et al. Topological node lines in mechanical metacrystals. Physical Review B. 2018;97(18):180101.

[161] Wang H-X, Guo G-Y, Jiang J-H. Band topology in classical waves: Wilson-loop approach to topological numbers and fragile topology. New Journal of Physics. 2019;21(9):093029.

[162] Hirayama M, Okugawa R, Miyake T, Murakami S. Topological Dirac nodal lines and surface charges in fcc alkaline earth metals. Nature Communications. 2017;8(1):1-9.

[163] Deng W, Lu J, Li F, Huang X, Yan M, Ma J, et al. Nodal rings and drumhead surface states in phononic crystals. Nature Communications. 2019;10(1):1769.

[164] Guo Q, Jiang T, Zhang RY, Zhang L, Zhang ZQ, Yang B, et al. Experimental observation of non-Abelian topological charges and edge states. Nature. 2021;594(7862):195-200.

[165] Liu JJ, Li ZW, Chen ZG, Tang W, Chen A, Liang B, et al. Experimental Realization of Weyl Exceptional Rings in a Synthetic Three-Dimensional Non-Hermitian Phononic Crystal. Phys Rev Lett. 2022;129(8):084301.

[166] Shi C, Dubois M, Chen Y, Cheng L, Ramezani H, Wang Y, et al. Accessing the exceptional points of parity-time symmetric acoustics. Nat Commun. 2016;7:11110.

[167] Hu B, Zhang Z, Zhang H, Zheng L, Xiong W, Yue Z, et al. Non-Hermitian topological whispering gallery. Nature. 2021;597(7878):655-9.

[168] Huang X, Deng W, Li F, Lu J, Liu Z. Ideal Type-II Weyl Phase and Topological Transition in Phononic Crystals. Phys Rev Lett. 2020;124(20):206802.

[169] Xia BW, Wang R, Chen ZJ, Zhao YJ, Xu H. Symmetry-Protected Ideal Type-II Weyl Phonons in CdTe. Phys Rev Lett. 2019;123(6):065501.

[170] Wen Z, Jin Y, Gao P, Zhuang X, Rabczuk T, Djafari-Rouhani B. Topological cavities in phononic plates for robust energy harvesting. Mechanical Systems and Signal Processing. 2022;162.

[171] Kumar A, Gupta M, Pitchappa P, Tan YJ, Wang N, Singh R. Topological sensor on a silicon chip. Applied Physics Letters. 2022;121(1).

[172] Budich JC, Bergholtz EJ. Non-Hermitian Topological Sensors. Phys Rev Lett. 2020;125(18):180403.

[173] Liu Z, Shan S, Cheng L. Nonlinear-Lamb-wave-based plastic damage detection assisted by topologically designed metamaterial filters. Structural Health Monitoring. 2022;22(3):1828-43.

[174] Shadrivov IV, Sukhorukov AA, Kivshar YS. Complete band gaps in one-dimensional left-handed periodic structures. Physical Review Letters. 2005;95(19):193903.